EVALUATION OF METAL NITRIDES AND BORIDES AS ALTERNATIVE ELECTROCATALYST SUPPORT MATERIALS FOR POLYMER ELECTROLYTE FUEL CELLS

Dissertation

Submitted in partial fulfilment of the requirement for the degree of

Master of Science in Chemical Engineering

Prepared by:

Thulile P. Khoza

Prepared for:

Dr Sharon Blair

Dr Pieter B.J Levecque

2014

Department of Chemical Engineering

Centre for Catalysis Research

National Hydrogen Catalysis Competence Centre

University of Cape Town

Plagiarism Declaration

I know the meaning of plagiarism and declare that all the work in this document, save for that which is properly acknowledged, is my own.

Signed by candidate

Signature Removed

Thulile P. Khoza

Acknowledgements

First and foremost, I would like to thank Dr Olaf Conrad for accepting me into the National Hydrogen Catalysis Competence Centre as an MSc candidate. Over the past 18 months I have met incredible people, learnt a lot and grown as a person. I am really grateful for the opportunity.

A special thanks to my project supervisors: Sharon Blair and Pieter Levecque. Sharon, thank you so much for the support, encouragement and insightful comments.

Pieter, there aren't enough words to describe how grateful I am for having you as a supervisor. You guided me through the experimental work and helped me with writing up of this thesis. You gave me so much support from day one, your patience, motivation and enthusiasm just blows me away. I did not think this project would have been done anytime soon, but you had faith and you helped me to get it done on time. Thank you so much!

To my Project mentor Shiro Tanaka, it has been a great pleasure to work with you. You were there for me every step of the way; you encouraged and challenged me to think outside of the box. You have inspired me in so many ways. Thank you so much for the guidance and knowledge you have imparted to me. I have learnt a lot from you.

And I would like to thank the following people as well,

Rhiyaad Mohamed, for tough questions which made me aware of other things regarding my work and showing me how to do RRDE experiments.

Mohammed Jaffer and Miranda Waldron for microscopic analysis.

Collen Jackson, for showing me how to synthesize catalysts using OMCVD.

My friends Zanele, Bontle, Koketso, Malebelo, Avela and Molefi for showing so much support during the course of this research.

Last but not least, I would like to thank my parents for their unconditional love and support.

Synopsis

Polymer electrolyte fuel cells (PEFCs) have wide variety of commercial applications, however due to poor durability and high cost, this technology has currently not reached its commercialization stage. Poor durability is mainly attributed to carbon support corrosion during start-up and shut-down of the fuel cell. Corrosion of the electrocatalyst support materials has numerous adverse effects on the performance of the fuel cell, such as weakening of metal-support interaction which results in Pt detachment, dissolution and sintering. Hence, the electrochemical active surface area is significantly reduced. It is clear that there is an urgent need for more robust, high performance alternative support materials to carbon. In this study, metal nitrides and borides (TiN, ZrN, TiB_2, ZrB_2 and LaB_6) were evaluated as potential support materials, in an attempt to improve the durability and performance of PEFCs.

Metal nitrides and borides were first subjected to a stability test by exposing them to potential cycling from 0.0 V vs SHE to 1.5 V vs SHE in 0.1 M $HClO_4$, 3000 times at room temperature. It was found that metal nitrides were more electrochemically stable than metal borides. Metal nitrides were passivated by formation of surface oxides (oxynitrides and metal oxides), whilst metal borides formed a B_2O_3 layer which is less protective than metal oxides and oxynitrides. Thus metal borides were continuously oxidised over the 3000 cycles; however, the rate of oxidation was much lower compared to Vulcan XC-72 carbon.

Using a wet chemical (impregnation) method well dispersed Pt nanoparticles, with a narrow size distribution could be deposited on all support materials except for Zr-based materials. The prepared catalysts were electrochemically characterised and it was found that Pt supported on metal nitrides and borides showed less Pt utilisation and activity towards ORR, compared to Pt/C. This was attributed to the presence of surface oxides, which significantly reduced electron conductivity. Pt/LaB_6 showed reasonable activity, although it was still lower than of its counterpart Pt/C. The durability of Pt/LaB_6 was evaluated by applying typical load cycling and start stop simulating protocols and it was found to be more durable than Pt/C.

From a performance point of view, Pt supported on carbon is still the best but less durable than metal nitrides and borides. However, Pt/LaB_6 shows great potential.

Table of Contents

List of Figures

List of Tables

Nomenclature

Symbols

Symbol	Unit	Description
A_E	cm^2	Electrode surface area
a	Å	Lattice constant
C	$mol.dm^{-3}$	Reactant concentration
d	Å	D-spacing
D	$cm^2.s^{-1}$	Diffusion coefficient
i	$mA.cm^{-2}$	Current density
i_d	$mA.cm^{-2}$	Diffusion limiting current density
i_K	$mA.cm^{-2}$	Kinetic current density
i_{disk}	mA	Current measured on the disk
i_{ring}	mA	Current measured on the ring
<L>	nm	Average crystallite size
N	%	Collection efficiency of the ring
n	-	Number of electrons
n	-	Number of cycles
r	-	Radius of particle size
SSA	$m^2.g^{-1}$	Specific surface area
$X_{H_2O_2}$ the	%	Hydrogen peroxide formed on ring
ω	rpm	Rotation speed of the electrode
ν	$cm^2.s^{-1}$	Kinematic viscosity
λ	nm	X-ray wavelength
θ	radius	Bragg's angle
β	-	Peak width

Constants

Constant	Value	Units	Description
F	96 485	Coulombs	Faraday's constant
K	1	-	Dimensionless crystallite shape factor

Glossary

Abbreviation	Description
AB	Acetylene black
H_{ads}	Hydrogen adsorption
HOR	Hydrogen oxidation reaction
COR	Carbon oxidation reaction
CV	Cyclic Voltammetry
H_{des}	Hydrogen desorption
ECSA	Electrochemical specific surface area
LSV	Linear sweep voltammetry
OMCVD	Organo-metallic chemical vapour deposition
MEA	Membrane electrode assembly
MPL	Micro-porous layer
OER	Oxygen evolution reaction
ORR	Oxygen reduction reaction
PEFC	Polymer electrolyte fuel cell
Pt	Platinum
Pt/C	Platinum supported on carbon
Pt/TiN	Platinum supported on titanium nitride
PT/TiB_2	Platinum supported on titanium diboride
Pt/LaB_6	Platinum supported on lanthanum hexaboride
RHE	Reversible hydrogen electrode
RDE	Rotating disk electrode

RRDE	Rotating ring disk electrode
SEM	Scanning electron microscopy
EDS	Energy dispersive spectrometry
SHE	Standard hydrogen electrode
TEM	Transmission electron microscopy
TGA	Thermogravimeteric analysis
XRD	X-ray diffraction

Chapter 1

1. Introduction

Polymer electrolyte fuel cells (PEFCs) are eco-friendly, powerful electrochemical energy converters, that can be operated with high energy density fuels and have a high efficiency compared to conventional power systems (Takasaki et al., 2011; Yin et al., 2010; Avasarala et al., 2009). Due to their viability, simplicity and quick start-up (Barbir, 2005), PEFCs have a wide variety of possible commercial applications, ranging from stationary backup power systems to automotive engines (Wang et al., 2011). Moreover, this technology can hold major economic benefits for South Africa, since all reactions in PEFCs are currently catalysed by platinum supported on carbon and South Africa has the largest platinum reserve in the world. However, due to poor durability and performance this technology has not been commercialised yet (Takasaki et al., 2011).

For PEFCs to be commercialized a lifespan of at least 5 000 h and 40 000 h of operation for automotive and stationary applications, respectively has to be achieved (Borup et al., 2007). The lifespan and the performance of the PEFCs is a major cost factor which mostly depends on the electrocatalyst and its support material (catalyst layer), since it is where electrochemical energy conversion takes place and it is one of the main spots of chemical and electrochemical degradation (Ramaswamy et al., 2008). Degradation of catalyst layers (Pt/C) is mainly attributed to two factors (i) electrocatalyst (Pt) dissolution during load cycling and (ii) corrosion of the support material (carbon) during start-up and shutdown of the fuel cell. Both factors result in loss of the electrochemical active surface area, hence poor performance and collapse of the MEA structure. Moreover, it has been reported that about 75% of performance losses are attributed to slow ORR kinetics on the cathode (Barbir, 2005).

Several mitigation strategies have been investigated, both on system and component level, in terms of complexity as well as the cost. A solution on the component level would always be preferred (Zhang et al. 2009). One approach taken by researchers in the field is to alloy Pt with other metals, such as Co and Ni to suppress Pt dissolution and improve ORR kinetics. Another is to support the electrocatalyst on alternative support materials, such as metal oxides, carbides, polymers, carbon nanotubes/fibers/aerogels, etc. However, so far none of these support materials has been successfully implemented in PEFC technology. There are major problems associated with the use of these materials, e.g. poor stability in acidic medium, insufficient electrical conductivity, or problems with Pt deposition. Therefore, the search for alternative supports must still continue to find better suitable materials that can withstand the corrosive conditions in the fuel cell, suppress Pt dissolution and improve ORR kinetics.

This research project will investigate the use of non-carbon based support materials as alternatives to carbon in an attempt to improve the durability and performance of PEFCs. The materials to be investigated are metal nitrides and borides, mainly due to their renowned superior mechanical and chemical properties compared to carbon. Electrochemical stability/durability and performance towards ORR will be investigated and compared to that of a commercial catalyst (Pt/C). The metal nitrides chosen for this study are titanium nitride (TiN) and zirconium nitride (ZrN); metal borides are titanium diboride (TiB_2), zirconium diboride (ZrB_2) and lanthanum hexaboride (LaB_6). Although TiN and TiB_2 have been studied individually, there is no systematic comparison of these materials.

Properties and application of these materials in PEFCs will be reviewed. Thereafter, objectives, hypothesis and limitations of this study will be discussed, followed by the proposed experimental procedure to test the validity of the hypotheses developed based on the objectives and the literature review. Experimental results obtained from this study will be reported and discussed. Lastly, based on these results, conclusions will be drawn and future recommendations will be made.

Chapter 2

2. Literature review

2.1 PEFC technology

PEFCs utilise hydrogen and oxygen as reactants to generate electrical power and the by-product is water, as shown in Fig. 2.1. When pure hydrogen is used as fuel, there are no greenhouse gases emitted during operation. Moreover, if hydrogen itself is produced from renewable sources PEFCs are considered as sustainable technology and a better alternative to other power producing systems.

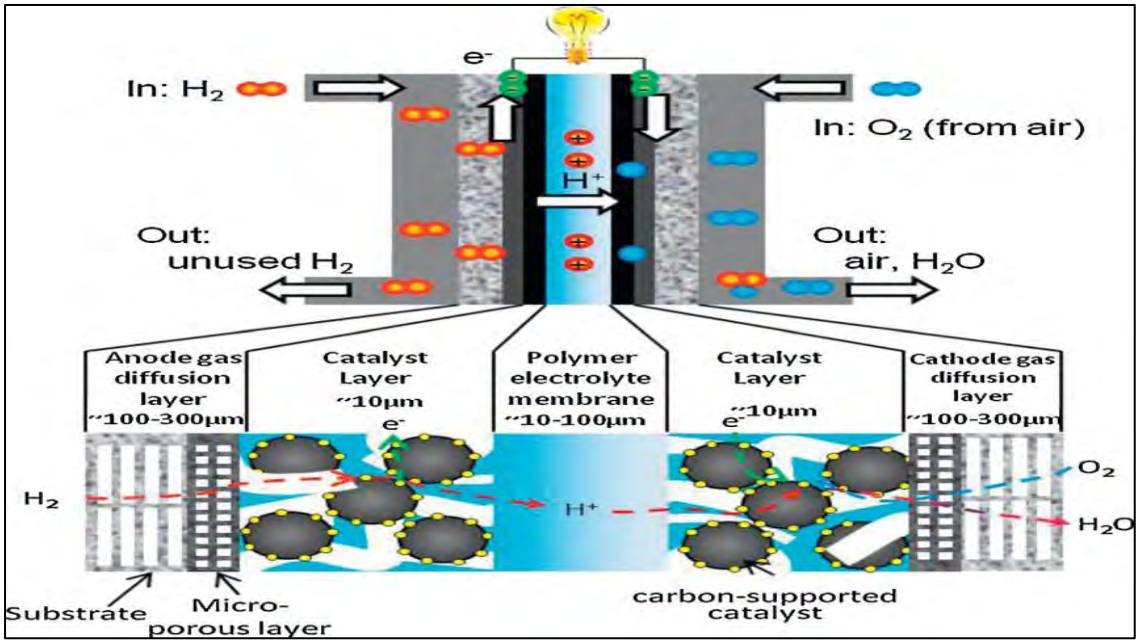

Figure 2.1 Schematic diagram of PEFC (Mishler et al., 2012)

At the anode, hydrogen is fed through a gas diffusion layer (GDL) and a micro-porous layer (MPL) into the catalyst layer, where the hydrogen oxidation reaction (HOR) occurs, via the following reaction:

$$\text{HOR: } H_2 \xrightarrow{Pt/C} 2H^+ + 2e^- \qquad E^0 = 0 \text{ vs SHE} \qquad (1.1)$$

Protons (H^+) that are generated from HOR are transported via the polymer electrolyte membrane to the cathode; and electrons (e^-) are conducted through the catalyst support material (as shown in Fig 2.1) to the MPL and GDL, then to the external circuit where it is available to do electrical work, as shown in Fig. 2.1.

On the cathode, oxygen reacts with the protons and the electrons from the HOR, this reaction is called the oxygen reduction reaction (ORR):

$$\text{ORR: } \tfrac{1}{2} O_2 + 2H^+ + 2e^- \xrightarrow{Pt/C} H_2O \qquad E^0 = 1.23 \text{ V vs SHE} \qquad (1.2)$$

The overall reaction of the fuel cell is:

$$H_2 + ½\ O_2 \xrightarrow{Pt/C} H_2O \qquad E^0 = 1.23\ V\ vs\ SHE \qquad (1.3)$$

HOR and ORR takes place in the so called 'three phase boundary' (TPB).

TPB consists of gas, ionomer and electrocatalyst surface, as depicted in Fig. 2.2.

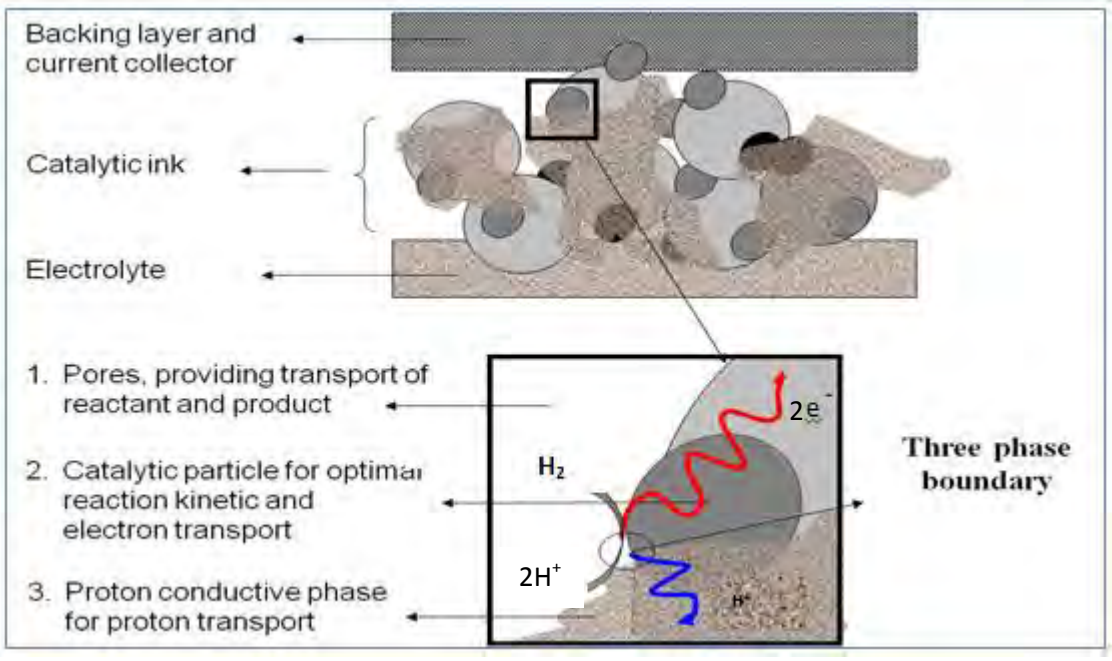

Figure 2.2 Schematic diagram of TPB (Adapted from Bladergroen, 2012)

The role of the ionomer on the TPB is to facilitate transfer of protons generated on platinum particles to the polymer electrolyte membrane; since protons have a very short diffusion length on carbon surfaces.

The role of carbon as the electrocatalyst support is to maximise utilisation of platinum in the fuel cell, by increasing the specific metal surface area. Conduct heat and electrons generated during the HOR, and to minimise mass transfer limitations

However, there are problems associated with the use of carbon as the support material. Carbon is susceptible to corrosion under PEFCs operating conditions (Takasaki et al., 2011; Yin et al., 2010; Avasarala et al., 2009, Kinoshita, 1988). Oxidation of the support materials has numerous adverse effects on the performance of the fuel cell.

2.1.1 Carbon corrosion

Kinoshita (1988) shows that in the electrolyte carbon corrodes via Incomplete oxidation by one electron transfer, resulting in formation of oxygenated surface species Eq. (1.4) and hydrolysis to form C_sO (s denotes surface species) (Eq 1.5) and lastly, It is the further

oxidation of C_sO to yield CO_2 Eq. (1.6), as shown in the following equations.

$$C \rightarrow C_s^+ + e^- \quad (1.4)$$

$$2C_s^+ + 2H_2O \rightarrow 2C_sO + 4H^+ + 4e^- \quad (1.5)$$

$$C_sO + H_2O \rightarrow CO_{2\,(g)} + 2H^+ + 2e^- \quad (1.6)$$

During start-up and shutdown of the fuel cell, conditions become extremely damaging, as the potential overshoots from the operating voltage (0.6 - 0.8 V) to approximately 1.5 V vs RHE on the cathode. This is caused by the phenomenon called 'air-fuel front'. During the shutdown of the PEFC, air diffuses into the anode as the gas supply is shut off. Therefore, during start up there is non-uniform distribution of hydrogen in the anode due to air front, as shown in Fig.2.3

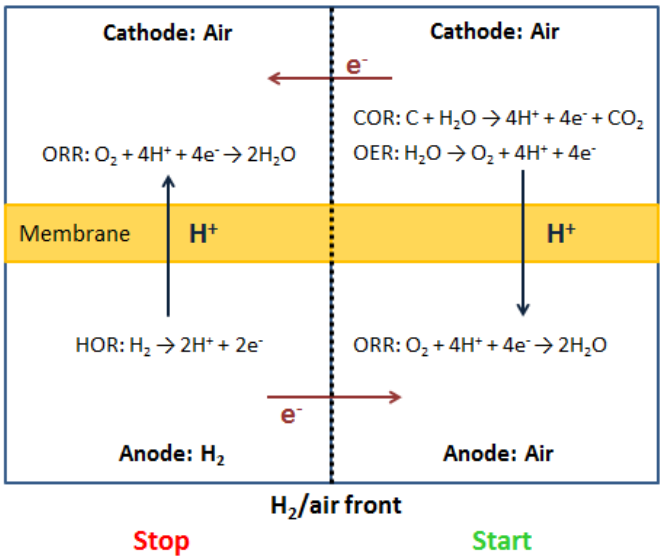

Figure 2.3 Schematic diagram of air-fuel front on PEFCs (adapted from Yu et al. 2006)

Air-fuel front drives ORR to occur on the anode, as the protons crossover into an oxygen rich sector (anode). Since there is no hydrogen on the cathode side to act as the source for the protons, protons therefore are generated in an oxidation reaction from water (either from direct oxidation of water (eq.1.8) or via oxidation of carbon (eq. 1.7)). These reactions drive the potential in the cathode to above 1.5 V.

Carbon oxidation reaction (COR): $C + 2H_2O \rightarrow CO_2 + 4H^+ + 4e^-$ $E^0 = 0.207$ V vs RHE (1.7)

And electrolysis reaction also takes place on the cathode.

Oxygen evolution reaction (OER): $2H_2O \rightarrow O_2 + 4H^+ + 4\,e^-$ $E^0 = 1.229$ V vs RHE (1.8)

In addition to air-fuel front, carbon oxidation may be induced by gross fuel starvation. When micro channels on bipolar plates are blocked, gases cannot flow through or uneven gas distribution on the stack between cells may be resulted. This effect raises the potential on the anode. Consequently, the cell potential drops and forces the cell to operate on the reverse mode, to provide H^+ and e^- for ORR at the cathode, as shown above in Fig 2.3 (Zhang et al., 2009; Ralph et al., 2006).

Furthermore, in the fuel cell heterogeneous water-gas shift (WGS) reaction occurs, and is catalysed by Pt:

$$C + H_2O \leftrightarrow CO + 2H^+ + 2e^- \qquad E^0 = 0.518 \text{ V vs RHE} \qquad (1.9)$$

According to Stevens & Dahn (2005) this reaction may be accelerated by increasing platinum loading on carbon, since there is more interfacial area between platinum and carbon (Baturina et al., 2006).

2.1.2 Consequences of carbon oxidation

Oxidation changes the morphology and surface chemical properties of carbon. For example, a loss in hydrophobic character results from the formation of oxygen containing groups such as phenol, carbonyl, carboxyl and carbonyl groups from C_s^+ produced in Eq. 1.4. The presence of these groups on the surface also inhibits electron conductivity and weakens Pt-C interaction (Avasarala, 2010).

Weakening of Pt-C interaction leads to (i) Pt particle detachment from the support (ii) Pt dissolution and (iii) agglomeration of Pt particles via sintering. All of these mechanisms, as shown in Fig 2.4, result in a loss of electrocatalyst active area (ECSA) and poor ORR kinetics.

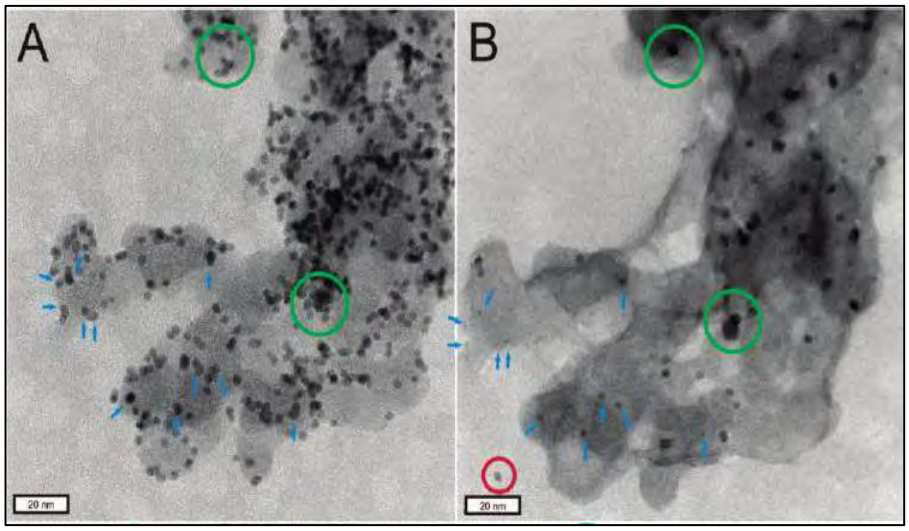

Figure 2.4 Catalyst changes before (A) after 3600 cycles (B), showing detached Pt particles(red circles), reduction of Pt particle size due to dissolution (blue arrows) and agglomeration of particles (green circles) (Meier et al., 2012).

As shown in Fig 2.4, platinum nanoparticles are detached from the support under load cycling. The effect of Pt dissolution is observed, by reduction in size of Pt nanoparticles and it is well known that platinum nanoparticles have very high surface energy and tend to agglomerate to form larger particles to minimise the energy of the system (Asoro et al., 2010). Therefore, strong Pt-support interaction is required to minimise this effect, since the loss of ECSA directly affects the performance of the fuel cell. Moreover, Pt^{2+} generated species migrate to the membrane and are reduced by hydrogen (crossover hydrogen), and precipitate as Pt particles on the membrane. These particles may react with crossover hydrogen but since they are isolated (not in contact with the support) produced electrons accumulate on the membrane and reduce the stability of the membrane (Ferreira et al., 2005). Therefore, it is essential to deposit Pt on the support that could possibly suppress Pt dissolution.

Furthermore, degradation of the support carbon leads to structural collapse of the MEA, as shown in Fig. 2.5.

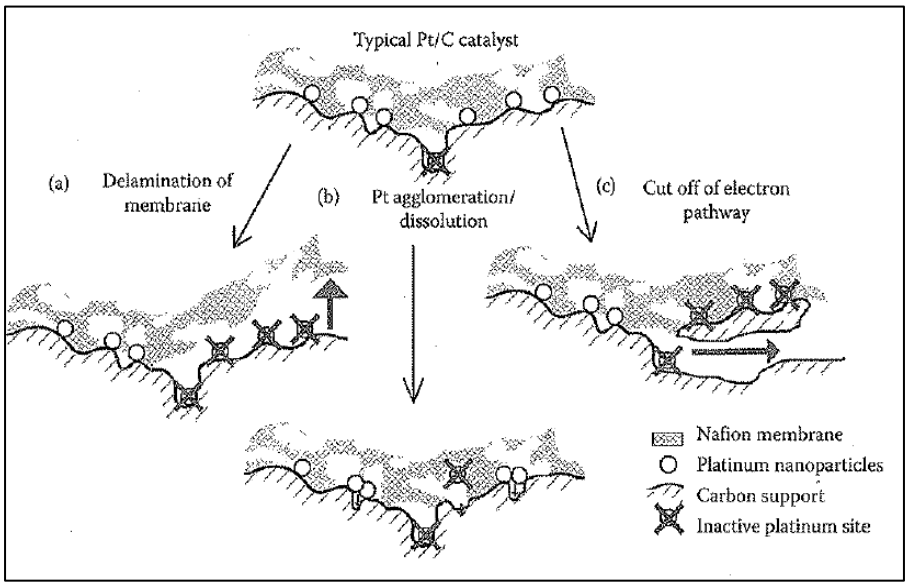

Figure 2.5 Effects of carbon degradation on catalyst layer (Wang et al., 2011)

During carbon oxidation, delamination of the catalyst layer from Nafion membrane is observed, which disrupts transfer of protons to the cathode and there is a cut off of electron pathways as shown in Fig 2.5 (c).

2.1.3 Activity losses in PEFCs during operation

The theoretical equilibrium achieved at Standard Ambient Temperature and Pressure (SATP) is 1.23 V. However, in practise, fuel cells are not operated under equilibrium conditions and the operating potential is lower due to activation, ohmic (resistance) and mass transfer losses (Barbir, 2005). This is illustrated in the polarisation curve, shown in Fig 2.6

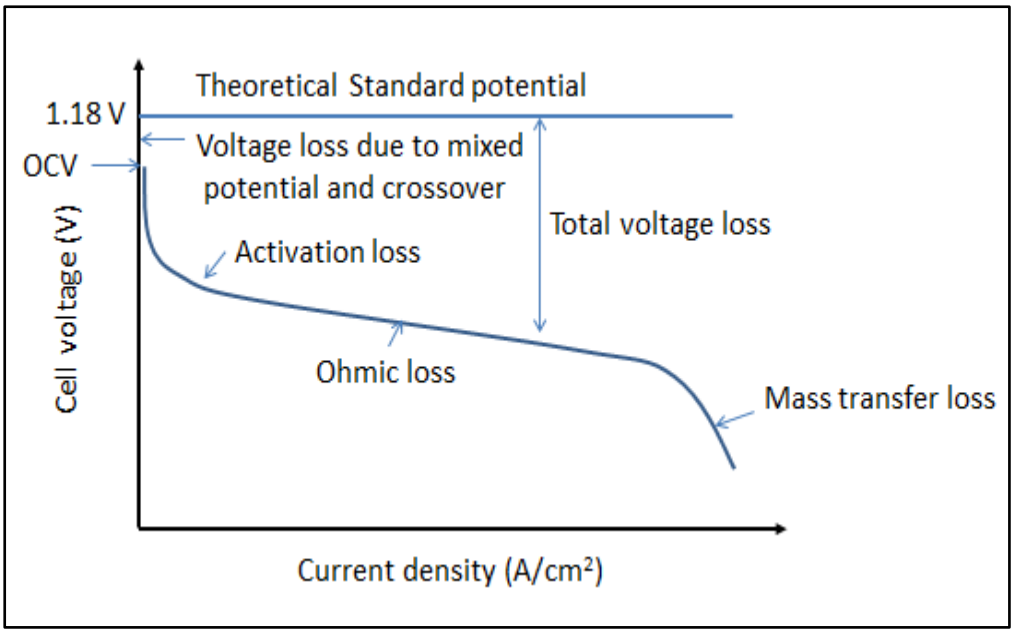

Figure 2.6 Typical polarisation curve showing performance losses in an operating PEFC (adapted from Jiang et al., 2011)

Activation losses are by far major losses in the system at any current density (Barbir, 2005), as it is the energy required to overcome the electrochemical energy for ORR and HOR. However, these losses are dominant in the cathode due slow ORR kinetics.

Ohmic losses are attributed to resistance of flow of ions in the membrane and electrons on the electrocatalyst support material. Lastly, the concentration losses occurs both at the anode and cathode, whenever there is a change in concentration of reactants on the electrode/catalyst layer during operation (Larminie & Dicks, 2003).

2.1.4 Basic requirements for alternative support materials

Due to the shortcomings of carbon as the electrocatalyst support material, there is an urgent need for alternative supports. It is one of the mitigation strategies to improve performance, durability and efficiency, so that PEFCs could be commercialized. The body of literature points to a very strong dependence of the performance and durability on the electrocatalyst support materials. (Sharma & Pollet, 2012; Nicole, 2001, Avasarala et al., 2009; Ham and Lee, 2009)

From the above factors on durability, for the material to be considered as an alternative, it must (Sharma and Pollet, 2012):

- Exhibit high corrosion resistance, under strongly acidic conditions and frequent potential cycling,
- Have high electrical conductivity to minimise ohmic losses,
- Have a reasonable thermal conductivity to remove heat from reaction centers,

- Have a large surface area and a meso-porous structure to allow for effective mass transfer and to accommodate the ionomer. That is required to maximise the three-phase boundary,
- Promote catalytic properties of platinum, and
- Provide the right combination of hydrophobicity and pore size distribution to aid in the effective management of water in the electrode layer.

In addition, it would be ideal to find a support that suppresses Pt dissolution and formation of hydrogen peroxide. The study by Inaba et al. (2006) showed that Pt supported on carbon forms a significant amount of peroxides. Some of these peroxides form reactive oxygen radicals in the presence of impurities such as Cu^{2+} and Fe^{2+} in the PEFC and reduces the stability of the membrane.

2.2 Alternative support materials for PEFCs

Shortcomings of carbon as the electrocatalyst support material in PEFCs has been briefly discussed in the previous section and demonstrated how it affects fuel cell durability and performance. A variety of carbon-based materials, such as carbon nanotubes, carbon nanofibers, graphene, carbon aerosol and boron doped diamonds, polymers and inorganic materials (metal oxides, carbides, nitrides and borides) have been considered as alternatives (Shao et al, 2008; Antolini & Gonzala, 2009; Sharma & Pollet, 2012). However, none has been implemented in PEFCs to date. Below is a concise overview of current results in the area.

(i) Carbon based materials

It has been reported (Yin et al. 2010, Antolini et al., 2009) that carbon nanotubes, carbon nanofibers and graphene require pre-oxidation with strong acids such as HNO_3, for platinum deposition, as the surface is extremely inert. However, it has been reported (Antolini et al.,2009) that pre-oxidation treatment reduces electrical conductivity and surface stability. Moreover, carbon nanotubes/nanofibers tend to tangle in solution and yield non-uniform dispersion. According to Shioyama et al. (2005), improved ORR kinetics and durability were observed in comparison to Pt/C. However, these materials do not inhibit carbon corrosion, but rather reduce the rate (Antolini et al., 2009; Yin et al., 2010), as shown in Fig. 2.15 (section 2.3.4), where the durability of Pt supported on graphitised carbon black and carbon black is compared (Kakinuma et al., 2012) Carbon aerogels are amorphous and were found to be unstable under fuel cells applications, due to a low degree of graphitization. Furthermore, Pt utilisation was found to be less than 25% and this was attributed to the fact that Pt nanoparticles were buried in pores (Antolini et al., 2007). Nanodiamonds were investigated as support due to renowned high electrochemical stability, wide potential window and low background current. However, they do not conduct electricity, therefore, doping with a p- or n-type dopant is required. Even though doping increases conductivity, it also decreases stability of the material (Shao et al., 2008; Sharma and Pollet, 2012).

(ii) Polymers

The search for alternatives has gone as far as the use of polymeric materials due to their high corrosion resistance and ease to be manufactured into any form (such as meso-porous nanofibers, nanotubes, platelets etc.) at a low cost. It has been reported that polymers conduct both protons and electrons (i.e no need for addition of ionomer on the catalyst layer) and are gas and water permeable. Huang et al. (2009) studied electron conducting polypyrrole as an electrocatalyt support material in PEFC and discovered that Pt/PPy is stable up to 1.8 V, outperformed Pt/C in terms of ORR and was 40% more durable. However, further development is still required for this material to be used in PEFCs. Polymers are very temperature sensitive and may be subjected to thermal shock under fuel cell operation and their dimensions may change due to swelling when there is excessive water present inside the fuel cell.

(iii) Metal oxides

Various metal oxides have been studied, such as n-type semi-conductors SnO, WO_x, ZrO_2 and Ti_xO_y. Some of the major findings were that SnO_2 supresses platinum dissolution under load cycling and this was attributed to strong metal support interaction. ORR kinetics were improved due to the same interaction effect. However, Reeve et al. (2007) showed that ORR activity deteriorates in acidic media since oxides have strong redox properties in an acidic environment.

A number of authors have improved oxidation resistance of metal oxides by doping. Chhina et al. (2007) and Takasaki et al. (2011), as an example, improved the oxidation resistance of SnO_2 with the addition of indium to form indium tin oxide (ITO), however ORR results were not reported for this hybrid support. Takasaki et al. (2011) doped SnO_2 with Sb^{5+}/ Nb^{5+} to increase electron conductivity and found that Pt/Nb-SnO_2 maintained its initial ECSA over 60 000 cycles. Doping also significantly improved ORR kinetics but Pt/C still showed better performance by 50%.

Tungsten oxide was considered as well, due to its multiple oxidation states (2-6), making it suitable for PEFCs. Oxygen vacant defects on the lattice makes WO_X conductive (Chhina et al., 2007; Supothina et al. 2007). In addition, it has been claimed that WO_x conducts protons as well, due to formation of tungsten trioxide hydrates (Nakajima et al., 2002). However, tungsten undergoes dissolution under load cycling in acidic medium. Proton conductivity was observed on S-ZrO_2 as well. Surface treatment of zirconia with sulfonic acid makes zirconia a strong superacid. Hara & Miyayama (2004) discovered that S-ZrO_2 with high S:Zr ratio had significantly high H^+ conductivity. Suzuki et al. (2007) tested Pt/S-ZrO_2 with no addition of ionomer and higher ORR performance was observed compared to Pt/C without ionomer. This shows that oxides may reduce the amount of ionomer required on the catalyst layer.

Titanium oxide (TiO_X, x>1) is very stable, however, it has very poor conductivity and requires doping with hypervalent species such as Sb^{5+} and Nb^{5+} just like SnO_2. Sun et al. (2012) found

that Pt/Nb-TiO_2 outperformed Pt/C and this was attributed to better metal dispersion on the oxides and higher durability was obtained. However, titanium may form oxides with homologous series Ti_nO_{2n-1} ($4 \leq n \leq 10$), which is known as Magneli phases. Ti_4O_7 is the most common and exhibits exceptional electrical conductivity $<10^3$ S cm^{-1} and oxidation resistance in 1 M sulphuric acid up to 2 V vs. RHE. However, Loroi et al. (2005) found that Pt/Ti_4O_7 has a low mass activity compared to Pt/C.

(iv) Metal carbides

Some metal carbides are chemically stable in acidic medium and have exceptional mechanical durability (Liu et al., 2013). Tungsten carbide has been intensively studied, due to surface reactivity that is similar to Pt. Zellner (2004) found that the W_2C phase was unstable at potentials greater than 0.4 V but WC was stable via formation of surface oxides which prevents further oxidation of the bulk material.

Liu and Mustain (2012) tested Pt/WC for ORR, with a higher activity and a shift on the ORR half-wave potential have been observed, which is likely to occur when there is a synergistic effect between the active metal and the support. However, after several cycles the activity dropped due to the presence of surface oxides (WO_X). Several other carbides have been studied, such as carbides of molybdenum, vanadium, iron and titanium. Ignaszak et al. (2011) reported that titanium carbide oxidises at potentials above 0 V vs. RHE, but Pt supported had an ORR activity greater than of a commercial catalyst (Pt/C). Molybdenum, vanadium and iron carbides are reported to have high ORR activity as well (Hu et al., 2011; Lui et al., 2013) but no reports on electrochemical stability could be found.

(v) Metal nitrides and borides

There have been few reports on metal nitrides and borides as alternative, but there is no systematic study. This current study will focus on them and therefore they are discussed in more detail in the following sections.

2.3 Metal nitrides

2.3.1 Physicochemical properties of metal nitrides

Transition metal nitrides (TMNs) are ceramic materials with high thermodynamic stability, hardness, and corrosion resistance due to the presence of a triple covalent bond between the metal and nitrogen. Metal nitrides from group 4-6 are reported to be more stable and active, than those of Group 7-10. The stability decreases with increasing group number from Group 4, as the lattice of high group number cannot accommodate interstitial nitrogen atoms while maintaining its own close-packed metal atoms (Ham& Lee, 2009). Therefore, group 4 metal nitrides are the most stable.

Group 4	Group 5	Group 6	Group 7	Group 8	Group 9	Group 10
Ti	V	Cr	Mn	Fe	Co	Ni
Zr	Nb	Mo	Tc	Ru	Rh	Pd
Hf	Ta	W	Re	Os	Ir	Pt

Thermodynamic stability stable nitrides unstable nitrides

Figure 2.7 Transition metals from group 4-10 showing thermodynamic stability

In addition, Group 4 nitrides have exceptional thermal and electrical conductivity compared to carbon ($1.2*10^3$ S m^{-1}), as shown in Fig. 2.8. ZrN has single crystal electrical conductivity of 3.3×10^6 S m^{-1}, and TiN has conductivity of 1.18×10^6 S m^{-1}(Kosolapova, 1986).

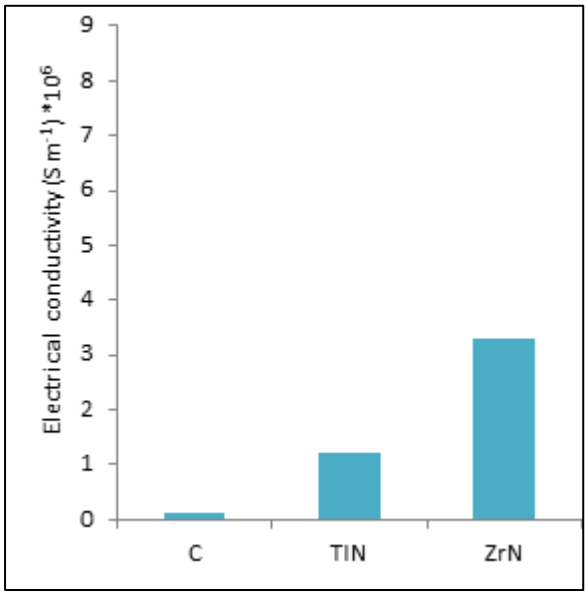

Figure 2.8 Electrical conductivity of metal nitrides and borides of study (adapted from Kosolapoza, 1986)

Metal nitrides (AB nitrides) have a cubic crystal structure, with nitrogen atoms at the interstitial sites of the metal, as shown in Fig. 2.9.

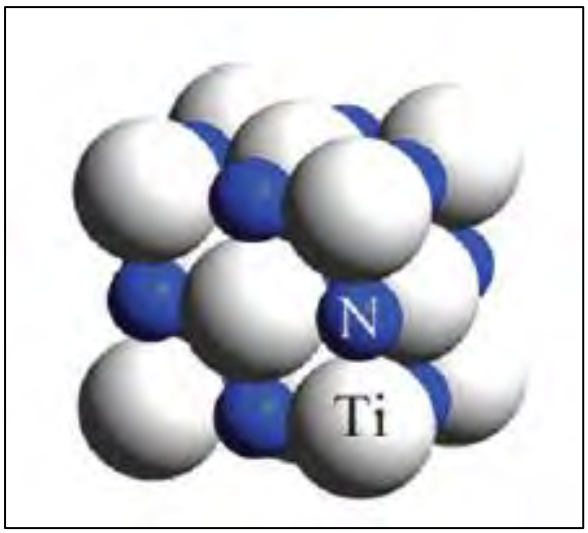

Figure 2.9 Model of ZrN / TiN crystal structure (Zhang et al., 2012)

During formation of metal nitrides the d-band of the metal is narrowed, as a result, metal nitrides have a similar electronic structure as Pt up to Fermi level. Above Fermi level, unfilled orbitals of the metal are broadened, increasing the density of empty orbitals, as shown in Fig 2.10.

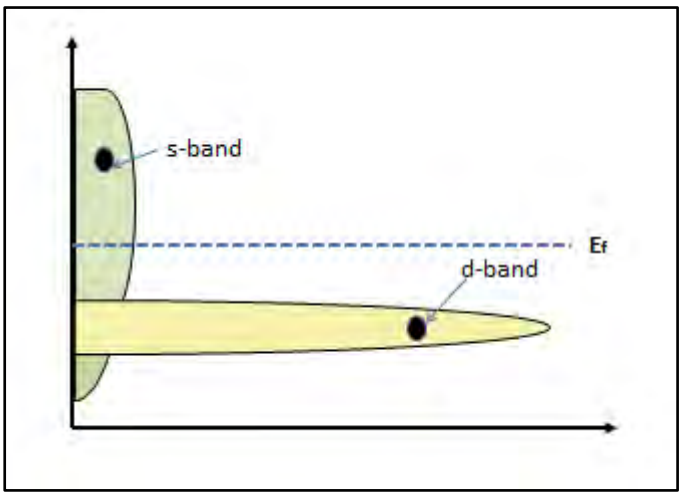

Figure 2.10 Illustration of the density f states of metal nitrides showing the d-band and s-band near Fermi level (adapted from Liu et al. 2013)

These changes in the d-band induce transfer of the metal's *s*- and *d*-orbital electrons to the *2p*-orbital of nitrogen, reducing electron population in d-orbital of the metal**.** Shortage of electrons in the *d*-orbital near the Fermi level prevents metal nitride surfaces to donate *d*-electrons to adsorbents. Furthermore, high electrical conductivity of metal nitrides arises from the transfer of one unpaired electron to metal localised *sp* hybrid orbital of the metal, resulting in non-zero electron density at Fermi-level (Avasarala et al., 2010)

Metal nitrides act similar to noble metals for electrochemical reactions such as HOR, methanol oxidation and ORR since they have a similar band structure as PGMs up to the Fermi level. When metal nitrides are combined with PGMs, electrocatalytic synergy is expected (Ham and Lee, 2009), which is why metal nitrides were selected for this study. Metal nitride may increase ORR kinetics and reduce the amount of Pt needed in the fuel cell (Kakinuma et al., 2012). The amount of Pt loaded on the cathode may be significantly reduced due to eletrocatalytic synergy effect.

2.3.2 Electrochemical oxidation of metal nitrides

2.3.2.1 Titanium nitride

High oxidation resistance of TiN in wide pH ranges has been reported by Avasarala et al. (2010 & 2011). High resistivity towards oxidation is attributed to the formation of a nitrogen rich, titanium oxynitride surface layer (Avasarala et al., 2010). The oxynitride layer is very electron dense and inhibits further oxidation of underlying titanium (Verkhoturov et al., 1988; Milosev et al., 1995). The presence of oxynitrides on the surface of TiN was confirmed by Avasarala et al. (2010) using X-ray diffraction (XRD) and X-ray photoelectron spectroscopy (XPS). TiN and Titanium oxide have lattice constants of 4.41 Å and 4.18 Å, respectively. Titanium oxynitride is the intermediate phase and its lattice constant lies between of TiN and Titanium oxide according to Vegard's law. The calculated lattice constant was found to be 4.212 Å, using Bragg's angle of the (111) diffraction plane; this confirms the presence of oxynitride phase on the surface of TiN. In addition, XPS confirmed the presence of this passive layer. In the spectrum a deconvolution of the Ti $2p_{3/2}$ emission band showed an additional peak between the nitride and oxide peaks due to the presence of oxynitride, with the oxidation state between TiN and TiO_2.

Between 0.5 V-0.9 V vs RHE TiN surface oxidizes via the following reaction to form TiO_2:

$TiN + 2H_2O \rightarrow TiO_2 + ½\ N_2 + 4H^+ + 4e^-$ (2.1) (Avasarala et al., 2010)

There have been concerns about the presence of the oxide/oxynitride reducing electron conductivity. However, Avasarala et al., (2009) reported that there are no ohmic losses observed on the ORR curve of Pt/TiN which are attributed to the presence of oxynitrides/oxides. As a matter of fact Pt/TiN showed better ORR performance in comparison to Pt/C, as shown in Fig 2.15 (b). If electron conductivity was inhibited by oxynitrides/oxides, retardation in kinetics could have been observed. Avasarala et al. (2010) reported that the surface of TiN is not dominated by TiO_2, but exists as a Magneli phase (i. e. a mixture of suboxides with a composition of the general formula Ti_nO_{2n-1}, which is able to conduct electrons). Furthermore, it is suggested that with increasing oxygen content on the surface of TiN at high potentials, TiO_2 is formed which rapidly undergoes dissolution in acids (Fig. 2.11). Dissolution of oxides was noted by the changes in open circuit potential (OCP) of TiN. The downwards shift of OCP values was observed in 0.5 M sulphuric acid over time. This shows that oxynitrides and oxides underwent dissolution and a new TiN surface was

exposed into the acid and a new oxynitride layer was generated. Moreover, the oxynitrride (TiO_xN_y) is partly metallic due to lower oxygen content, and has a crystal structure similar to of TiN, which is why it is able to conduct electrons.

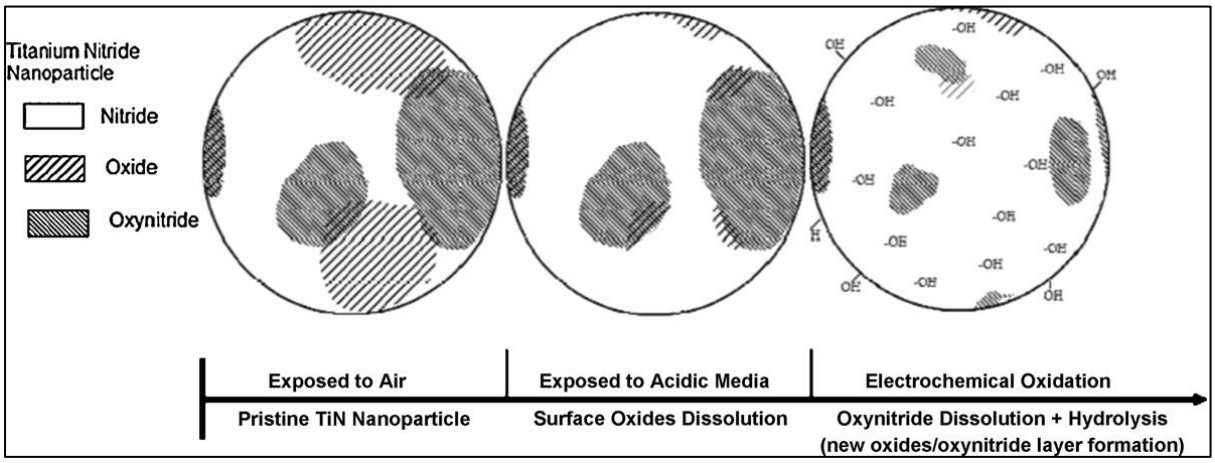

Figure 2.11 TiN nanoparticles exposed to different conditions in the fuel cell (Avasarala et al., 2010).

Detailed studies by Avasarala et al. (2010) elucidated the formation of hydroxides and hydrated oxides and concluded that TiO_2 forms at a potential of 0.5 to 0.9 V vs SHE whereas hydroxides are formed at higher potentials. They also concluded that the oxide formation provides a degree of protection from further oxidation to the underlying TiN. CV profiles of TiN and carbon in 0.1 M $HClO_4$ are shown below (Fig 2.12).

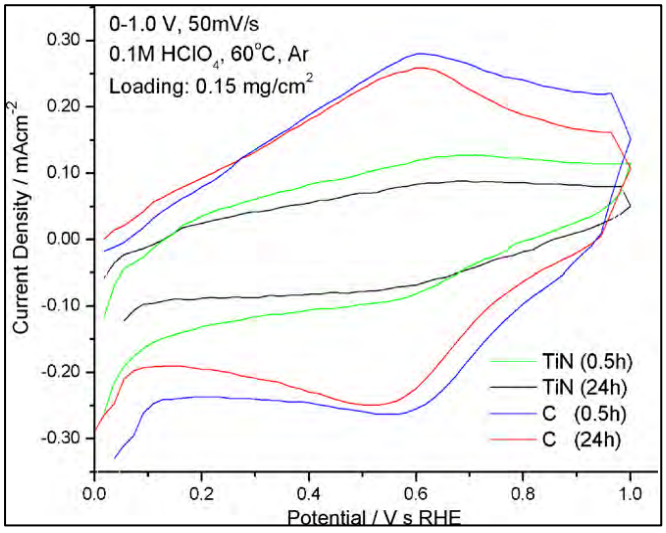

Figure 2.12 Cyclic voltammogram (CV) of TiN and carbon, conditions: Ar saturated 0.1 M $HClO_4$, 60 °C, cycling from 0.0 - 1.0 V vs SHE, 50 $mV.s^{-1}$ (Avasarala et al., 2010)

In Fig 2.12, the current density generated by TiN is lower than that of carbon under similar testing conditions. The presence of an oxide/oxynitride layer on the surface does prevent further oxidation of the material. The small oxidation and reduction current observed

between 0.5-0.6 V vs RHE, is due to surface oxidation of TiN to form a passive layer. A major current drop is observed after 0.5 h and thereafter the current has the same magnitude, showing that passivation of the material occurred very early and was sustained throughout the experiment, whereas carbon is constantly undergoing oxidation.

In addition, Avasarala et al. (2011) showed that oxidation only occurs on the surface of metal nitrides using XPS depth profiling by sputtering the surface with Ar ions.

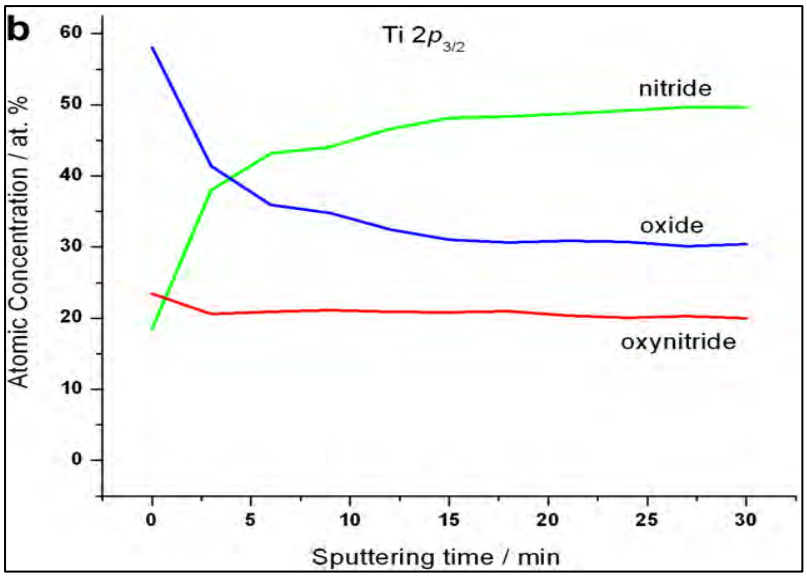

Figure 2.13 Relative atomic percentage concentrations of surface elements of treated and untreated TiN samples from XPS Avasarala et al. (2011).

As shown on the figure above (Fig 2.13), the oxide and oxynitride rapidly decreased with a corresponding increase of nitride. After 5 min of sputtering the plateau was reached, indicating that although surface oxidation took place, the underlying material was still predominantly TiN.

2.3.2.2 Zirconium nitride

Although zirconium nitride has similar properties as TiN, there is not much literature documented on oxidation of this material for fuel cells applications as the support material. This material is widely used in coatings due to excellent corrosion resistance. Cunha et al. (2006), claimed that at low O_2 content ZrN surface oxidation occurs to form oxynitrides $Zr(NO)_X$, similar to TiN. As shown above the titanium oxynitride layer prevents further oxidation of underlying material. Doi et al. (2006) tested the chemical and electrochemical stability of zirconium oxynitride at 30 °C in N_2 saturated 0.1 M sulphuric acid for 72 hours and potential cycling in the 0.05 – 1.0 V potential range in N_2 saturated 0.1 M sulphuric acid at 30 °C, respectively. The main findings were that zirconium oxynitride is chemically stable as very minimal amount of Zr ions were measured by ICP. Moreover, the material is electrochemically stable as no reduction nor oxidation peaks were observed at this potential range. However, if pre-oxidation does not occur on ZrN surfaces to form oxynitride, it is not

known how this material (ZrN) will behave under fuel cell conditions. The Pourbaix diagram of the Zr-H_2O system (Fig. 2.14) shows that at fuel cell relevant potentials Zr can only form protective layers at pH > 3, and below pH 3 Zr is subjected to corrosion.

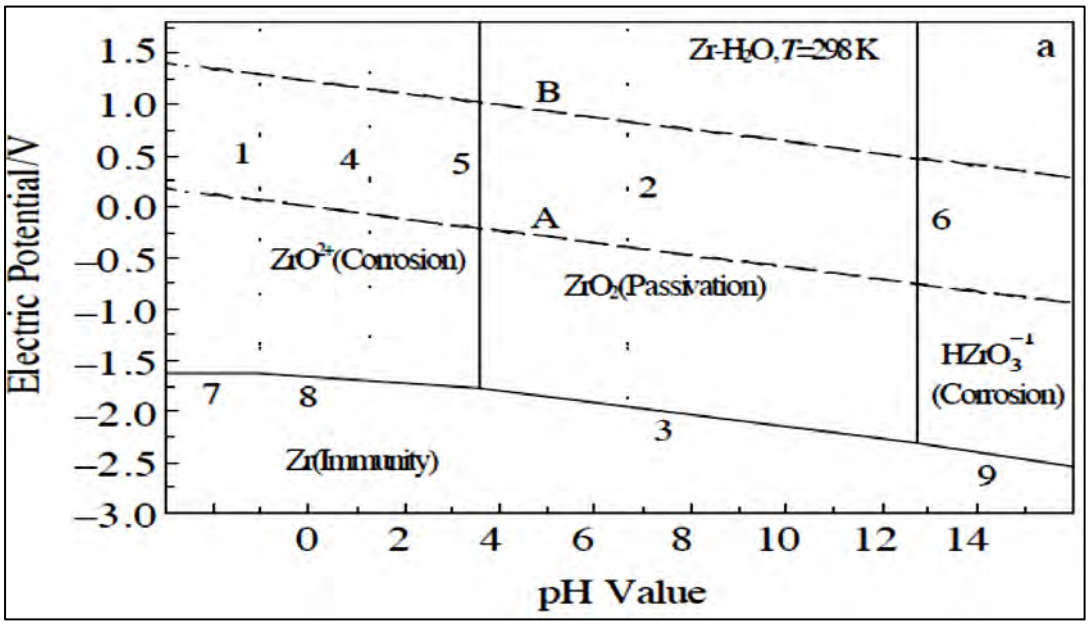

Figure 2.14 Pourbaix diagram of Zr-H_2O over a wide pH of zirconium in water at 25°C (Chen et al. 2004)

2.3.3 Electrocatalyic activity of Pt supported on metal nitrides

Avasarala et al. (2009) evaluated TiN as the electrocatalyst support material. The polyol method was used to deposit 20 wt% Pt on TiN using hexachloroplatic acid (H_2PtCl_6). The resulting catalyst was compared with a commercial catalyst 20 wt% Pt/C catalyst. Tests were performed under identical conditions and the mass of Pt on the glassy carbon disk was the same for both catalysts. The ECSA and activity results for both catalysts are tabulated below (Table 2.1).

Table 2.1 ECSA, specific activity (i_s), and mass activity (i_m) of Pt/TiN and Pt/C from CV and ORR measurements (Avasarala et al., 2009)

	20 wt% Pt/C	20 wt% Pt/TiN
ECSA (m^2/g_{Pt})	68.7	75.6
Mass activity (mA.mg-1Pt), i_m		
0.9 V	6.2	16.4
0.8 V	90.6	294.2
0.7 V	586.2	1221.4
Specific Activity (µA.cm-2Pt),i_s		
0.9 V	9.1	21.7
0.8 V	131.8	389.2
0.7 V	853.3	1615.6
[a] Catalysts were supported on glassy-carbon disk electrodes (for Pt loading of 20µg_{Pt}/cm^2) and tested in 0.1 M $HClO_4$ at 60 °C.		

As shown in Table 2.1, Pt/TiN showed higher ECSA and Avasarala et al. (2009) claimed that this was due to more catalytically active Pt sites on TiN , as the TEM image showed high Pt particle density. Furthermore, Pt/TiN showed better ORR activity as shown in Table 2.1. The mass activity of Pt/TiN is ca. 3.5 times more than that of Pt/C with the same amount of Pt loading and it was speculated that this was due to metal-support interaction and TiN acting as the promoter for electrochemical reactions.

Kakinuma et al. (2012) also conducted a study on Pt/TiN but the loading was different (shown in table 2.2) and the catalyst was prepared via a colloidal method, using H_2PtCl_6. The resulting Pt particles had an average size of 2.2 ± 0.3 nm and were hexagonal in shape. In addition to that, 20 wt% acetylene black (AB) was added to the batch to enhance electron conductivity of Pt/TiN. All results are tabulated in the table below (Table 2.2).

Table 2.2 ECSA and mass activity of electrocatalysts (Kakinuma et al., 2012)

catalyst	**Pt/Titanium nitride+acetyl black**	**Pt/Titanium nitride**	**Pt/graphitized carbon**	**Pt/carbon black**
Pt (wt%)	7.00	8.80	46.1	47.9
Pt mass activity/Ag^{-1}	562	522	407	527
Pt ECSA m^2g^{-1}	79.2	58.9	83.1	80.7

The results of Kakinuma et al. (2012) are consistent with Avasarala et al. (2009) for Pt/TiN catalyst. Pt/TiN outperformed Pt/C. Furthermore, it can be seen that addition of electrical conducting acetylene black improved ECSA and ORR kinetics. However, since Avasarala et al. (2009) did not report the use of AB and yet observed a substantial improvement, it is not clear why the report of Kakinuma et al. (2012) shows that AB improves it, when their data merely shows equivalent performance to Pt/C.

2.3.4 Electrochemical stability of Pt/metal nitrides

Kakinuma et al. (2012) conducted durability tests on Pt/carbon black (CB), Pt/graphitized carbon black (GCB), Pt/TiN and Pt/TiN+ AB, results are shown in Fig. 2.15.

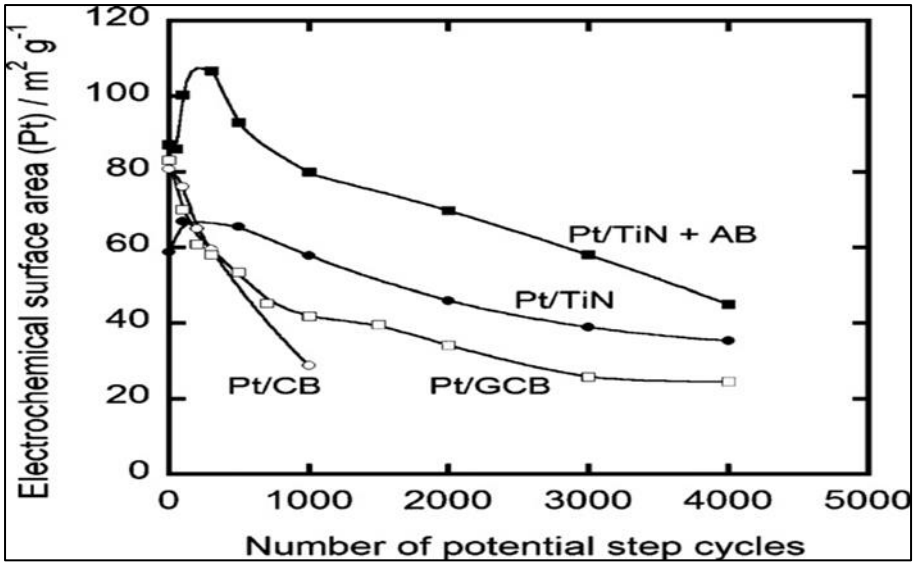

Figure 2.15 ECSA of Pt/TiN, Pt/TiN+acetyl black (Pt/TiN+AB), Pt/graphitized carbon (Pt/GC) and Pt/Carbon black (Pt/CB) under load cycling at 25°C in 0.1 M $HClO_4$ (Kakinuma et al., 2012)

Kakinuma et al., (2012) found that Pt/TiN and Pt/TiN + AB was more durable compared to carbon based supports. This was attributed to encapsulation of Pt particles by the support and stronger Pt-support interaction, which restrained Pt migration and sintering. Hence, there were minimal ECSA losses.

2.4 Metal borides

2.4.1 Physicochemical properties of metal borides

Metal borides are widely used as protective coatings in various applications, due to their exceptional chemical stability in oxidising conditions. In addition, these materials have excellent thermal stability and conductivity, which are essential properties for electrocatalyst support materials (Yin et al., 2010). Furthermore, TiB_2, ZrB_2 and LaB_6 have exceptionally high electrical conductivity compared to carbon and the metal nitrides of this study as shown in Fig 2.16.

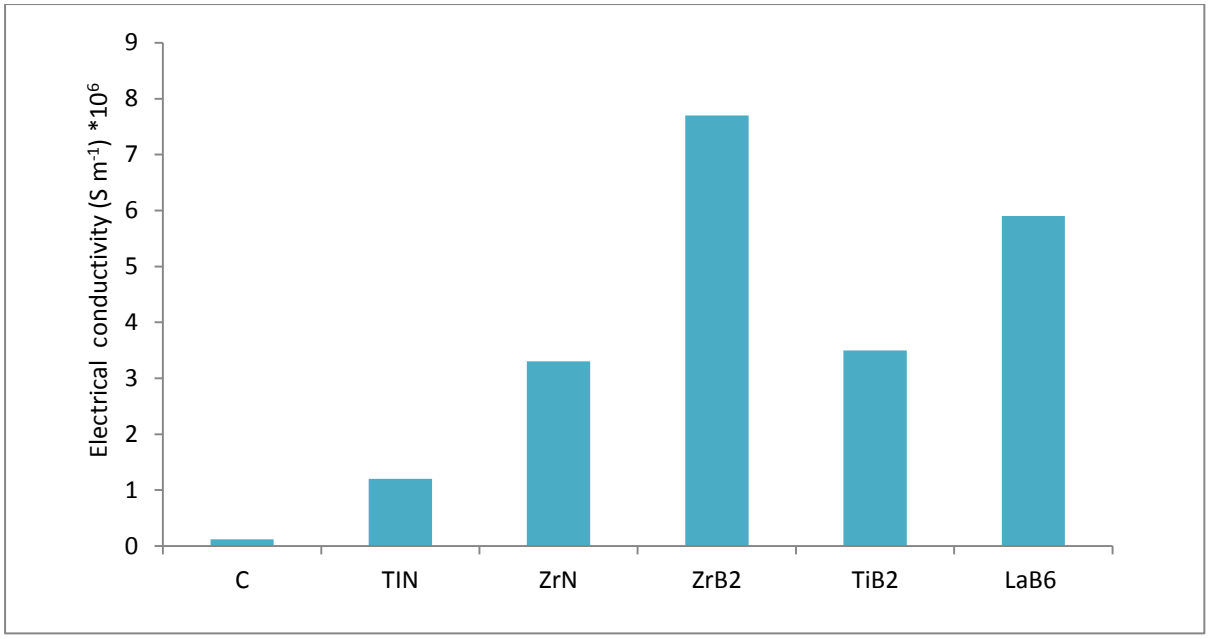

Figure 2.16 Electrical conductivity of metal nitrides and borides of study (data taken from Kosolapoza, 1986)

Titanium and zirconium diboride have a crystal structure that compromises of covalent hexagonal boron networks, similar to graphene layers and the metal atoms are situated between individual layers of boron , as shown in Fig.2.17. Based on band structure calculations, Zhou et al. (2006) argue that the electronic conductivity is mainly due to in-plane conduction.

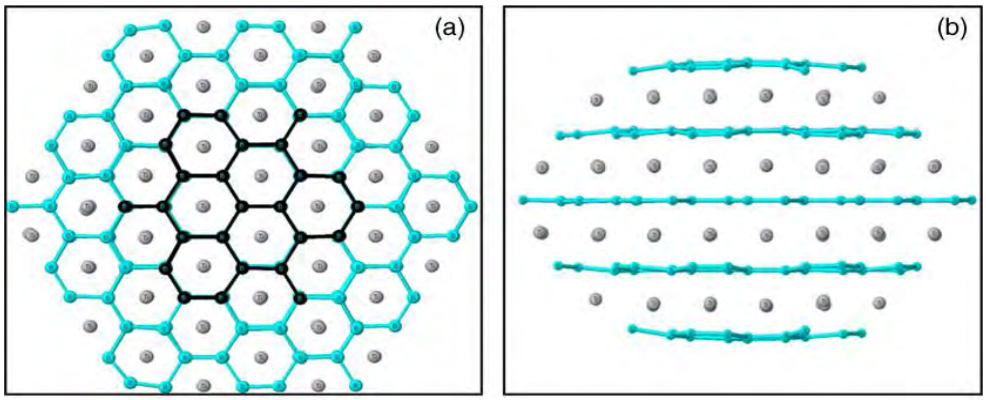

Figure 2.17 (a) top view and side view of TiB_2/ZrB_2 (Volonakis et al.2011)

Similar to metal nitrides, the stability of metal diborides decreases with increasing group number, due to filling of the d-orbitals. Therefore, only group 4 transition metals were selected for this study (Ti and Zr).

Volonakis et al. (2011) studied adsorption of H_2, H_2O and O_2 on TiB_2 surfaces *ab initio*, and found that TiB_2 surfaces favour adsorption of H_2 and O_2 molecules but not H_2O. This shows

that TiB_2 may enhance ORR and HOR kinetics by facilitating H_2 and O_2 adsorption on Pt nanoparticles.

Metal hexaborides are superconductors with unique properties such as the electronic structure. This material has a cubic crystal structure with B_6 clusters in octahedral configuration and the metal atoms forming simple cubic sublattices, as shown in Fig. 2.18. Schell et al. (1982) suggested that the electron conduction occurs through the sublattice of boron, which renders conductivity an isotropic property unlike in metal diborides.

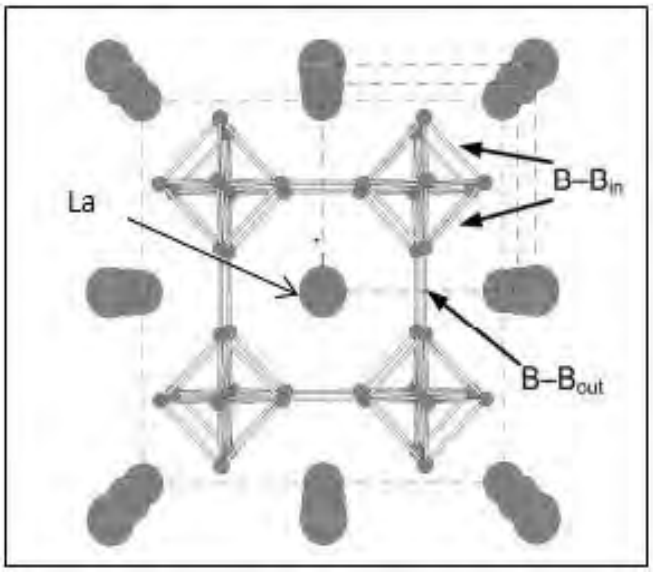

Figure 2.18 Crystal structure of LaB_6 (Mackinnon et al., 2013)

2.4.2 Electrochemical oxidation of metal borides

2.4.2.1 Titanium diboride

Yin et al. (2010) tested the electrochemical stability of TiB_2 in 0.5 M sulphuric acid at 1.20 V for 48 hours, and found titanium diboride to be more electrochemically stable than carbon black XC-72, as the current was not increasing in the redox region. Carbon black showed oxidation at *ca*. 0.6 V, as shown in Fig 2.19. Radmilovic et al. (1995) suggested that formation of surface oxides on carbon are due to hydroquinone-quinone redox coupling.

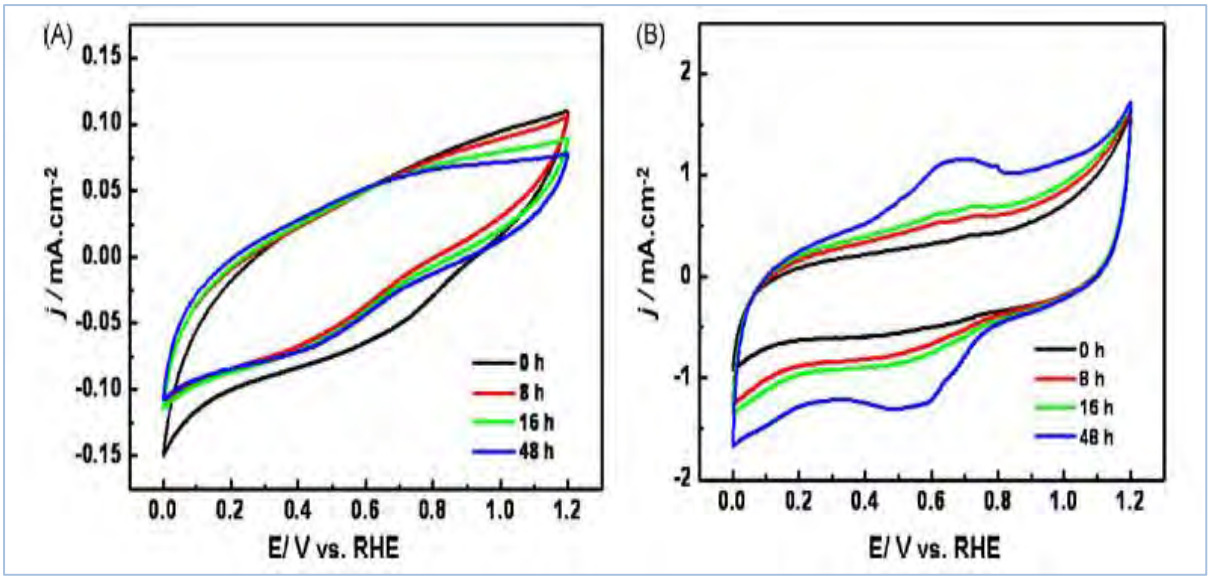

Figure 2.19 CV curves of titanium diboride (A) and carbon black XC-72 (B) held at 1.2 V vs RHE for different durations: 0.5 M H_2SO_4, 20 $mV.s^{-1}$, 25 °C (Yin et al.,2010)

2.4.2.3 Zirconium diboride

Lavrenko et al. (1974) studied the oxidation of ZrB_2, TaB_2, NbB_2 and W_2B_5 by anodic polarisation in Ar saturated 0.5 M H_2SO_4 and found that ZrB_2 was the most stable. The material oxidized to form a protective layer in acidic electrolyte and maintained its passive state up to 1.8 V vs RHE. Compositions of surface compounds formed during oxidation were examined and the protective layer was found to be B_2O_3. It is suggested that zirconium possesses better protective mechanisms, since no metal oxides were formed under oxidation. However, it is claimed that B_2O_3 may reduce electrical conductivity of the material. But if B_2O_3 crystalizes as a perovskite on the surface of ZrB_2 it acts as an electron conductor. Moreover, B_2O_3 may act as a proton conductor as well since it is a solid superacid, with pH 4.

2.4.2.4 Lanthanum hexaboride

The Pourbaix diagram of the La-H_2O system shows that this metal is susceptible to corrosion in acidic medium to form La^{3+} (Garnier et al., 2013). However, as a metal hexaboride, it is not documented in the literature if this material will undergo oxidation or follow a passivation mechanism like other metal borides to form B_2O_3 in acidic electrolyte. As discussed above B_2O_3 forms a protective layer that prevents further oxidation of the material.

2.4.3 Electrocatalytic activity of Pt supported on metal borides

Yin et al. (2010) studied TiB_2 as platinum electrocatalyst support material. TiB_2 powder was prepared via a self-propagating high-temperature synthesis method, and the resulting particle size was 1.8 µm. The colloidal method was used to synthesise 1.5 nm Pt particles from H_2PtCl_6. Pt colloid was added to TiB_2, to result in a loading of 18.6 wt. % on TiB_2. Yin et al. (2010) claims that it is extremely hard to deposit Pt nanoparticles on the surface of TiB_2,

due to its inertness. Therefore, Nafion was added as a stabilizer to enhance metal-polymer-support interaction and Pt dispersion. Moreover, it serves as proton conductor. Roth et al. used the same procedure to deposit Pt to $_{TiB2}$ and the resulted catalyst is shown in Fig 2.20

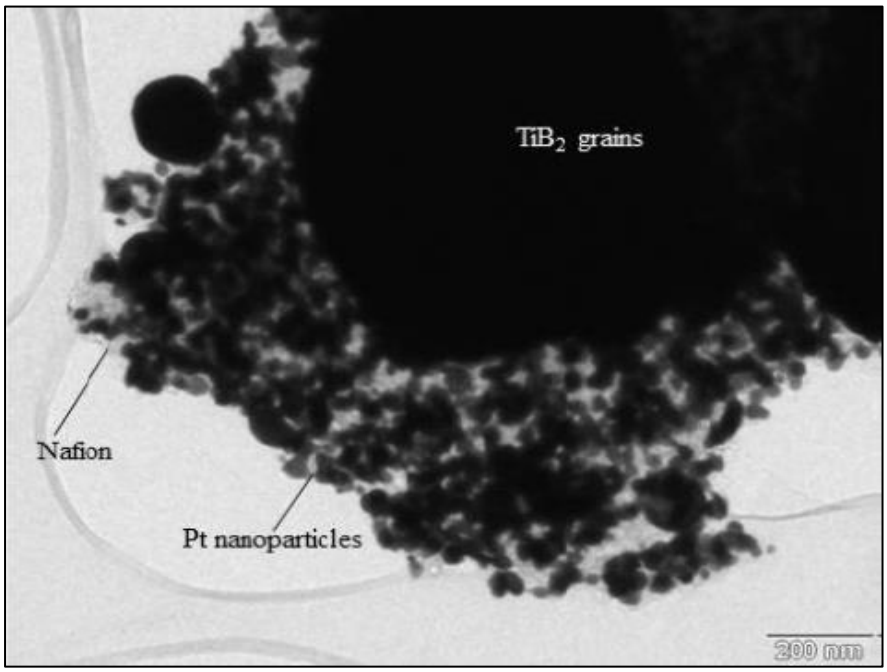

Figure 2.20 TEM micrograph of prepared catalyst (Roth et al., 2014)

As shown in Fig. 2.20, the resulting catalyst has the configuration of metal-polymer-support. However, this raises concerns regarding electron conductivity from active sites to the support, since Nafion is only selective for proton conductivity, not electrons. The electrons that are generated from HOR may not be conducted through to the external circuit and cathode for ORR. However, surprisingly, Yin et al. (2010) and Roth et al. (2014) reported improved activity at 0.8-0.9 V vs RHE, in comparison to Pt/C, as shown in Fig 2.23. This improvement was attributed to electronic effects from the support to Pt. However, Pt weight loading was almost the same as of Pt/C. Therefore, Pt on TiB_2 had higher Pt surface area compared to carbon due to differences on the density of materials. Therefore, Pt/TiB_2 is more likely to outperform Pt/C.

2.4.4 Electrochemical stability of Pt/metal borides

The accelerated durability test (ADT) showed that Pt/TiB_2 is more durable than Pt/C. After 7000 cycles TiB_2 had lost approximately 50% of active surface area and Pt/C had lost approximately 67% after 2000 cycles, as shown in Fig 2.21.

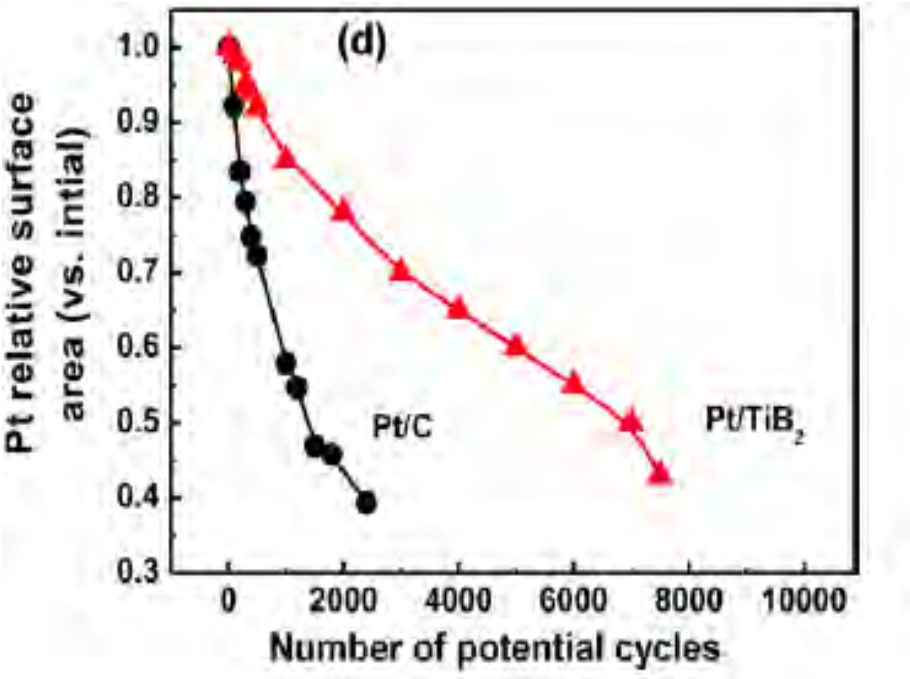

Figure 2.19 Change in ECSA under potential cycling, conditions: Ar saturated 0.5 M H_2SO_4, 25 °C (Yin et al., 2010).

Based on results obtained by Yin et al. (2010) it is evident that TiB_2 has better electrochemical stability compared to carbon and it is reported that this was attributed to the presence of Nafion which stabilises electron deficient TiB_2 with electron rich $–SO_3^-$. Moreover, the presence of Nafion creates steric hindrance and inhibits Pt migration. However, the study by Roth et al. (2014) reports that Pt/TiB_2 undergoes oxidation to form TiO_2 under in situ testing. However, it is not investigated whether it is surface or bulk oxidation and how it affects electrical conductivity of the material and ORR.

Although ZrB_2 has exceptional physical properties, similar to those of TiB_2, no publications were found on its application on PEMFCs.

2.5 The influence of size and morphology of the support on durability

It must be noted that it is not just chemical properties of the material that determines long term stability of the material; this also depends on physical properties such as size, morphology, roughness of the surface and compactness of pores (Artyushkova et al., 2012). It has been reported that major contributing factors to the durability of the PEFC are surface and bulk structural defects in the material. Moreover, the literature suggests that the support durability is inversely proportional to its BET surface area, in those cases where the rate of corrosion is dependent on availability of corrodible surface sites (Stonehart, 1984). Artyushkova et al. (2012) conducted a study on nine different carbon supports with different BET surface area, texture/roughness. It was found that Pt support on carbon materials with high surface area, roughness and compacted pores, were more active towards ORR and more susceptible to corrosion.

2.6 Platinum deposition techniques

There is a wide variety of deposition techniques used to deposit Pt onto support materials, such as chemical precipitation, colloidal, organo-metallic vapour deposition, sol-gel, spray pyrolysis, electrochemical, micro-emulsions and impregnation. However, only two are discussed below, which are relevant to this study:

2.6.1 Wet chemical deposition (impregnation)

Preparation of the catalyst with this method has several advantages, such as simplicity, control of the particle size and low temperature synthesis. The support and Pt-precursor are mixed together in an aqueous solution. The process requires addition of reducing agent; such as formic acid, $NaBH_4$, N_2H_4 and $Na_4S_2O_5$ (Zhang, 2008). The resulted catalyst does not require any heat treatments for activation. This method is quick and efficient and always preferred.

2.6.2. Organo-metallic chemical vapour deposition (OMCVD)

OMCVD is an advanced technique used to deposit thin metallic films on substrates as fine dispersed particles. The process involves evaporation of metal containing precursor (organometallic complex) under controlled pressure and elevated temperature, to ensure sufficient vapour pressure is obtained for deposition. The temperature is further increased so that the complex undergoes thermal decomposition to remove all the organics, followed by formation of metallic nanoparticles on to the substrate (Thurier & Doppelt, 2008). OMCVD is also quick and the product does not have to be washed, filtered and dried like in wet chemical deposition. Therefore, the yield losses are very minimal, whereas in wet chemical deposition some of the product remains on the filter paper during filtration. The OMCVD process is illustrated below in Fig 2.22.

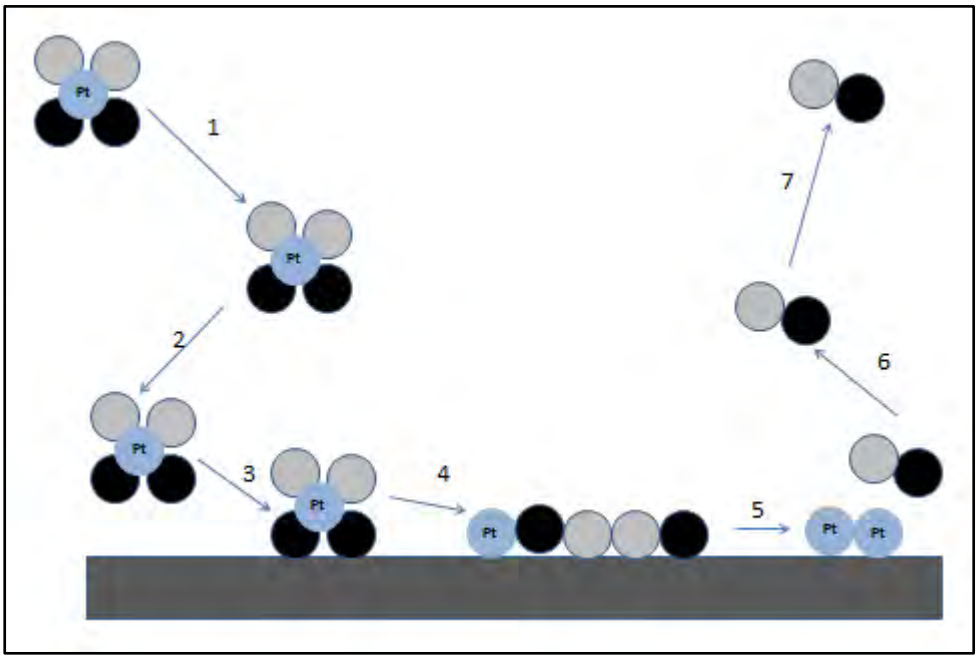

Figure 2.22 Illustration of OMCVD process (adapted from Thurier & Doppelt, 2008).

The stages of OMCVD:

1. Transportation of the precursor into the support/substrate
2. Diffusion of the precursor towards the support/substrate
3. Adsorption
4. Thermal Decomposition of organometallic complex, releasing a metal, followed by nuclei growth to form metallic film.
5. Desorption of by-product species (organics)
6. Diffusion of organics from the support/substrate
7 Evacuation of the system

OMCVD results in highly dispersed metallic particles and with good reproducibility, since it is a gas phase process and allows easy access of vapour to the pores of the support. This process has been successfully used to deposit Pt on carbon for PEFCs, using chlorine free precursor platinum acetylacetonate ($Pt(acac)_2$).This is the precursor of choice due to its stability in atmospheric conditions, low decomposition temperature and high purity films are obtained, after decomposition of ligands (Thurier & Doppelt, 2008).

2.6.3 Techniques used to deposit Pt on inorganic support materials

Polyol method is commonly used to deposit Pt on inorganic supports. The method is based on reduction of a Pt precursor (H_2PtCl_6) by the solvent ethylene glycol. Once the precursor is completely dissolved in ethylene glycol, metal oxides or hydroxides are formed, which are later reduced to Pt metal. The product is then heat treated at 160 °C for over 24 hours in air and in H_2-N_2 at 160 °C for 2 h. (Avasarala et al., 2008; Kakinuma et al., 2012; Yin et al. 2010). H_2PtCl_6 is the Pt precursor of choice for polyol; however, there are problems associated with the use of this precursor. H_2PtCl_6 contains chlorine and Job et al. (2010) and Gelin et al. (2002) suggested that Cl^- species from the precursor may poison Pt and block active sites which results in reduced performance

2.7 Electrochemical characterisation techniques

Electrochemical characterisation techniques play a very crucial role in characterising and evaluating fuel cell's performance and its components, such as the electrocatalyst and its support. Most common characterisation techniques are cyclic voltammetry, linear sweep voltammetry, voltammetric studies using a rotating ring-disk electrode and impedance spectroscopy. The purpose of these techniques is to determine and capture information on the behaviour of the system and track reaction steps taking place, such as mass transfer to and from the electrode, adsorption of reactants, charge transfer either from oxidation or reduction, desorption of products and reversibility of reactions (Qi, 2008).

2.7.1 Cyclic Voltammetry (CV)

This technique has been widely used in fuel cells to study reactions taking place on the catalyst-surface, such as hydrogen adsorption/desorption, capacitance (double layer) charge, Pt oxidation and reduction. Furthermore, a CV profile shows if there are any

chemical changes on the system, such as dissolution of the catalyst and the support or formation of new phases or if reactants/products are dissolved in the electrolyte or bound to the surface of the catalyst. However, CV is mainly used to determine ECSA and durability of PEFCs.

During CV measurements, the voltage is swept linearly between two voltage values (lower and upper limit) at a certain scan rate, and the current response is recorded. The current corresponds to the certain reaction taking place on the system at certain peak potentials. Oxidation occurs on the positive sweep and reduction on the negative sweep. The reversibility of reactions is observed on the CV profile, for e.g. hydrogen adsorption and desorption on Pt from ca. 0.05 - 0.4 V vs RHE, as shown below, in Fig 2.23.

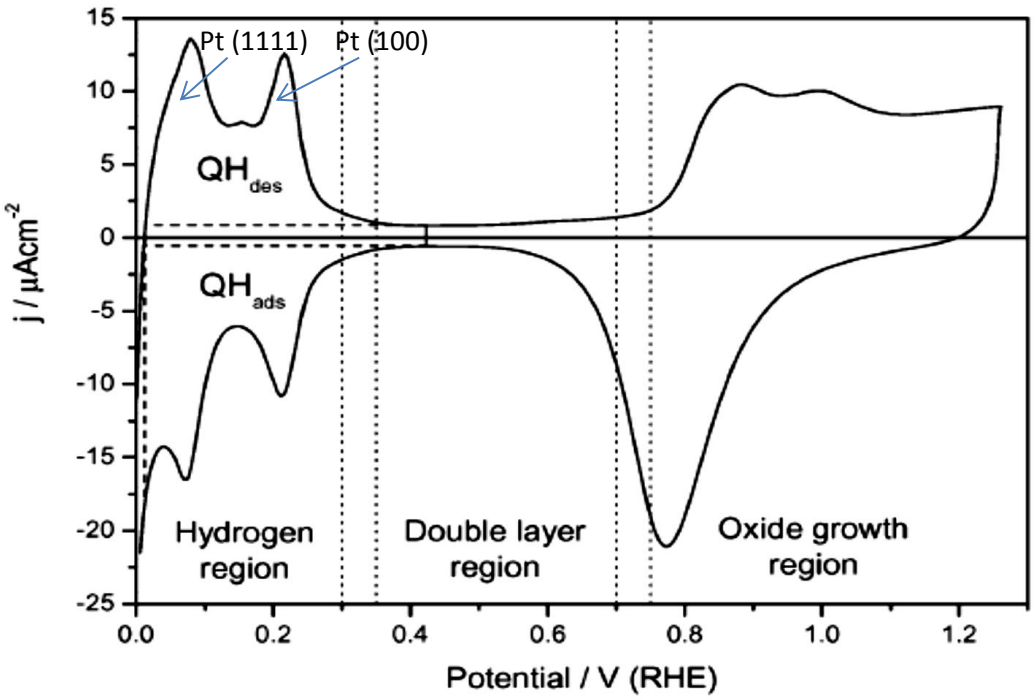

Figure 2.20 Typical CV profile for Pt (Kucernak & Offer, 2008)

When the reaction is reversible, both the oxidation and reduction peak will have the same current density, $j_{p,a}$=$j_{p,c}$, therefore, the charge integrated is the same (Q_a=Q_c). The hydrogen adsorption and desorption peak is integrated to determine the charge of the reaction, of which represents the number of active sites occupied by hydrogen to form the monolayer when divided by the surface area-specific charge and Pt mass as shown below:

$$ECSA = \frac{Q\ \mu C}{210\ \mu C.cm^{-2} * g_{Pt}}$$

The Hydrogen region (0.05 - 0.4 V vs RHE) in Fig. 2.26 shows distinct $H_{ads/des}$ peaks which are related to Pt surfaces. Pt has three dominating crystal surfaces, (111), (100) and (110). Mukerjee (1989) reported that $H_{ads/des}$ peaks at ~0.09 V vs RHE corresponds to weak bonded hydrogen on Pt(111) and strongly bonded hydrogen to Pt (100) crystal facet at ca. 0.27 V vs

RHE. The $H_{ads/des}$ peak corresponding to Pt (110) is only observed on clean Pt surface (Climent & Feliu, 2011).

As no peaks are observed between 0.4 - 0.8 V vs SHE (positive sweep) and 0.6 – 0.4 V vs RHE (negative sweep) there are no reactions taking place on Pt. However, small current is observed in this region, and is attributed to double layer charging. This charge arises from the electrode-electrolyte interface, when a potential is applied the current flows to charge electrode-electrolyte interface. The double layer is usually extrapolated to $H_{ads/des}$ region as shown in Fig 2.23, and used as the baseline for $H_{ads/des}$ area integration to determine the charge for $H_{ads/des}$ which is used to determine ECSA (Zhang, 2008).

As stated in section 1, from 0.85 V vs RHE, Pt undergoes oxidation to form PtO. The oxidation process is illustrated below in Fig 2.24.

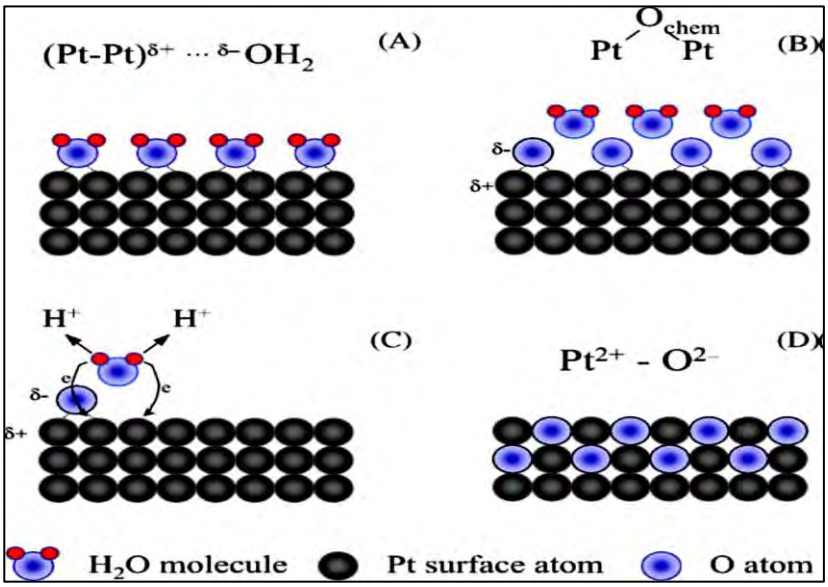

Figure 2.21 Illustration of Pt oxidation in the electrolyte during cyclic loading (Jerkiewicz et al., 2004).

As shown above (A), Pt is partially positively charged and attracts lone pair of oxygen in water, to form $H_2O^{\delta-}$ - $^{\delta+}Pt$ interaction, at 0.27 - 0.85 V vs RHE. There are no features observed on the CV profile for this interaction since there is no charge transfer (Jerkiewicz et al., 2004). At (B), half of the H_2O monolayer is removed and results in formation of half a monolayer (0.5 ML) chemisorbed oxygen and removal of H^+, this occurs at 0.85 – 1.15 V vs RHE and accompanied by charge transfer. Therefore, this feature is observed on the CV profile, as shown in Fig. 2.27. At (C), the second monolayer of H_2O is removed, which is subjected to strong interfacial interactions with Pt that is already 50% covered by oxygen. After removal of H_2O, process B occurs again. But there already exists 0.5 ML oxygen on the Pt surface. Therefore, strong dipole-dipole lateral repulsive interactions occur. Therefore, the system tries to minimise these interactions by interfacial place-exchange between Pt

and adsorbed oxygen, to form PtO lattice, as shown in (D), which is later reduced to Pt^0 at 0.95 - 0.65 V vs RHE (Jerkiewicz et al., 2004).

2.7.1.1 CO Stripping voltammetry

CO stripping is an alternative method used to determine ECSA of the catalyst. However the ECSA is usually larger by a factor of 1.4, compared to ECSA obtained from $H_{ads/des}$. This was attributed to better diffusivity of CO on the catalyst layer compared to H_2 (Rudi et al., 2014). However, Mayrhofer et al. (2008) claims the difference is due to support contributions on $H_{ads/des}$, which leads to underestimation of the ECSA. Below, Fig 2.25 is the typical CO stripping CV profile.

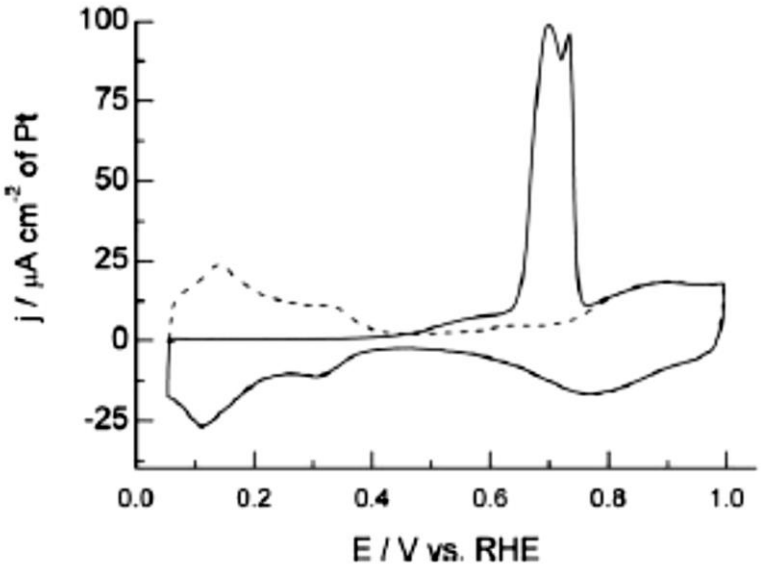

Figure 2.22 CV profile showing CO oxidation in 0.1 M $HClO_4$ at 20 $mV.s^{-1}$ on Pt (Caipina et al., 2010)

For CO stripping technique Pt is poisoned by CO which is subsequently oxidatively removed ('stripped off') at ~0.68-0.78 V vs RHE. The charge that corresponds to the removal of a CO monolayer on Pt surface is transferred in the positive-going sweep resulting in a current response in that region, as shown in Fig 2.25. Integration of the area under CO stripping peak gives the charge which gives the ECSA, as shown in the equation below:

$$ECSA = \frac{Q\ \mu C}{420\ \mu C.cm^{-2} * g_{Pt}}$$

The surface area-specific charge constant for CO is twice of $H_{ads/des}$, since CO stripping is a two electron transfer, whereas for H_2 is just one electron transfer per active site.

2.7.1.2. Accelerated durability test (ADT) using CV

Durability test on a regular working PEFC is very costly, since the lifespan of the PEFC is greater than 5000 h for transportation and 40 000 h for stationary devices (Zhang et al., 2007). Therefore, ADT techniques were developed, such as thermal degradation under hot air conditions *(in situ),* degradation in hot acids, OCV operation and electrochemical degradation under simulated cell conditions. ADT is very efficient and protocols have been developed for experiments either *in situ* or *ex situ* (Shao et al., 2007)

Examples of the most commonly applied tests are shown Fig. 2.26, a) is the catalyst stability test (Pt dissolution), using rectangular wave, cycling from 0.65-0.95 V vs RHE and b) is support stability test, using symmetric triangle wave, cycling from 1 - 1.5 V vs RHE, these methods were proposed by (Zhang et al., 2009; Uchimura & Kocha, 2007; Mitsushima et al., 2007 and Tikahashi & Kocha, 2010).

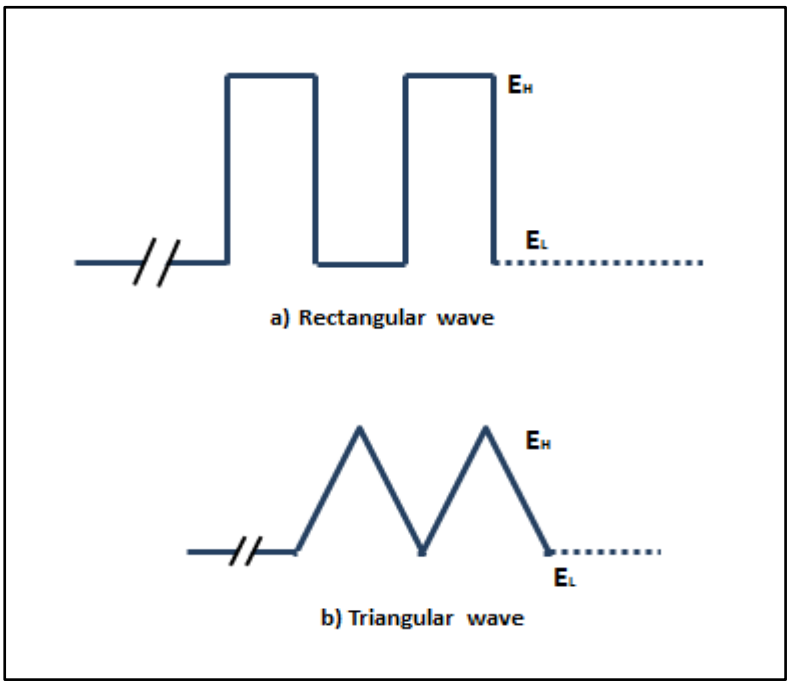

Figure 2.26 Potential cycling profiles in durability studies, E_L and E_H, denoted lower and higher potential (adapter from Charreteur et al., 2008)

The rectangular wave is suggested for a Pt dissolution test, since it is slower than the triangle wave function, and it gives overall corrosion including surface defects and on anchoring sites of Pt. The potentials are selected based on two factors, which are the changes in Pt surface (oxide covered (0.95 V) and oxide free (0.65 v)) and practical consideration of degradation of the catalyst (Takahashi & Kocha, 2010). The triangle wave function shows much faster degradation (no holding time at each potential step) and is applied to test the stability of support materials at high cycling potentials (Park et al., 2012).

During durability testing, CV is used as an electrochemical diagnostic tool, to measure the change in ECSA of the catalyst during cyclic loading, and to investigate any changes on the catalyst layer, such as double layer charging, due to oxidation. Any deviations from the typical Pt CV profile, shows that there is either formation of new phases, dissolution or corrosion taking place on the system, such as carbon oxidation.

In addition, CV will be used to determine stability of pure metal nitrides and borides under cyclic loading, cycling from 0 - 1.5 V vs RHE, to investigate changes over number of cycles during cyclic loading, such as formation of new phases and dissolution of the support.

2.7.2. Rotating disk electrode (RDE)

RDE can be used to study ORR kinetics. The same principles apply as in CV. The voltage is applied and the output is the current, which corresponds to reactions taking place on the system. The reactants in the electrolyte are conveyed to the electrode via diffusion and convection, as shown in Fig 2.27.

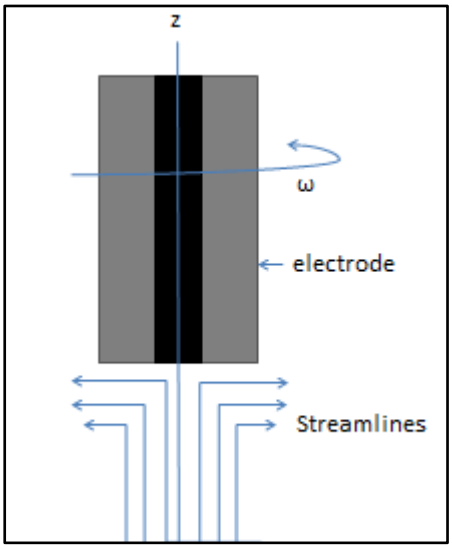

Figure 2.27 Schematic representation of hydrodynamics of a rotating disk electrode, showing streamline of the fluid (adapted from Nikolic et al., 2007)

The rate of mass transfer is increased by increasing the rotation speed (ω) of the electrode, which drags the reactants at the right angle on the electrode due to centrifugal force (Bard & Faulkner, 2001). The reactants diffuses across stagnant layer (Nerst diffusion layer), as shown in Fig. 2.28. Under rotation the thickness of the stagnant layer decreases and the steady state is reached faster and the double layer effect is eliminated, hence, higher currents are measured on the electrode.

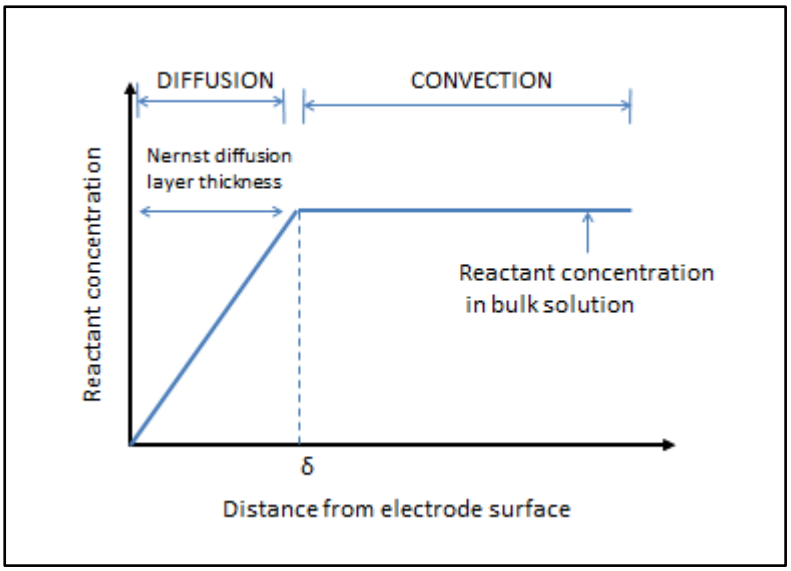

Figure 2.28 Convective-diffusive model (adapted from Nikolic et al., 2007)

The flux of reactants that are transported is proportional to the concentration gradient, according to Fick's law: $N = \frac{D.(C_B - C_S)}{\delta} A$ (Barbir, 2005)

A denotes area of the electrode, C- concentration (B-bulk and s-surface of the catalyst), D diffusion coefficient and δ = 4.98 $D^{1/3} \nu^{1/6} \omega^{-1/2}$, where *ν* is the kinematic viscosity of the solution.

In steady state, the rate of reactants consumption is proportional to the flux,

$$N = \frac{I}{nF}$$

Therefore, $$i = \frac{nF.D.(C_B - C_S)}{\delta}$$

This relationship shows that the current density depends on the concentration of reactants. When the rate of consumption of reactants exceeds the rate of diffusion, the limiting current is reached, since the surface concentration is zero. Therefore,

$$i_L = \frac{nF.D.(C_B - 0)}{\delta}$$

On RDE studies, the limiting current is measured at various rotation speeds and used to calculate the kinetic current using the Koutecky-Levich equation:

$\frac{1}{i} = \frac{1}{i_k} + \frac{1}{i_L}$ (Barbir, 2005)

The plot of log i_k vs overpotential gives the so called Tafel slope, which gives information on whether ORR proceeds via a two or four electron pathway. The Tafel slope of polycrystalline Pt in 0.1 M $HClO_4$ is measured to be ca.-60 mV/dec at low current density, and -120 mV.dec

at higher current density. At lower potentials, below 0.3 V vs RHE, hydrogen ions are adsorbed and produce intermediates such as H_2O_2, according to the two electron process and reduces the ORR current at lower potentials (Yeng et al, 2013). To study formation of peroxides on the system, rotating ring disk electrode (RRDE) technique is commonly used.

2.7.3 Rotating ring disk electrode (RRDE)

RRDE consists of the ring and the disk, the ring is held at a fixed potential, while the voltage is swept at the disk. This allows ORR to occur on the disk via four electron pathway to form water and the intermediates formed are reduced on the ring as shown in Fig.2.29.

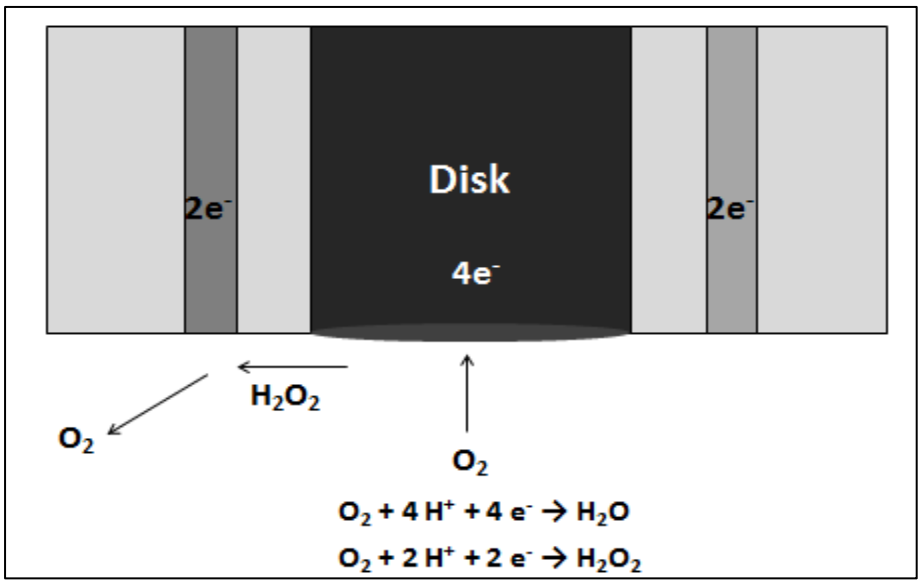

Figure 2.29 Illustration of ORR mechanisms on RRDE

However, not all peroxides are detected and reduced on the ring, only the small percentage is. Therefore, the collection efficiency of the ring has to be measured before commencing RRDE studies. Paulus et al, (2001) used $K_3Fe(CN)_6$ compound to measure collection efficiency. The oxidation of the product $[Fe(CN)_6]^{4-}$ (from the disk) to $[Fe(CN)_6]^{3-}$ occurs on the ring, as shown in Fig. 2.30. The efficiency is given by the disk and ring current ratio: $N = -\frac{I_R}{I_D}$.

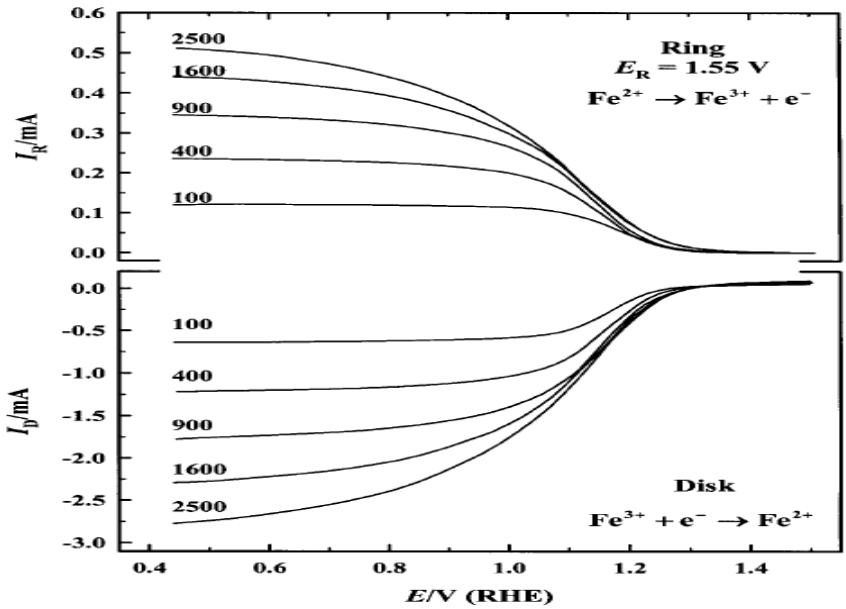

Figure 2.30 Collection efficiency curves at 60 °C, while the ring was held at 1.55 V in 0.1 M NaOH with 10 mM $K_3Fe(CN)_6$, at various rotation speeds, scanning at 20 $mV.s^{-1}$ (Paulus et al, 2001)

Paulus et al, (2001) reported that the collection efficiency is independent of the rotation speed, as the measured collection efficiency was the same across all rotation speeds.

Chapter 3

3. Research plan

Poor durability of PEFCs is one of the major hindrances to commercialisation. As shown in the introduction and literature review, carbon based support materials are significant contributors to reducing durability. This has opened the search for more robust support materials, which can withstand harsh conditions in the fuel cell and promote ORR.

3.1 Objective

The main objectives of this research project is to evaluate a range of metal nitrides and borides for their suitability as a support for electrocatalysts (e.g Pt) in order to improve durability, efficiency and performance of PEFCs.

The approach to achieving this objective is to carry out and analyse the results of the following:

- Determine physical properties such as specific surface area, porosity and crystal structure of metal nitrides and borides.
- Support Pt on metal nitrides and borides via a wet chemical deposition method as well as OMVCD, using chlorine-free precursors, to avoid potential poisoning by chlorine (Gelin et al. 2002; Job et al., (2010).
- Measure electrocatalyst surface area (ECSA) and determine intrinsic and mass activity of Pt supported on metal nitrides and borides.
- Perform accelerated durability tests (ADT) to determine electrochemical stability.

3.2 Hypotheses

Based on the objectives of this research project and literature review, the following hypotheses were developed:

- Metal nitrides and borides can be used as alternative electrocatalyst support materials since they are more electrochemically stable than carbon.
    - ❖ When metal nitrides are exposed to oxidizing environment, a very thin passive layer consisting of metal oxides and oxynitrides is formed, which prevents further oxidation of the bulk material (passivation).
    - ❖ Metal borides are passivated via formation of surface oxides, such as $TiBO_3$, $ZrBO_3$ and B_2O_3 when exposed to oxidising environment.
- Surface oxides formed on metal nitrides and borides do not compromise electron conductivity, hence, do not affect the activity of the catalyst.

- As supports, metal nitrides and borides may enhance the activity of Pt, due to strong support-metal interaction. In addition, they may also supress Pt migration, dissolution and formation of peroxides.

3.3 Research questions

Based on the objectives the following key questions were developed:

- Are the metal nitrides and borides used in this study more electrochemically stable than carbon?
- Are the methods used to deposit Pt on carbon applicable to metal nitrides and borides as supports, using chlorine free Pt-precursors?
- Can the electrochemical surface area (ECSA) and activity be measured the same way as Pt/C?
- Do Pt-electrocatalysts supported on metal nitrides and borides outperform Pt/C and are they more durable?

3.4 Limitations and scope of research

Not all transition metal nitrides and borides will be studied due to time constraints. Only a few will be selected, based on chemical stability, availability and other essential properties beneficial to PEFCs, such as porosity, thermal and electron conductivity.

Metal-support electronic interaction and surface chemistry will not be studied in this research project due to both time and lack of availability of XPS at the University of Cape Town.

The cost associated with the use of metal nitrides and borides as alternatives to carbon will not be evaluated in this study.

Lastly, due to time constrains, commercial powders (inorganic supports) will be used to carry out this study.

4. Experimental Approach

The experimental programme developed to investigate the key questions is outlined below.

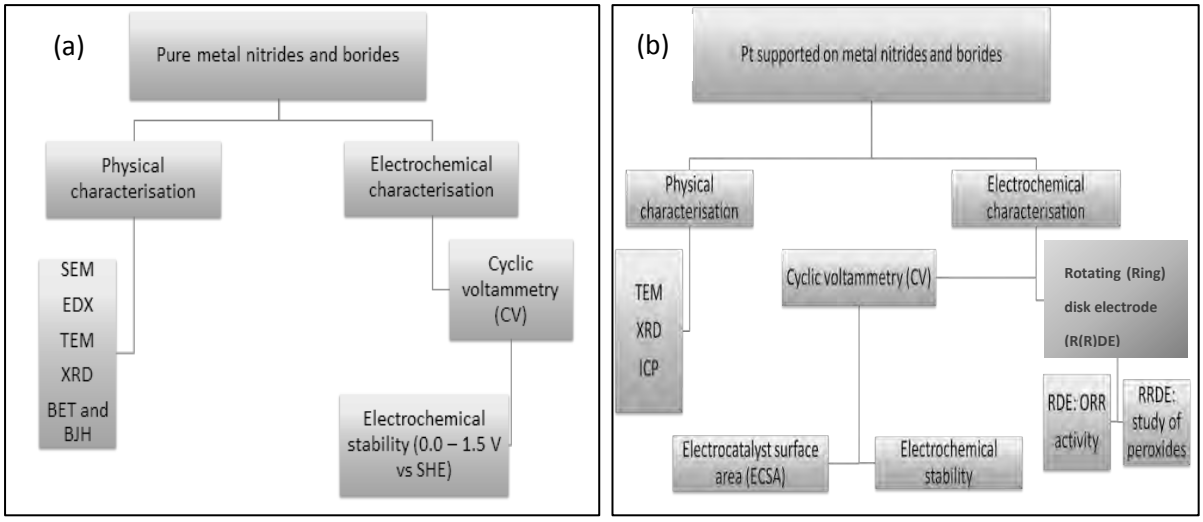

Figure 4.1 Schematic diagram of the experimental plan before (a) and after (b) Pt deposition on metal nitrides and borides**.**

4.1 Chemicals

Materials	**Supplier**	**Product Information**
TiN	US Research Nanomaterials	>99.2 %, 20 nm
TiB_2	US Research Nanomaterials	>95.0 %, 58 nm
ZrB_2	US Research Nanomaterials	>99.0 %, 43 nm
ZrN	Sigma Aldrich	≥ 99 %, 1-2 µm
LaB_6	American Elements	99+%, < 100 nm
Carbon (Vulcan)	ElectroChem, Inc.	EC-XC72-100
20 wt % Pt/C	Alfa Aesar	HiSPEC^{TM} 3000
40 wt % Pt/C	Alfa Aesar	HiSPEC^{TM} 4000
60 wt % Pt/C	HySA/Catalysis	HySA-V60
$Pt(acac)_2$	Sigma Aldrich	97%
$H_2Pt(OH)_6$	Sigma Aldrich	-
$HClO_{4(aq)}$	Sigma Aldrich	70%
Nafion solution	Ion-Power, Inc	5 wt % in water and alcohols
$(CH_3)_2CHOH$	Kimix Chemicals	-
C_2H_5OH	Kimix Chemicals	99.9%, Absolute
$K_3Fe(CN)_6$	Sigma Alderich	99%
Ar	Afrox	99.999%
O_2	Afrox	99.998% (4.8)
CO	Afrox	99.97%

4.2 Physical characterisation techniques

4.2.1 Transmission Electron Microscopy (TEM)

Tecnai G^2 electron microscope was used for imaging of metal nitrides and borides before and after Pt deposition to determine Pt particle size and distribution. A small sample was suspended in acetone in the small centrifuge tube and the tube containing the solution was submerged in an ultrasonic bath for 15 min. 5 µl of the suspension was micropipetted onto a carbon coated copper grid and dried in air. Once acetone had evaporated the grid was transferred to TEM for analysis. The sample was irradiated with an electron beam at 200 kV for better transmission and resolution (Reimer, 2008). The electrons from the beam are transmitted through the sample, and scattered by the electrostatic potential of the material. The scattered wave of electrons passes through the electromagnetic objective lens to form the image. The particle size was measured from images and statistically analysed using ImageJ software.

4.2.2 Scanning Electron Microscopy (SEM)/Energy Dispersive X-ray Spectrometry (EDX/S)

SEM was used to study the morphology of metal nitrides and borides. Less than 1 mg of the sample was placed on the sample stub that was coated with carbon paste, for adhesion and electron conductivity. Any excess sample on the stub was removed by compressed air spray. The sample was then transferred to the Nova NanoSEM chamber and irradiated with the electron beam across the area of inspection, under vacuum conditions. When the beam interacts with the sample, secondary electrons are released like in TEM, and these secondary electrons are detected to reproduce topographical information.

EDS was used to determine the elemental composition of materials as received, and to detect the presence of any impurities. When the incident beam collides with electrons from the sample, electrons move and occupy the outer shell. The change of electron distribution in orbitals reduces the energy, and causes the sample to release photons corresponding to the change in energy. Photons are detected and are characteristic of different elements and, although the technique has limitations with sensitivity to lighter elements, the spectra obtained can assist with the determination of relative atomic percentages.

4.2.3 X-ray diffraction (XRD)

A D8 Advance Brucker was used to determine the crystal structure, Pt crystallite size and lattice constants. Co K_α was used as the X-ray source and the scan rate was set to 3.5 2θ/min, scanning from 20-100 2θ. The incident wave is diffracted by the crystal plane of the sample at different directions according to Bragg's law. The angle of diffraction is recorded by photographic film.

Produced patterns from the XRD were matched with XRD patterns from the ICCD database, to look for corresponding peaks. To determine the Pt particle size, the Pt(111) peak and Debye-Scherrer equation below, was used.

$$\tau = \frac{K\lambda}{\beta cos\theta} \quad (4.1)$$

Where, τ= dimension of the particle perpendicular to the reflecting plane.

K= shape factor

λ= X-ray wavelength

β=peak broadening

θ= angle of diffracted wave

To calculate lattice constant, the d-spacing between planes was measured using Bragg's equation:

$n\lambda = 2dsin\theta$, the value calculated is substituted in the equation below, to determine 'a' which is the lattice constant.

For cubic structure (e.g metal nitrides and LaB_6): $\frac{1}{d^2} = \frac{h^2+k^2+l^2}{a^2}$ (4.2)

For hexagonal structure (e.g metal diborides): $\frac{1}{d^2} = \frac{4}{3}\frac{h^2+hk+k^2+l^2}{a^2} + \frac{l^2}{c^2}$ (4.3)

4.2.4 Brunauer-Emmett-Teller (BET) and Barret-Joyner-Halenda (BJH) measurements

Nitrogen (N_2)-adsorption isotherms were recorded to determine the BET-specific surface area of support materials. BET measurements were carried out at different relative pressures to determine the volume of N_2 adsorbed to form a monolayer. BJH was used to determine porosity of the material, using hysteresis in physisorption isotherms of nitrogen at relative pressures, upon filling and emptying pores at 77.35 K. The adsorption branch was used to measure the pore size.

4.2.5 Inductively Coupled Plasma-Atomic Emission Spectroscopy (ICP-AES)

A Varian ICP 730-ES Spectrophotometer was used to determine Pt loading on support materials. A MARS-5 microwave was used to digest samples in concentrated 3:1:1 hydrochloric acid (HCl), hydrofluoric acid (HF) and nitric acid (HNO_3) at 180 °C for 20 minutes. After digestion, the sample was exposed to inductively coupled plasma to produce electromagnetic radiation. The intensity at a given wavelength is proportional to the concentration of the atoms in the analyte.

Moreover, ICP-AES was used as a diagnostic tool for durability test. After testing, electrolyte solutions were analysed to determine the concentration of materials that leached into solution.

4.2.6 Thermogravimetric analysis (TGA)

A Mettler TGA/sDTA851e Thermogravimetric Analyser was used as an alternative method to determine metal loading on carbon, due to the fact that irreproducible results were

obtained with the ICP-AES technique. Ceramic crucibles were used as sample holders during analysis. A very small amount of the sample was placed in the crucible with lid and an empty crucible with lid was used as the blank (to correct for background). The temperature profile was set from 25 to 800 °C, at the heating rate of 10 °C.min^{-1}. The catalyst was combusted in air flowing at 10 mL.min^{-1}. The initial mass of the catalyst was measured before carbon was combusted and the final mass after combustion represents the mass of Pt.

4.3 Pt deposition techniques

Since all the support materials have different densities, Pt loading was calculated in terms of v/v % (v/v refers to volume Pt per volume support) to ensure that every support has the same amount of Pt per unit surface area. The density and mass of support materials and Pt was used to determine the volume (volume= mass/density). The v/v % of 20 wt % Pt/C, which is used as the benchmark, is 1.68 % after correcting for the differences in supports (carbon and inorganic materials) surface area. Therefore, to obtain 1.68 v/v% Pt on metal nitrides and borides, the following wt% loadings were to be deposited:

Table 4.1 Densities and calculated v/v% and wt%, equivalent to 20 wt% Pt/C

Support materials	Density (g.cm^{-3})	1.68 v/v% Pt wt%	3.36 v/v% Pt wt%	5.04 v/v% Pt wt%
Carbon	1.80	20.0	40.0	60.0
TiN	5.40	6.66	13.3	20.0
TiB_2	4.52	7.96	15.9	23.8
LaB_6	4.72	7.62	15.2	22.9
ZrN	7.09	5.08	10.2	15.2
ZrB_2	6.08	5.92	11.8	17.8

Two deposition techniques were used to deposit 1.68 v/v% Pt on metal nitrides and borides. Products were compared, in terms of Pt particle size and distribution. The technique that produced better results was further used to deposit v/v% Pt loading equivalent to 40 wt% and 60 wt% Pt/C. The v/v% was calculated and found to be 3.36 and 5.04, respectively.

4.3.1 Wet chemical deposition (impregnation)

A ligand mixture was added to $H_2Pt(OH)_6$ and stirred, until Pt precursor was dissolved. The solution was transferred to round flask containing 500 mg support material suspended in 10 ml H_2O. The pH was adjusted to 8.4 whilst the temperature was kept at 25°C. The mixture was then heated up to 80 °C in an oil bath, while N_2 gas was constantly flowed. After that a reducing agent was added drop-wise. The mixture was stirred for 1.5 hours at 80°C. Synthesized catalysts were allowed to cool to room temperature, then filtered, washed with deionised H_2O and dried under ambient conditions.

4.3.2 Organo-metallic chemical vapour deposition (OMCVD)

500 mg of the support material was mixed with $Pt(acac)_2$ (the amount is shown in table 4.2) and transferred to the reactor vessel. The vessel was then placed in the furnace (Labofurn). The temperature was ramped to 100°C at 3.5 °C/min and held for 30 min, while Ar was constantly flowing through the reactor. The reactor was held at this temperature to allow evaporation of water and trace organics. The gas flow was stopped by closing the outlet first, then the inlet to maintain inert atmosphere in the reactor. The temperature was then ramped to 350 °C at 2.5 °C/min and held at that temperature for 1.5 h, to allow precipitation and nuclei growth of Pt on support surfaces. The reactor was then removed from the furnace and allowed to cool to room temperature.

Table 4.2 Mass of $Pt(acac)_2$ added to yield 1.68 v/v% Pt on metal nitrides and borides.

	TiN	**TiB_2**	**LaB_6**	**ZrN**	**ZrB_2**
$Pt(acac)_2$ (mg)	65.12	77.83	74.50	49.67	57.88

4.4 Electrochemical characterisation techniques

CV and R(R)DE techniques were used to determine electrochemical stability, ECSA, durability and ORR kinetics of synthesised catalysts. CV and R(R)DE measurements were carried out in 0.1 M $HClO_4$ at room temperature in a 250 ml three-electrode cell (Gamry instruments), shown below in Fig. 4.2. The cell was cleaned with oxidative Piranah solution (1:3 Hydrogen peroxide:sulphuric acid). The cell was soaked overnight in the solution and rinsed with 18.2 MΩ.cm deionised water. A SP-300 Bipotentiostat (Biologic Science Instruments) and RDE 710 Gamry rotating electrode were used.

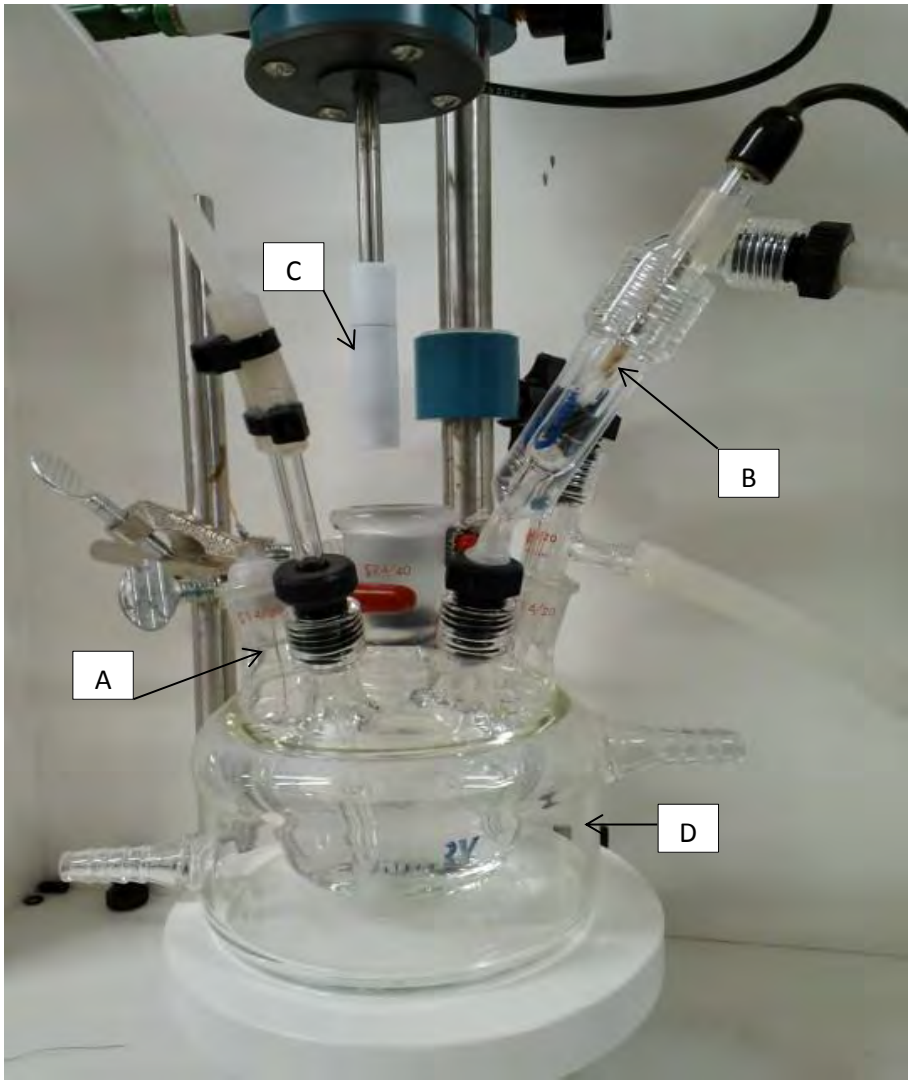

Figure 4.2 Electrochemical experimental setup

The elements of the typical setup are shown in Fig 4.2. A is the Pt wire, which was used as the counter electrode. However, for durability tests Pt wire was replaced by a graphite counter electrode, since Pt-wire undergoes Pt dissolution and it was directly inserted into the electrolyte. Hence, the amount of Pt dissolved from the counter electrode will increase Pt concentration measured, as it was observed in the durability study by Urchaga &Rice (2013), B is the reference electrode $Hg/HgSO_4$ saturated in K_2SO_4. For CV and RDE, glassy carbon disk electrode, C (5 mm, Pine instruments) was used, and to measure peroxides a rotating ring (Pt) disk (glassy carbon) electrode (E6 series, AFE6RIRT, Pine instruments) was used. The collection efficiency was determined experimentally as described below (4.4.5.1)

4.4.1 Cleaning of electrodes

The electrodes were manually polished in the figure of 8, until they had a mirror-finish, before ink deposition. Buehler micro-polish Alumina 1.0 µm and 0.05 µm powder were mixed with 18.2 MΩ.cm deionised water to make the paste on Buehler micro-cloth for polishing. After polishing, the electrodes were rinsed by 18.2 MΩ.cm deionised water and

placed in the beaker with water and ultrasonicated for 15 min to remove debris.The alectrodes were dried under rotation at 700 rpm.

4.4.2 Catalyst ink preparation for CV and RDE studies

The formulation used to prepare ink for Pt/C, consists of: 10 mg catalyst, 5 ml H_2O, 1.5 ml isopropanol, 25 µl Nafion. All components were mixed in the vial and placed in a beaker with ice. The vial containing the suspension was then immersed in an ultrasonic bath for 30-45 minutes. For metal nitrides and borides ink optimisation was performed. The optimum ECSA in the range tested was achieved using the formulation shown in Table 4.3.

CV technique was used to measure ECSA. Different solvents and combinations such as varying Nafion content, ratios of solvent:water and catalyst to solvent were investigated.

Table 4.3 Ink formulation for metal nitrides and borides (please note that for ZrN and ZrB_2 the ink was not optimised since Pt deposition was not successful, see chapter 5)

	Pt/TiN	**Pt/TiB_2**	**Pt/LaB_6**
Catalyst (mg)	10.0	10.0	20.0
Ethanol (ml)	3.00	2.00	2.50
Nafion (µl)	8.50	8.00	10.0

10 µl of prepared catalyst ink was micropipetted onto a polished glassy carbon disk electrode. The electrode was then dried in air at room temperature for ca. 15 min, to allow the solvent to evaporate. For Pt/C, the electrodes were dried in air under a rotation speed of 700 rpm for 45 minutes.

4.4.3 Cyclic voltammetry (CV)

4.4.3.1 Electrochemical stability of metal nitride and borides

To measure the electrochemical stability of pure metal nitrides and borides (before Pt deposition), CV measurements were carried out in Ar saturated 0.1 M $HClO_4$, cycling 3000 times between 0 and 1.5 V vs SHE at 100 $mV.s^{-1}$ at room temperature. The sample loading on the disk was set to 15.32 µg. After tests, electrolyte solutions were analysed by ICP, to determine the amount of leached material during load cycling. TiN and ZrN samples from the electrodes after testing were analysed by XRD to determine if oxnitrides or oxides were formed. Vegard's law was used to calculate the lattice constants, as it was done by Avasarala et al. (2010) on TiN.

4.4.3.2 ECSA measurements

(i) Using H-adsorption peak.

The electrolyte was purged with Ar 30 minutes before commencing measurements. Once the ink on electrodes was dry, electrodes were pre-wetted with 0.1 M $HClO_4$ (to prevent

formation of air bubbles on the catalyst surface) before being inserted into the electrolyte solutions. Before inserting the electrode the potential was set to 0.5 V vs SHE. The electrode was then cleaned/pre-conditioned by cycling 50 times between 0 - 1.1 V vs SHE at 100 $mV.s^{-1}$ to remove impurities. Thereafter, the scan rate was reduced to 20 $mV.s^{-1}$ and 5 cycles were recorded. The last cycle (5^{th}) was used to determine the ECSA by integrating the charge under the hydrogen adsorption peak and normalised by 210 $\mu C.cm^{-2}$ x Pt mass loading.

(ii) CO stripping

Before starting CO stripping measurements, pure metal nitrides and borides (without Pt) were electrochemically tested for activity towards CO oxidation. The electrodes were pre-conditioned and cleaned in the electrolyte by cycling 50 times, as described above. Thereafter, the electrolyte was purged with CO for 20 min, while the electrode was held at 0.1 V vs SHE to allow CO to bind to active sites (Maillard et al., 2005). After 20 min the electrolyte was purged with Ar for 30 min. A total of 5 cycles were recorded scanning from 0 - 1.1 V vs SHE. The 5th cycle was used as the baseline to integrate the charge under CO peak.

(iii) CO baseline correction method (Binninger et al. (2014))

CV measurements were carried out in Ar saturated electrolyte at the same scan range and rate as in (i) and (ii). The electrode was cleaned over 50 cycles and 5 cycles were recorded at 20 $mV.s^{-1}$. Thereafter the electrolyte was saturated with CO and 5 CV scans were recorded, while rotating the electrode at 1600 rpm. The CV scan from CO saturated electrolyte was subtracted from CV in Ar, to remove support contributions from the hydrogen adsorption (H_{ads}) peak. The difference was integrated to determine the charge for H_{ads}.

4.4.4 Rotating disk electrode (RDE)

To obtain the kinetic current density for ORR, RDE measurements were carried out after CV measurements using the same electrode. However, before starting LSV, the background (capacitive) current was measured under Ar using ORR sweep profile, scanning from 1.2 – 0.1 V vs SHE and 0.1 -1.2 V vs SHE at 5 $mV.s^{-1}$ at various rotation speeds. Rotation speeds were set to 400, 900, 1600 and 2500 rpm. The background current was subtracted from the experimental ORR current. Thereafter, the electrolyte was saturated with O_2 and RDE measurements were carried out. The kinetic current (I_k) was determined using Koutecky-Levich equation, at 0.7, 0.8 and 0.9 V vs SHE. The mass and intrinsic activity is represented by I_k/mass of Pt on the disk and I_k/intrinsic surface area.

4.4.5 Rotating ring disk electrode (RRDE)

RRDE measurements were done to determine the amount of peroxides formed by Pt supported on metal nitrides and borides. The same electrochemical cell setup was used, with a different shaft and the electrode shown below, (Fig. 4.3).

Figure 4.3 RRDE electrode

Before RRDE studies, the collection efficiency of the ring was measured, as follows.

4.4.5.1 Collection efficiency

The collection efficiency of the ring was measured using a procedure by Paulus et al, (2001), using 10 mmol $K_3Fe(CN)_6$ compound in the electrolyte. However, for this study measurements were carried out at room temperature and the ring was held at 1.2 V vs SHE. The disk was swept from 1.2 – 0.1 V vs SHE and reversed, at the scan rate of 5 $mV.s^{-1}$ at 400, 900, 1600 and 2500 rpm. The electrolyte was saturated with Ar. The collection efficiency is given by the disk and ring current ratio:

$$N = -\frac{i_{ring}}{i_{disk}}.$$

4.4.5.2. RRDE measurements for hydrogen peroxide (H_2O_2) formation

The collection efficiency will never be close to 1, since not all peroxides that are formed on the disk are dictated/goes to the ring (Paulus et al., 2001); therefore it is always crucial to measure the collection efficiency before commencing RRDE studies.

These measurements were carried out in 0.1 $HClO_4$ purged with oxygen and the conditions were similar to those of the collection efficiency and RDE measurements. To determine if reduction of O_2 proceeded via $2e^-$ or $4e^-$ pathway equation (4.7) was used, which is derived from calculating the current measured on the disk and the ring (Antoine and Durand, 2000).

$$i_{2e^-} = \frac{i_{ring}}{N} \qquad (4.4)$$

$$i_{Disk} = i_{2e^-} + i_{4e^-} \qquad (4.5)$$

And $$\frac{i_{Disk}}{n} = \frac{i_{2e^-}}{2} + \frac{i_{4e^-}}{4} \qquad (4.6)$$

Therefore,

$$n = \frac{4\, i_{Disk}}{i_{disk} + \frac{i_{ring}}{N}} \qquad (4.7)$$

In addition, the amount of H_2O_2 formed per O_2 molecule was calculated using the following equation:

$$X_{H_2O_2} = \frac{\frac{2\, i_{Disk}}{N}}{i_{disk} + \frac{i_{ring}}{N}} \qquad (4.8)$$

4.4.6 Durability studies

4.4.6.2 Pt dissolution

Electrodes and catalysts were prepared as explained above in section 4.3.1/2. The ECSA was measured (as described in section 4.3.3) before starting durability test to obtain initial ECSA. The rectangular wave profile from 0.65-0.95 V vs SHE was used to determine ECSA losses due to Pt dissolution (Zhang et al., 2009). The scan rate was set to 100 mV.s^{-1}. The potential was held at each potential step for 1 s as shown in Fig. 4.4 below.

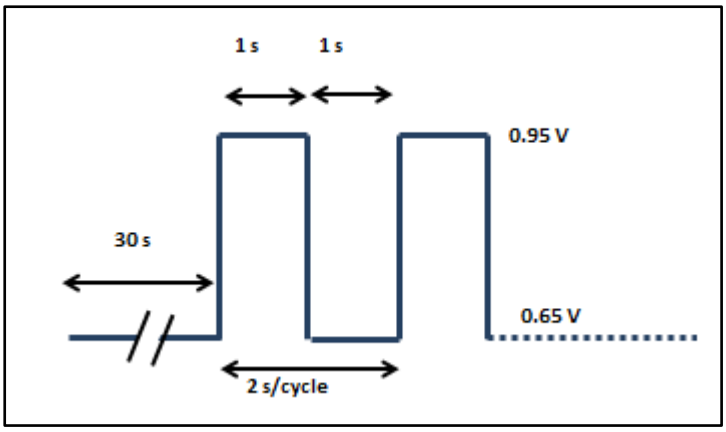

Figure 4.4 Rectangular wave function from 0.65-0.95 V vs SHE for Pt dissolution test

The ECSA was measured at 0 and after 100, 500, 1000, 4000, 7000 and 10 000 cycles. Before measuring the ECSA after cycling, the electrode was cleaned by cycling 50 times between 0.01-1.11 V vs SHE, to remove by-products and oxides formed on the catalyst film during degradation test. The same procedure was used to measure ECSA during the catalyst support degradation test shown in figure 4.5.

4.2.6.2 Support corrosion

Support corrosion studies of the materials with Pt deposited were conducted in a similar manner as described above. However, with different scan limits (1.0 – 1. 5 V vs SHE) and in a triangle wave pattern (Kocha & Takahashi, 2010) as shown below, (Fig. 4.5).

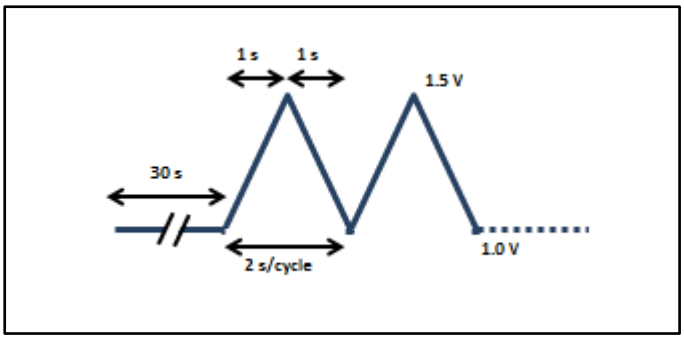

Figure 4.5 Triangle wave function, cycling from 1.0 - 1.5 V vs SHE for support corrosion test.

Chapter 5

5. Results and Discussion

Based on objectives, hypothesis and experimental procedure, the following results were obtained. It must be noted that since the focus of this study is on Pt deposition and the behaviour of the materials as supports, all metal nitrides and borides used are commercially available powders. Pt/C catalysts are used as benchmark and were commercially obtained as well. All the experiments were repeated at least twice to check for reproducibility of results.

5.1 Physical characterisation

Metal nitrides and borides were physically characterised using TEM, SEM/EDX, XRD, BET and BJH to determine the particle size, crystal structure, specific surface area, and pore structure of support materials, as received.

5.1.1 TEM, SEM/EDS and XRD of metal nitrides and borides.

(i) TiN

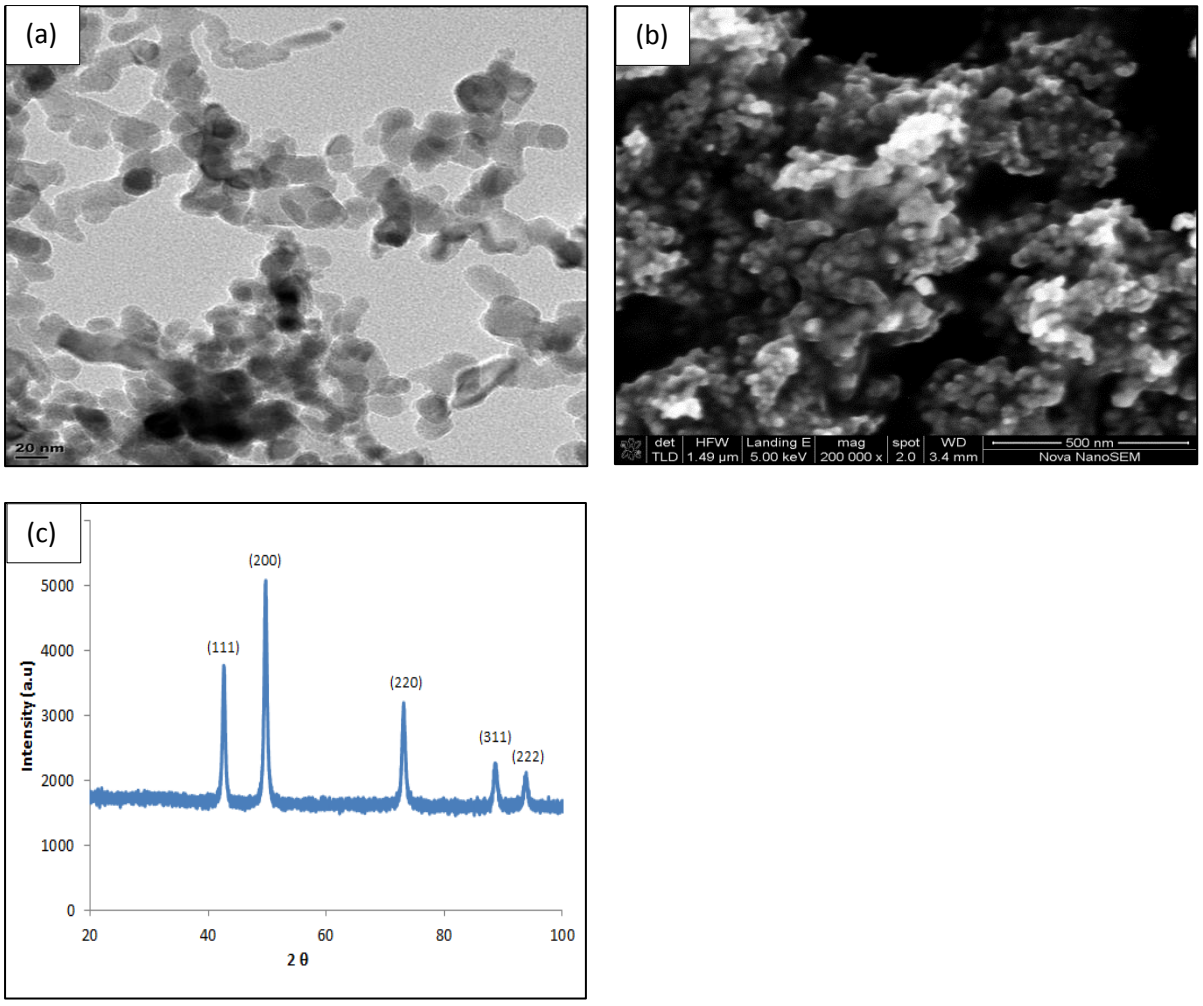

Figure 5.1 TiN (a) TEM image, (b) SEM image and (c) XRD pattern of TiN scanning from 20-100 2θ

Commercial TiN nanoparticles are reported to have an average particle size of 20 nm by the supplier (US Research Nanomaterials, Inc.). The mean particle size measured from the TEM image (Fig 5.1 (a)) is 18.9 ± 5.9 nm. The XRD pattern of TiN is similar to the one reported in literature (Avasarala et al., 2010). In addition, XRD was used to measure the particle size, and is found to be 18.6 nm, using the TiN (200) peak and Debye-Scherrer equation. EDS analysis showed the presence of 12.21 wt% oxygen on the material. The presence of oxygen on the material is attributed to TiN oxidation at room temperature, via the following reaction:

$2TiN + 2O_2 \rightarrow 2TiO_2 + N_2 \qquad \Delta G° = -611.8\ kJ.mol^{-1}$

The literature reports that oxidation of TiN occurs via three stages (Esaka et al., 1997; Komratov et al., 1997):

I. Diffusion of O_2 into the crystal lattice of TiN and substitute N at interstitial sites, and as a result titanium oxynitride is formed.

II. Ti_nO_{2n-1} phases are formed and prevents further oxidation of the material, under diffusion control.

III. Slow oxidation of TiN to TiO_2

Since EDS showed the presence of both nitrogen and oxygen, it was investigated whether oxidation was at stage I.,II. or III., using XRD TiN(111) peak and Vegard's law to calculate the lattice constant *'a'*. The calculated *'a'* is 4.26 Å, and does not correspond to the lattice constant's of TiN (4.24 Å), TiO_2 (4.59 Å) and TiO (4.18Å) (Bauer, 1982; Burdett et al.,1987; Avasarala et al., 2010), but rather lies inbetween of TiN and TiO_2. This suggests that TiN is partially oxidised on the surface to form oxynitride species, as shown in the study by Avasarala et al., 2010. Moreover, if the material was at stage lll., titanium oxide peaks would have been observed on the XRD pattern.

(ii) TiB_2

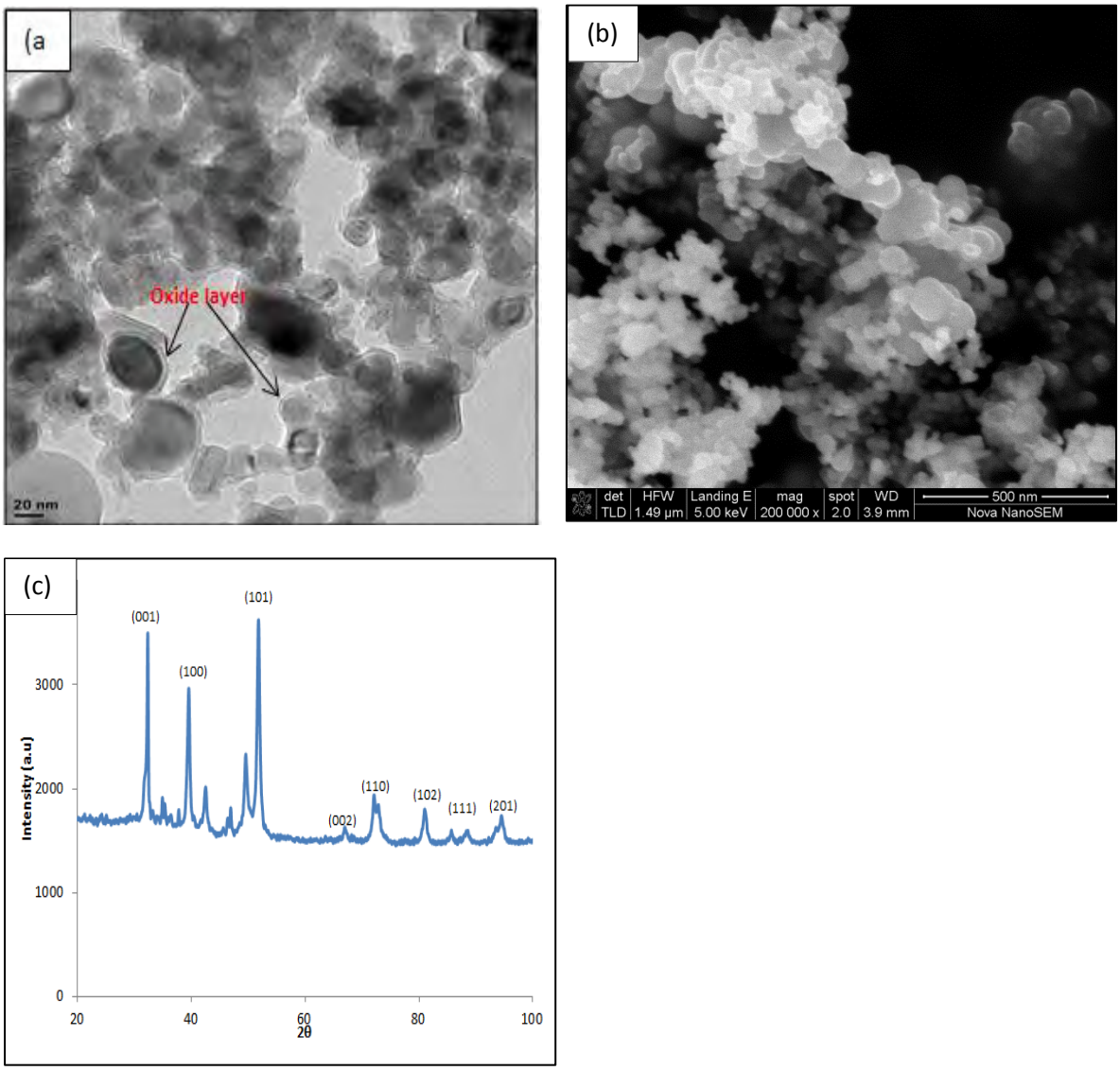

Figure 5.2 TiB_2 (a) TEM, (b) SEM image and (C) XRD pattern of scanning from 20-100 2θ

The measured TiB_2 particle size (38.0 ± 8.3 nm) from TEM and (41.6 nm) from XRD, did not match the one given by the supplier (58 nm). TEM image Fig. 5.2 (a) shows that TiB_2 has oxidized, by the presence of thin oxide layer, which is less than 2 nm on the surface of the material. The oxidation is confimed by the XRD pattern in Fig 5.2 (c). Peaks at *ca.* 35,37,42 and 46 2θ do not match the pattern from the database and literature (Yin et al., 2010. The data was analysed further to determine whether the oxide layer formed is B_2O_3 or titanium oxide phases or titanium borate ($TiBO_3$). Huang et al. (2002) claimed that TiB_2 films tend to oxidize at room temperature, in the presence of oxygen to form TiO_2 via the following reaction:

$TiB_2 + O_2 \rightarrow TiO_2 + 2B$

TiO_2 is formed rather than B_2O_3 due to favourable reaction energy, better stability and optimal protection towards further oxidation of the material. Oxidation of TiB_2 to TiO_2 is also reported in the study by Roth et al., (2014), where TiB_2 was used as Pt-support material for *in situ* testing. However, Kulpa & Troczynski (1996) claimed that TiB_2 oxidises to $TiBO_3$ and the process is reversible at low temperatures. Based on results in section 5.4, the oxidation layer is likely to be $TiBO_3$. The calculated lattice constant is 3.53 Å, which is slightly greater than the one reported in literature (3.02 Å). This shows that the material is partially oxidized. Moreover, the XRD peaks for TiO_2 and B_2O_3 from the database did not have a match with any of the unkown peaks from TiB_2's pattern. EDS analysis showed the presence of oxygen, but cannot be accurately quantified since B is undetectable. An impurity of 1.03 ± 0.25 wt % Cl was detected.

(iii) ZrB_2

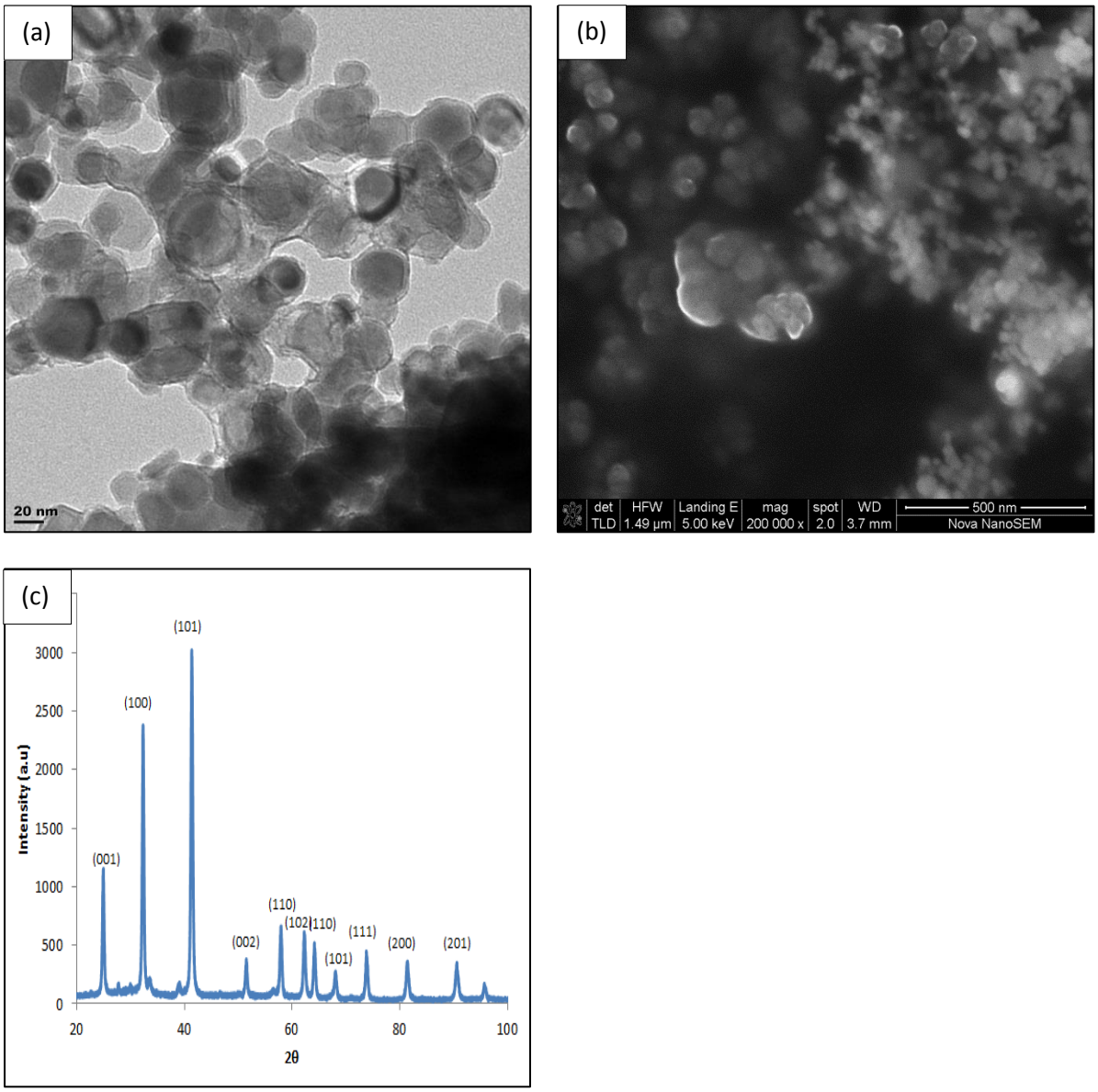

Figure 5.3 ZrB_2 (a) TEM, (b) SEM image and (c) XRD pattern scanning from 20-100 2θ

Similar to TiB_2, ZrB_2 showed a thin oxidation layer around nanoparticles, as seen from the TEM image in 5.3 (a). Oxidation peaks are observed at *ca*.26, 28, 31 and 38 2θ from the XRD pattern. These peaks are similar to the ones seen in the TiB_2 XRD pattern (two are adjacent to peak (100) and (101), and other two falls between peak (001) and (100). This shows that the oxide that is formed is similar to $TiBO_3$, hence, it is likely to be $ZrBO_3$. The measured particle size from TEM is 34.0 ± 10.5 nm, and from XRD, (001) peak is 26.8 nm. The average particle size reported by the supplier was 43 nm. EDS showed the presence of oxygen and 3.90 ± 1.31 wt% Cl.

(iv) ZrN

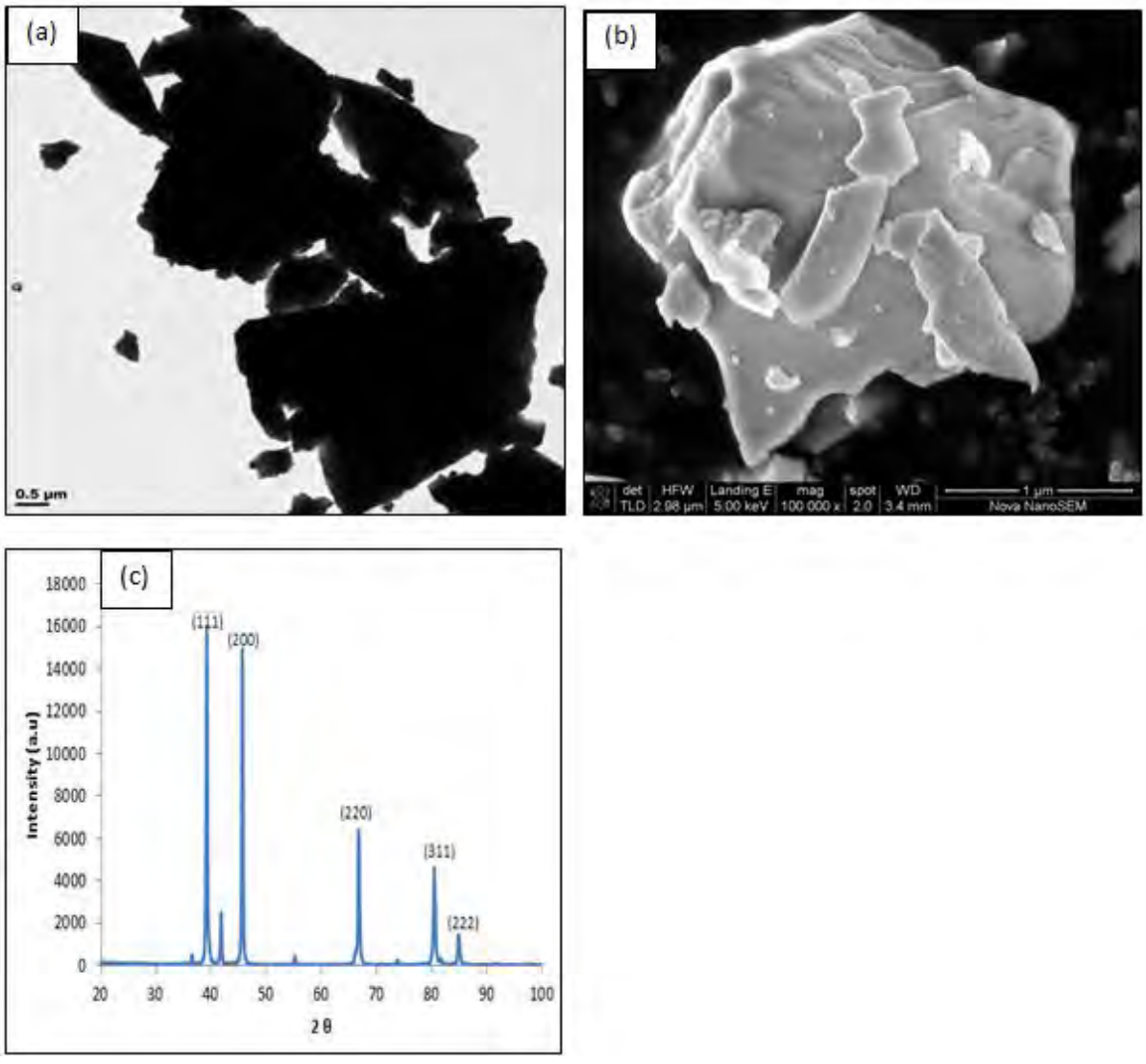

Figure 5.4 ZrN (a) TEM, (b) SEM image and (c) XRD pattern scanning from 20-100 2θ

ZrN particles appear dark under TEM due to large size and high density (7.09 $g.cm^{-3}$). The material is reported to have an average particle size of 1-2 µm and experimentally measured particle size is 1.70 ± 1.51 µm. However, it was difficult to accurately measure the size due to irregular morphology, as can be seen in Fig. 5.4 (a) and (b). However, the experimental

numbers were within the expected range as indicated in the specification sheet. The XRD pattern showed peaks at *ca.* 38, 42, 56 and 74 2θ, which did not match with the pattern of ZrN from the database. Cunha et al. (2006) showed that these peaks correspond to zircornium oxynitride ($Zr(NO)_X$).

EDS showed very minimal amount of oxygen content and according to the study by Cunha et al.(2006), it is claimed that at low oxygen content (below 6 at%) ZrN does not oxidize to form ZrO_2, but rather $Zr(NO)_X$. Oxygen atoms diffuse into ZrN lattice and occupy interstitial sites. The measured lattice constant *'a'* is 4.62 Å and theoretical *a* is 4.58 Å (Bazhanov et al.,.2005)

(v) LaB_6

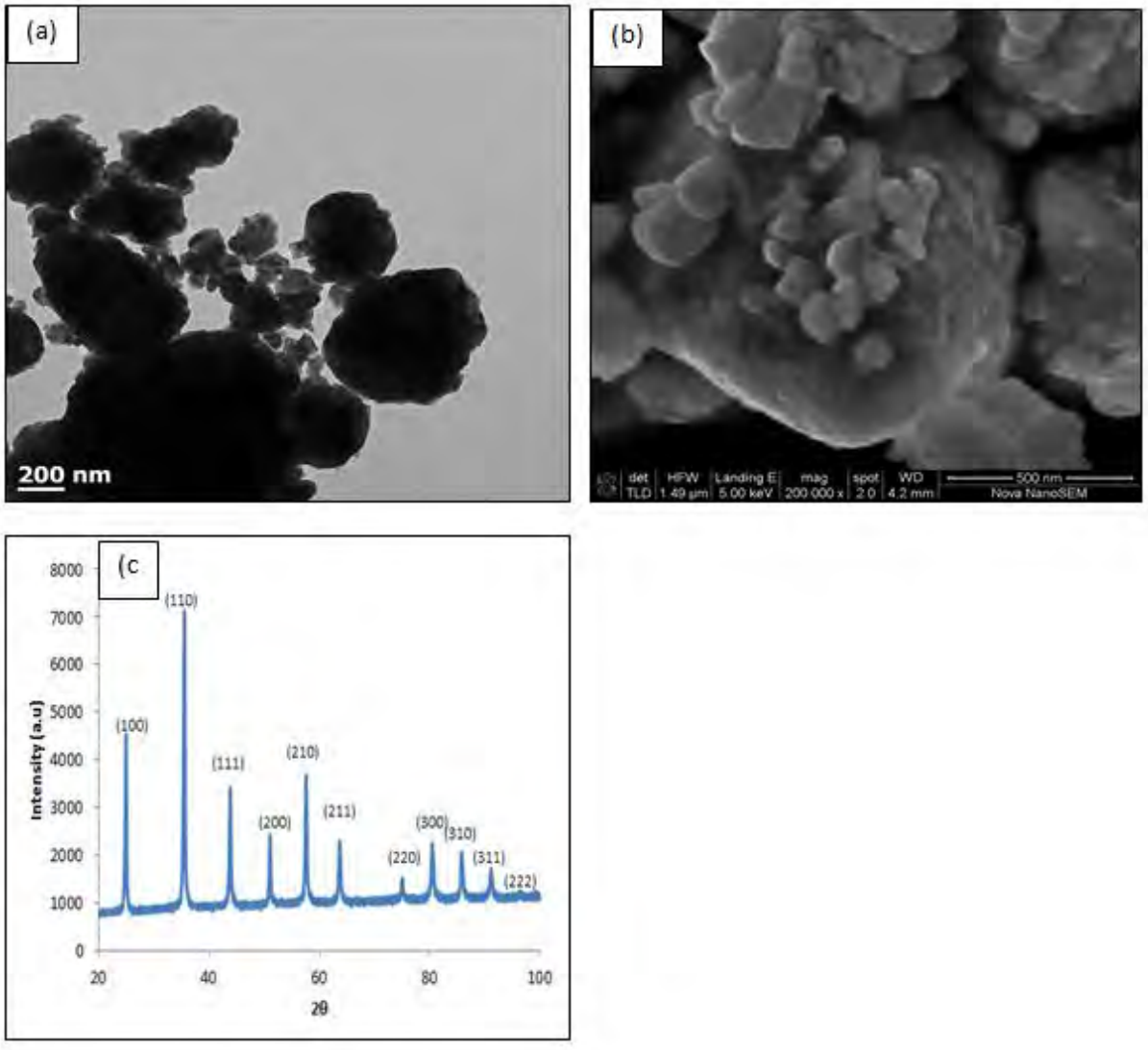

Figure 5.5.LaB_6 (a) TEM, (b) SEM image and (C) XRD pattern scanning from 20-100 2θ

LaB_6 is reported to have a particle size less than 100 nm, according to the supplier. However, the measured particle size was found to be 350 ± 144 nm. Similar to ZrN, the support

appears dark under TEM due to this large particle size. The XRD pattern was consistent with the pattern from the database. EDS showed no impurities.

5.1.3 BET

BET Measurements were carried out to determine specific surface area (SSA) and porosity of support materials and results are as follows:

5.1.3.1. Specific surface area (SSA)

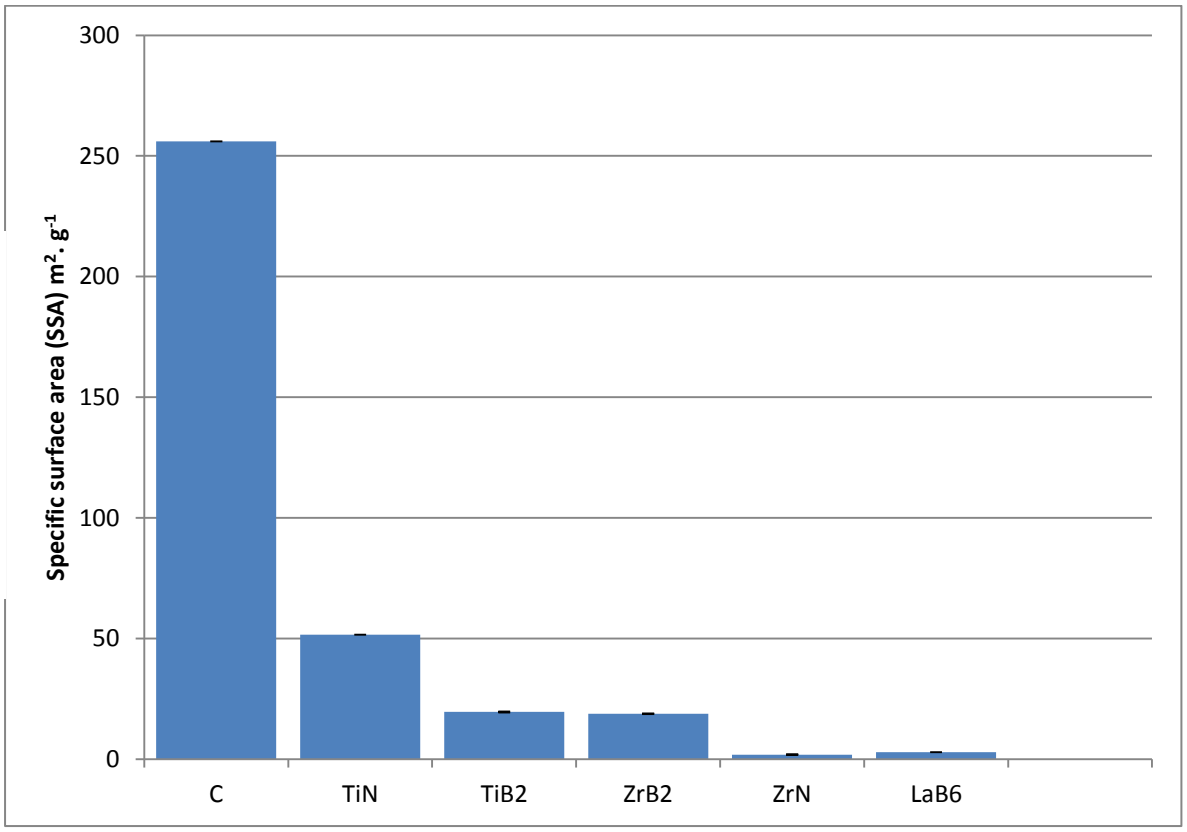

Figure 5.6 BET surface area of metal nitrides, borides and Vulcan XC-72 (C) as benchmark

The BET results showed that C has the highest SSA, followed by TiN. For TiB_2 and ZrB_2 SSA is almost the same. LaB_6 and ZrN have the lowest SSA. The specific surface area depends on the size of particles and density of materials. Vulcan XC-72 has an average particle size of about 50 nm, which is similar to TiB_2 and ZrB_2 and larger than TiN, however its apparent density is an order of magnitude lower (0.264 $g.cm^{-3}$) than the nitrides and borides under investigation in this work. Therefore the specific surface area of Vulcan XC-72 is about 5-10 times higher. To exclude differences in Pt coverage on the surface when comparing the inorganic support materials the Pt loading will be calculated on a per volume basis rather than per weight basis.

5.1.3.2 Porosity of metal nitrides and borides

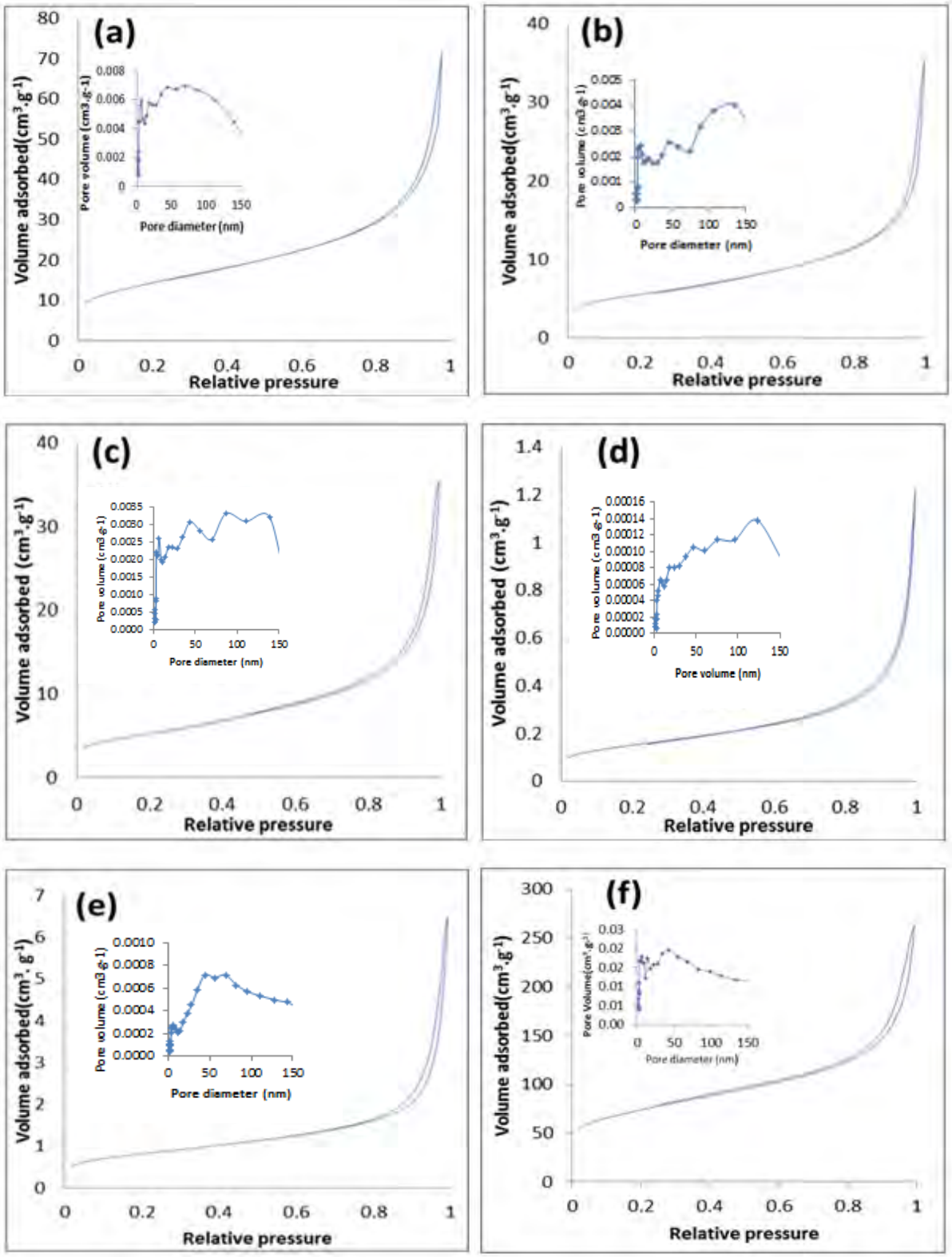

Figure 5.7 N_2 adsorption-desorption isotherms of (a) TiN (b) TiB_2, (c) ZrB_2 (d) ZrN (e) LaB_6 (f) C (Vulcan XC-72). The inset shows BJH pore size distribution.

According to IUPAC classification (Brunauer et al., 1940), the hysteresis loops of adsorption and desorption of N_2 on metal nitrides, metal borides and Vulcan XC-72 (carbon) at 77.35 K, shows a similar combination of type I and II isotherm behaviour. This indicates the presence of micro- and macro-pores. The pore size distribution is presented by BJH adsorption curves. All the support materials showed a very broad size distribution. This confirms that the inter-particle space consists of micro and macro-pores. However, the pore volume of inorganic support materials is much lower than that of carbon.

5.2 Physical characterisation of metal nitride and borides after Pt deposition and Pt/C.

5.2.1 Pt/C (benchmark)

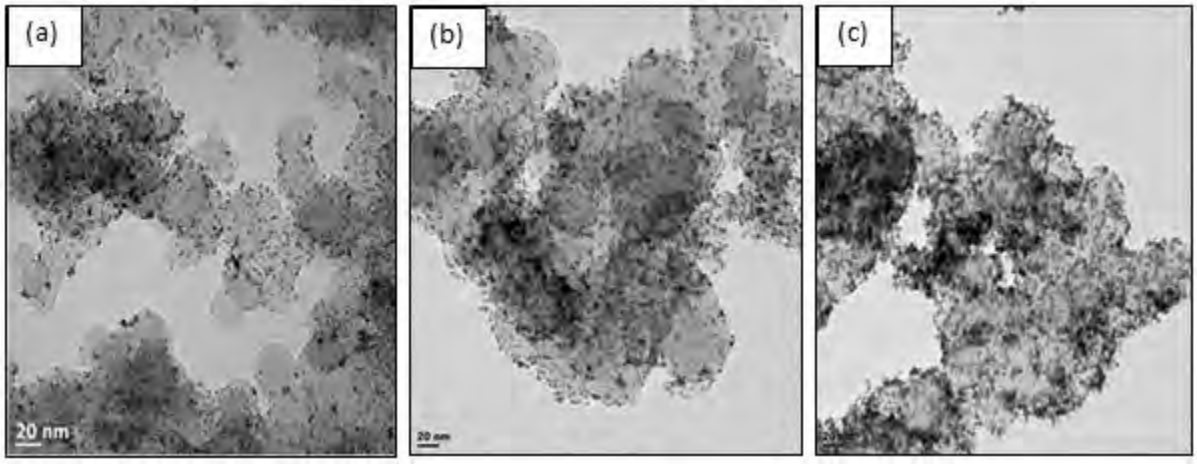

Figure 5.8 (a) 20 wt% (b) 40 wt % and (c) 60 wt% Pt/C

Three Pt/C catalysts with different loading (20 wt %, 40 wt % and 60 wt%) were used as the benchmark. The particle size from TEM images is 2.5 ± 0.7 nm, 3.4 ± 0.7 and 4.3 ± 0.9 nm, respectively. The particle size calculated from XRD data is slightly different from the one measured from TEM, as it is shown in table 5.1. The difference is due to the fact that XRD provides the crystallite size from averaging the volume across the sample (Kocha & Takahashi, 2010). As expected, the measured particle size gets larger as the loading increases. If particles are deposited in closer proximity to each other, agglomeration is more likely to occur.

As stated before, the v/v% of Pt/C was used to determine the amount of Pt to be deposited on metal nitrides and borides, with the goal to deposit the same amount of Pt per unit area of the support. The v/v% equivalent to 20, 40 and 60 wt % of Pt/C, were calculated and found to be 1.68, 3.36 and 5.04, respectively. A wet chemical (impregnation) and organo-metallic chemical vapour deposition (OMCVD) technique were used, and the following results were obtained:

5.2.2 Pt on metal nitrides and borides materials

(i) 1.68 v/v%, equivalent to 20 wt% Pt/C

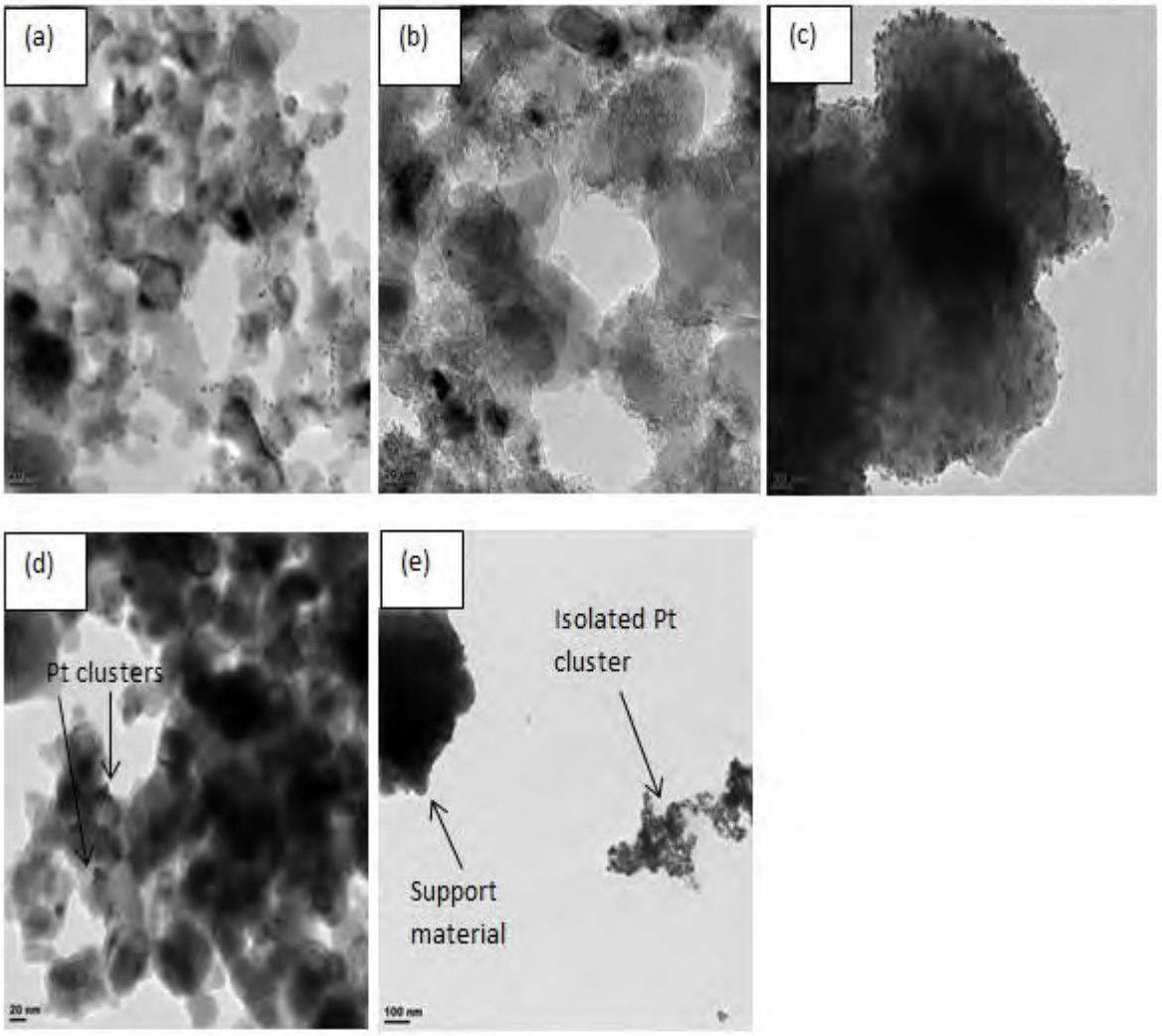

Figure 5.9 TEM images of catalysts prepared by OMCVD technique (a) TiN (b) TiB_2 (c) LaB_6 (d) ZrB_2 and (e) ZrN

(ii) 1.68 v/v%, equivalent to 20 wt% Pt/C

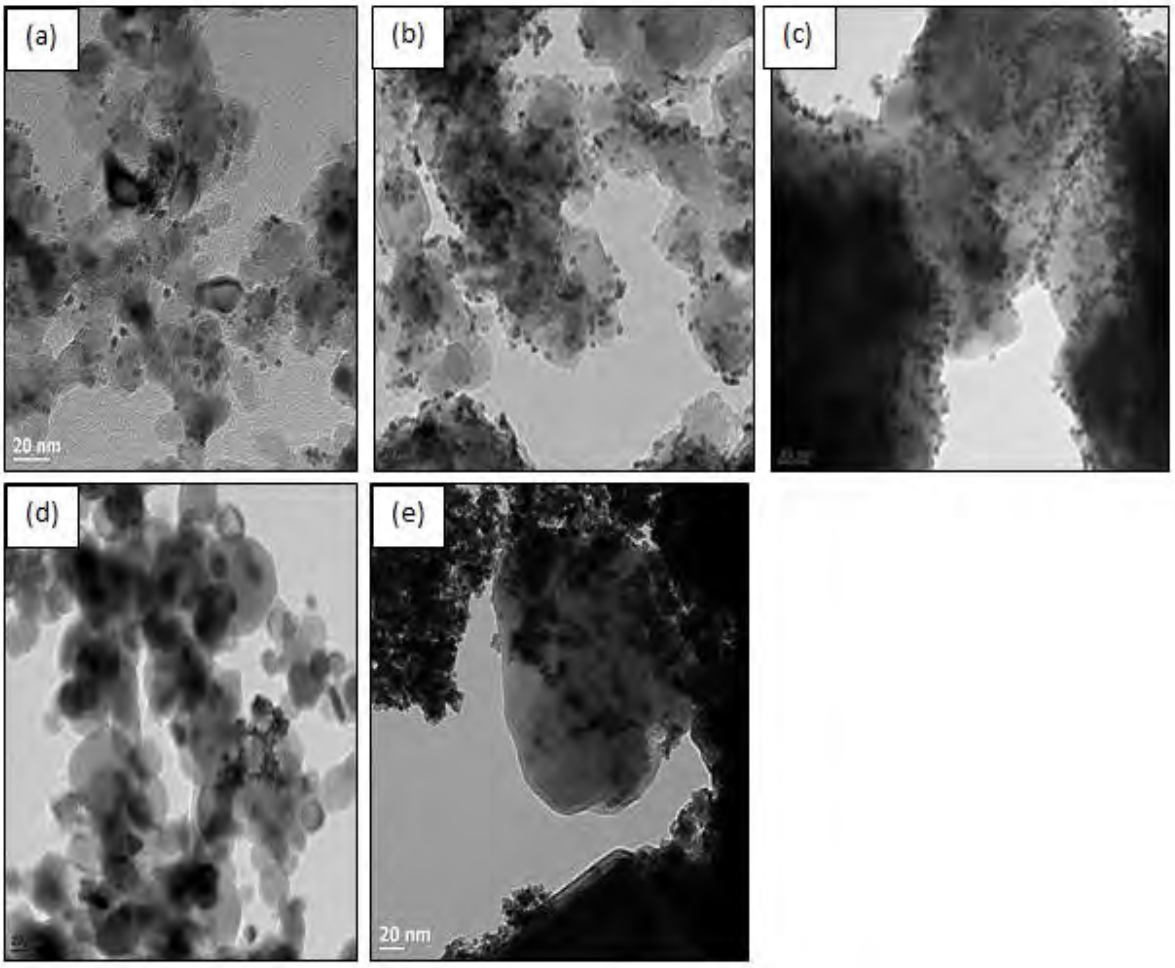

Figure 5.10 TEM images of catalysts prepared by wet impregnation method to deposit 1.68 v/v% Pt on (a) TiN (b) TiB_2 (c) LaB_6 (d) ZrB_2 and (e) ZrN

From Fig 5.9 and 5.10 (d & e), isolated Pt clusters are observed on TEM images of ZrB_2 and ZrN for both deposition techniques. For the wet chemical deposition technique employed in this work pH is determined by Pt precursor and not the potential of zero charge of the support, this might have led to poor interaction between the support and the particles formed during deposition.However, since the same observation is made for samples of ZrN and ZrB_2 prepared using OMCVD, this suggests that in general a low metal-support interaction for these materials.However, it is not distinghushable whether this is due to ZrN and ZrB_2 chemical inertness (Jones & Hitchman, 2009) or due to oxidation products (from section 5.1.1) on the surface of these materials. Unsupported Pt particles have high surface energy and tend to agglomerate to lower the energy of the system, as observed.

From Fig. 5.9 (b) It could be seen that Pt precipated as agglomerates rather than as particles on TiB_2, using OMVCD. In contrast, the wet chemical deposition technique (Fig. 5.10 (b)) produced well dispersed Pt particles with an average size of 3.8 ± 0.7 nm in the presence of oxidation products on its surface. In light of the above this seems to further indicate that Zr-

based supports are chemically inert. Depositing Pt on ZrB_2 and ZrN would require coupling agent or pre-treatment to modify the surface. However, surface modification techniques tends to reduce the stability of the material (Yin et al. 2010). Therefore, these materials were not taken for further studies/analysis in this research project. However, the electrochmical stabilty experiment was conducted for comparison purpose.

Fig 5.9 and 5.10 (a & c) Both techniques produced well dispersed Pt on TiN and LaB_6 , in the same partcle size range (4.0 - 4.5 nm). However, since OMCVD failed to deposit well dispersed Pt particles on TiB_2, the wet chemical deposition technique was considered as the method of choice for Pt deposition on the metal nitrides and borides in this work. This technique was then further employed to deposit 3.36 and 5.04 v/v% Pt on TiN, TiB_2 and LaB_6, and results are as follows:

(iii) 3.36 v/v%, equivalent to 40 wt% Pt/C

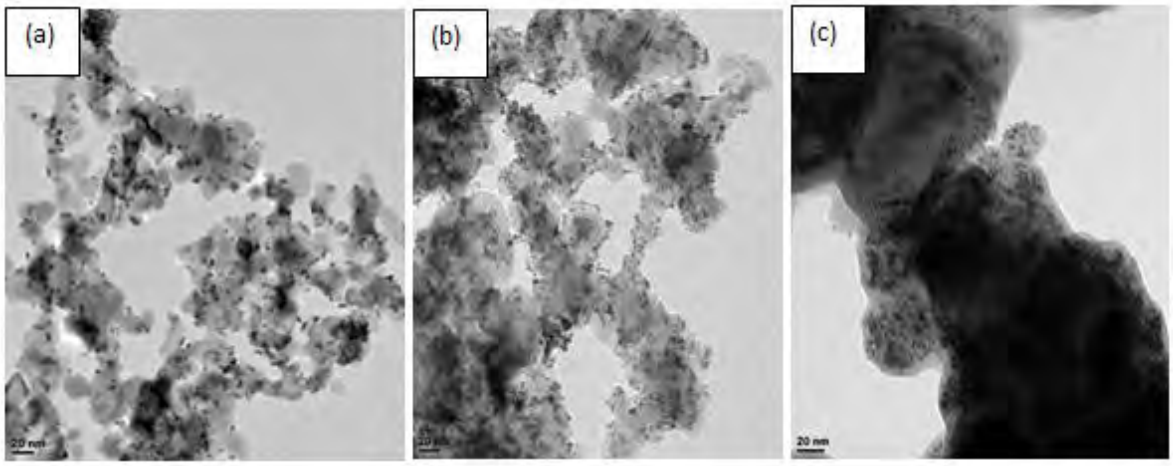

Figure 5.11 TEM images of catalysts prepared by wet impregnation method to deposit 3.36 v/v% Pt on (a) TiN (b) TiB_2 (c) LaB_6

(iv) 5.04 v/v%, equivalent to 60 wt % Pt/C

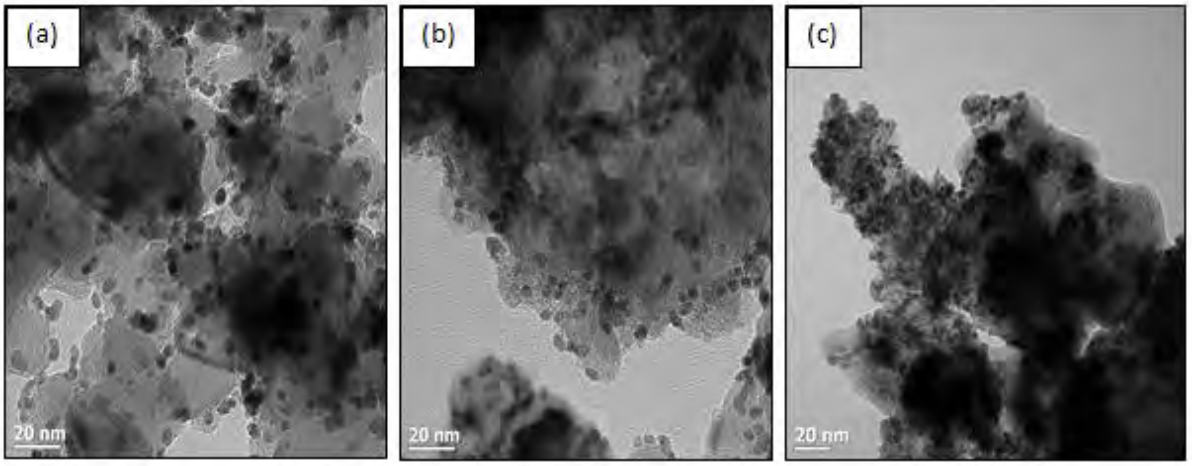

Figure 5.12 TEM images of catalysts prepared using precipitation method to deposit 5.04 v/v% Pt on (a) TiN (b) TiB_2 (C) LaB_6

From above images obtained from TEM, the particle size measured using ImageJ and the results are tabulated in Table 5.1. Furthermore, the XRD data (Fig 5.13) was used to determine the Pt crystallite size, using Pt (111) and (200) peaks.

5.2.4 XRD

The benchmark Pt/C and synthesised catalysts were analysed by XRD. However, only 1.68 v/v% Pt catalysts are presented below; since 3.36 and 5.04 v/v% showed similar patterns.

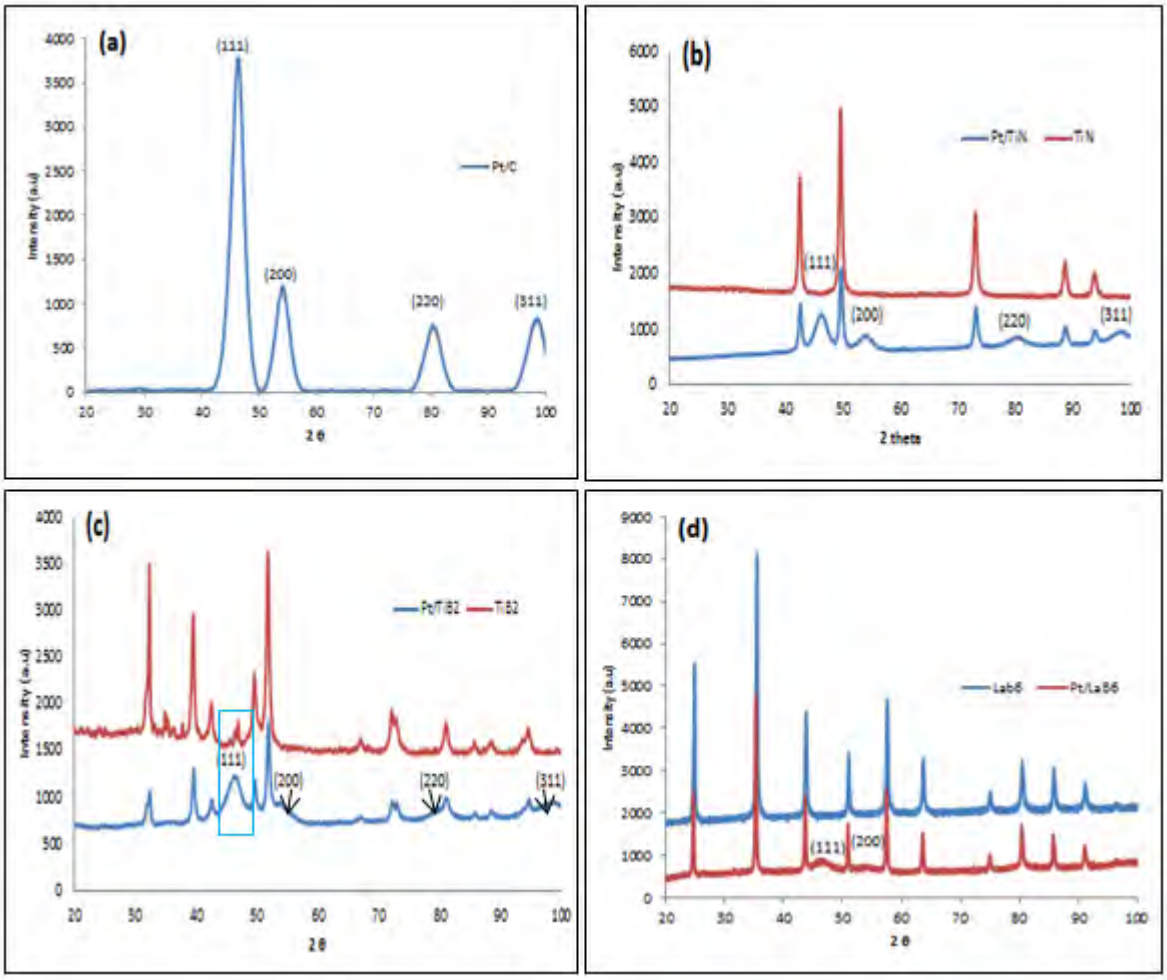

Figure 5.13 Typical XRD patterns of (a) Pt/C, (b) Pt/TiN (c) Pt/TiB_2 , (d) Pt/LaB_6

XRD patterns obtained were plotted on the same axis with XRD data of pure support materials. As shown in Fig 5.13 (c) Pt/TiB_2 peak Pt (111), Pt (200) & (220) overlap with peaks of the support. Therefore, XRD data cannot be used to calculate the size of Pt on $_{TiB2}$. However, for TiN and LaB_6 the peaks were distinct and isolated. Therefore, the Debye - Scherer equation was used to calculate the size and the results are tabulated in Table 5.1.

Table 5.1 Pt particle/crystallite size measured from TEM images and XRD data.

	1.68 v/v%		3.36 v/v%		5.04 v/v%	
	TEM particle size (nm)	**XRD particle size (nm)**	**TEM particle size (nm)**	**XRD particle size (nm)**	**TEM particle size (nm)**	**XRD particle size (nm)**
Pt/C	2.5 ± 0.7	3.3	3.4 ± 0.7	3.9	4.3 ± 0.9	4.0
Pt/TiN	4.0 ± 0.6	4.8	4.1 ± 0.73	4.8	4.5 ± 0.7	4.8
Pt/TIB_2	3.8 ± 0.7	-	3.9 ± 0.75	-	4.3 ± 0.5	-
Pt/LaB_6	3.9 ± 0.7	4.5	3.7 ± 0.67	4.8	4.2 ± 0.5	4.9
Please note that for TiB_2 Pt peaks overlapped with the support, thus Pt crystallite size could not be measured using Debye-Scherer-equation.						

As shown in Table 5.1, the Pt particle size increases as Pt loading increases for Pt/C, Pt/TiB_2 and LaB_6, as expected; due to closer proximity at which Pt nanoparticles are being deposited and high surface energy of Pt nanoparticles, agglomeration is likely to occur. However, for Pt/TiN the Pt crystallite size did not change significantly across all three loadings, this is attributed to strong metal support interaction. Pt migration is restricted on TiN surfaces; therefore, Pt agglomeration is less likely to occur. As stated before the particle size measured from TEM and XRD is different due to the fact that XRD provides the crystallite size from averaging the volume across the sample (Kocha & Takahashi, 2010).

5.2.5 Metal loading

ICP was used to determine Pt loading on the benchmark and Pt supported on metal nitrides and borides. However, ICP gave inaccurate results for Pt/C and Pt/TiN. Measured loading was significantly lower than the expected value, with the error being as high as 35%. To overcome this, alternative methods were used. For Pt/C, thermogravimetric analysis (TGA) was used to determine Pt loading. The initial mass of the catalyst was measured before carbon was combusted and the final mass after combustion represents the mass of Pt. For Pt/TiN, EDS was used, as TiN decomposes at high temperature (melting point: 2950 °C (Hu et al. 2000) and TGA would not work. The following results were obtained for Pt/C (Table 5.2) and Pt/TiN with all other catalysts (Table 5.3).

Table 5.2 Benchmark Pt/C

Electrocatalyst	**Anticipated (wt%) loading**	**Calculated (wt%) loading**	**Deviation (%)**
20 wt% Pt/C	20	20.6	3.1
40 wt% Pt/C	40	40.5	1.3
60 wt% Pt/C	60	58.6	2.3

Table 5.3 Pt/metal nitrides and borides

	Equivalent to 20 wt% Pt/C			Equivalent to 40 wt% Pt/C			Equivalent to 60 wt% Pt/C		
	Loading (wt%)	**Calc. loading (wt%)**	**Dev. (%)**	**Loading (wt%)**	**Calc. loading (wt%)**	**Dev. (wt%)**	**Loading (wt%)**	**Calc. loading (wt%)**	**Dev. (%)**
Pt/TiN (EDS)	6.7	6.8±1.8	2.7	13.3	13.1±2.1	1.6	20.0	19.2±3.4	3.6
Pt/TiB_2	8.0	7.8	2.1	15.9	15.1	5.0	23.9	22.9	4.1
Pt/LaB_6	7.6	7.2	5.0	15.2	14.4	5.4	22.9	21.2	7.1

As shown in Table 5.3, the wet chemical deposition method results in accurate deposition of desired Pt amount on metal nitrides and borides. The highest error was observed on Pt/LaB_6 (7.2%). For other catalysts the error ranged from 1.6 -5.4 %.

5.3 Electrochemical stability of support materials

CV technique was used to determine the electrochemical stability of the supports in 0.1 M $HClO_4$ at room temperature. A total of 3000 cycles were recorded over 25 hours, scanning from 0 – 1.5 V vs SHE at 100 $mV.s^{-1}$. The following results were obtained:

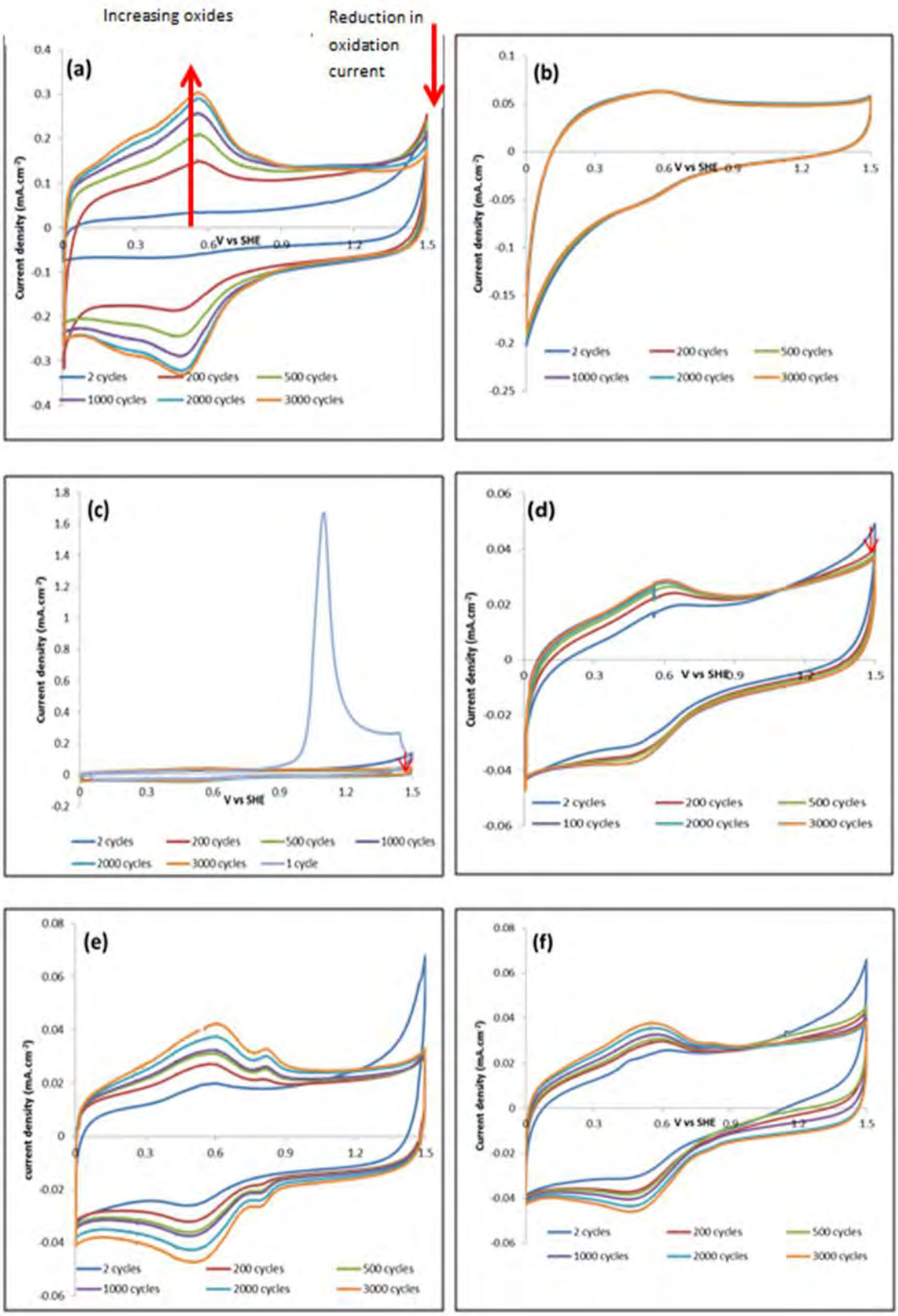

Figure 5.14 Electrochemical stability of support materials (a) Vulcan XC-72 (C) (b)TiN (c) TiB_2 (d) ZrN (e) ZrB_2 (f) LaB_6 (0.1 M $HClO_4$, 1.0 - 1.5 V vs SHE, 100 $mV.s^{-1}$, room temperature)

As shown in Fig. 5.14, for all support materials the current in redox region increased due to capacitance. Vulcan XC-72 carbon (C) showed least stability as expected. Literature has reported that carbon oxidizes to form surface oxides due to hydroquinone-quinone redox coupling (Yin et al. 2010). Carbon oxidizes via the following reactions (Kinoshita, 1988):

$C \rightarrow C_s^+ + e^-$

$2\ C_s^+ + 2\ H_2O \rightarrow 2\ C_sO + 4H^+ + 4\ e^-$

And in the redox region, C_sO species are hydrolysed via the following reaction:

$C_sO + H_2O \rightarrow CO_{2\,(g)} + 2H^+ + 2e^-$

As seen in Fig 5.14 (a), as more oxides are formed on carbon surface, the oxidation current at 1.5 V vs SHE is progressively decreasing over number of cycles. This shows that oxides reduce the rate at which C is oxidized to C_s^+. However, regardless of the presence of oxides, C is still diminishing. After the stability test, the Vulcan (carbon) thin film on the electrode had almost entirely disappeared.

On the other hand, TiN shows great stability over 3000 cycles. Under load cycling, a very small current increase was observed in the redox region, which is an indication of formation of oxides and oxynitrides. Similarly to carbon, at 1.5 V vs SHE the current is decreasing over the first 200 cycles, while the current is increasing in the redox region. After 200 cycles, the material is fully passivated, as there is no change in current in both regions (1.5 V vs SHE and redox region). This shows that oxides that are formed are enough to provide sufficient protection towards further oxidation.

Avasarala et al. (2010) showed that from 1.0 - 1.5 V vs SHE titanium hydroxides are formed via the following reactions:

$TiN + 3H_2O \rightarrow Ti(OH)_3 + ½\ N_2 + 3H^+ + 3e^-$ (I)

$TiN + 3H_2O \rightarrow TiO_2.H_2O + 1/2N_2 + 4H^+ + 4e^-$ (II)

The hydroxides that are formed (reaction I and II) dissociate in the electrolyte and produce Ti^{3+} and TiO_2.

Once the experiment was done the electrolyte was analysed using ICP to confirm the presence of titanium ions. ICP reported 24.8 ppb Ti ions in the electrolyte. This confirms that Ti was leached during cycling. The CV patterns suggest that Ti was leached at ca. 1.3 - 1.5 V vs SHE over the first 200 cycles before the material reached its passivation point.

The formation of TiO_2 via dissociation of $TiO_2.H_2O$ (reaction II) raised the current in the redox region. As more oxides are formed, the material becomes passivated. Pre-existing oxynitrides (discussed in section 5.1.1 (i)) and formation of TiO_2 on the surface of TiN during cycling, prevented further oxidation of TiN. The passivation/stability of the material was

maintained over the entire experiment. Once enough oxides are formed, the system is at equilibrium. After the stability test, the material was removed from the electrode and was analysed using XRD. This was done to investigate whether the material was still TiN or completely converted to TiO_2, and the results are as follows.

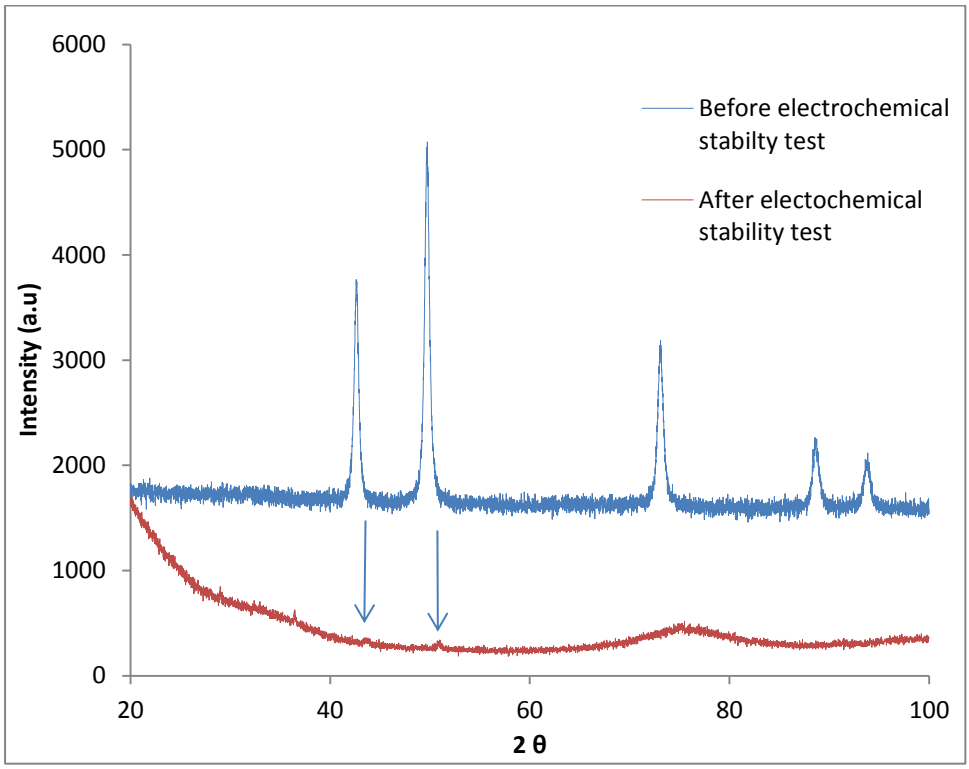

Figure 5.15 XRD pattern of TiN before and after electrochemical stability test

As shown in Fig 5.15, the arrows show peaks of TiN (these peaks matched $TiN_{0.98}$ from ICDD database). However, in comparison with TiN before the test, peak (111) and (200) is slightly shifted to the right. D-spacing of peak (111) was measured to determine the lattice constant, and it is found to be 4.22 Å. This value lies between the lattice constant of TiN (4.24 Å) and TiO_2 (4.18 Å). This is consistent with bulk material remain as TiN and only the surface was oxidised. These findings are consistent with the study by Avasalara et al. (2010), where he investigated the electrochemical stability of TiN for PEFCs applications.

TiB_2 (Fig 5.14 (c)) showed major oxidation peak between ca. 0.9 -1.5 V vs SHE in the first cycle. This may be attributed to oxidation of pre-existing oxides on the surface, as shown in Fig. 5.2 (a). If these oxides were TiO_2, a similar CV profile to TiN would have been observed during first few cycles. This indicates that these oxides are less stable in comparison to TiO_2. Therefore, they are mostly likely to be $TiBO_3$, as discussed in section 5.1.1. After removal of $TiBO_3$, the material shows the following behaviour (Fig. 5.16),

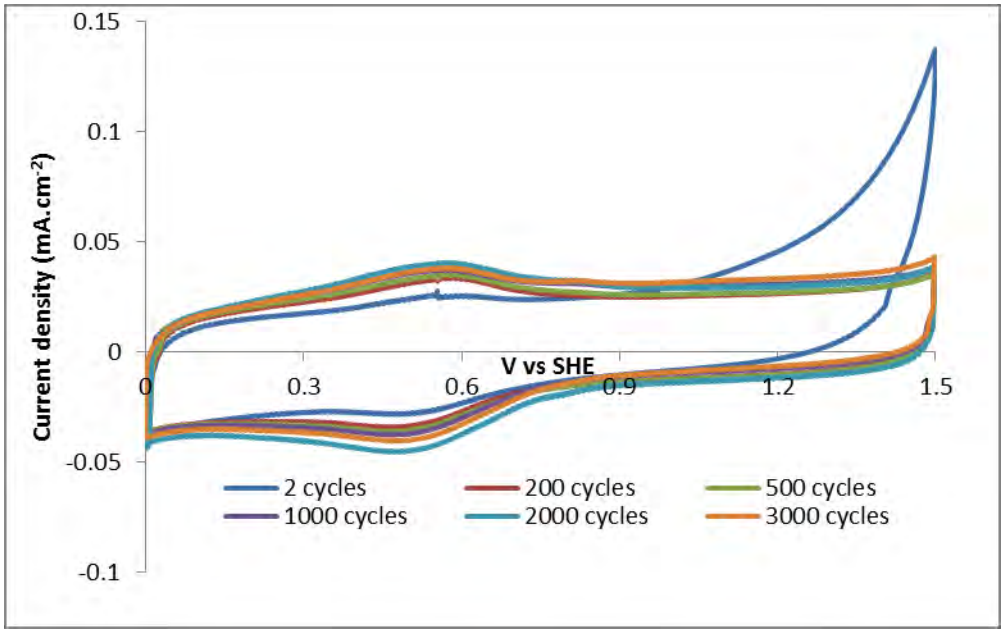

Figure 5.16 Reproduced from Fig 5.14 (c) TiB_2 showing cycle 2-3000.

Similarly to TiN and carbon, at 1.5 V vs SHE the current is decreasing over the first 100 cycles (cycle 100 not shown in the diagram) due to formation of hydroxides. As the hydroxides are formed, the current is increasing in the redox region due to formation of oxides and Ti^{3+} species are produced. TiB_2 did not show complete passivation as TiN, since metal borides form B_2O_3 on its surface rather than metal oxides (Lavrenko et al., 1974). B_2O_3 is not as stable as metal oxides and does not offer sufficient resistance towards further oxidation. This is observed in the figure above, as the current is constantly changing at 1.5 V.

These results are not consistent with literature. Yin et al. (2010) claimed that TiB_2 does not form oxides on its surface, as there was no change in the redox region after holding the electrode at 1.2 V for 48 hours. However, on the same paper he reported the concentration of Ti ions in the electrolyte as $0.07\mu g.ml^{-1}$ and did not show how Ti was produced in the electrolyte. Form this study it could be seen that the Ti he measured was from the oxidation of TiB_2. Therefore, TiB_2 is not immune to oxidation under fuel cell conditions.

The voltammograms obtained for ZrN, ZrB_2 and LaB_6 (Fig. 5.14 (d), (e) & (f)), shows similar behaviour at 1.5 V vs SHE to previously discussed materials. This shows that metal hydroxides were formed. After 1000 cycles ZrN Fig 5.14 (c) reached its passivation point, as the surface had formed ZrO_2. ICP results showed negative results for Zr concentration; probably the concentration was below detection limit. However the pourbaix diagram of Zr in water shows that the material is not stable under acidic conditions. From these results it can ben that ZrN oxidises to form a passivation layer but not ZrB_2. Hence, nitrogen and boron are major determinants of the electrochemical stability.

ZrB_2 (Fig 5.14 (e)) and LaB_6 (Fig 5.14 (f)) does not show any mechanism of passivation. La^{3+} is constantly produced, via the following reaction: $LaB_6 + 18H_2O \rightarrow La(III) + 6H_3BO_3 + 18H^+ + 21e^-$

(Curran D.J. & Fletcher K.S, 1968), while oxides are formed in the redox region. Hence, the oxides formed do not offer sufficient corrosion resistance, as stated above and showed by (Lavrenko et al., 1974). The concentration of La leached was not quantified due to unavailability of the reference standard at UCT.

The change in oxidation current (positive sweep) between 0.5 - 0.6 V vs SHE was recorded and the rate of oxidation was calculated as shown in the table below, for the materials that showed least stability.

Table 5.4 Change in oxidation current from cycle 2-3000 for C, ZrB_2, TiB_2 and LaB_6

Support materials	**Initial current density ($i_{l\ (mA.cm^{-2})}$)**	**Final current density ($f_{l\ (mA.cm^{-2})}$)**	**$\Delta = f_l - i_l$ ($mA.cm^{-2}$)**	**Rate of oxidation ($\mu A.cm^{-2}$/cycle)**
Carbon	0.002	0.310	0.308	102
TiB_2	0.025	0.042	0.017	5.67
ZrB_2	0.019	0.042	0.024	8.00
LaB_6	0.024	0.037	0.013	4.34

As shown in Table 5.4, the oxidation rate of carbon is *ca.* 24 times more than that of LaB_6, 18 times more than TiB_2 and 13 times ZrB_2. Therefore, LaB_6 and TiB_2 are still a better alternative to C.

Based on the results above, it can be seen that electrochemical stability of these materials is based on the parental metal and also on the light elements (B, N). N-based materials are more electrochemically stable than B-based. Metal nitrides oxidized to form stable metal oxides, while metal boride formed B_2O_3. This is attributed to the fact that N on interstitial sites is easily substituted by oxygen in the lattice. While in metal borides it is thermodynamically favourable to form boron oxides rather than metal oxides. The electronegativity of B is 2.0, Ti is 1.5 and Zr is is 1.3; therefore, oxygen will have stronger binding affinity with boron than either Zr orTi.

5.4 Electrochemical Characterisation of Pt supported on metal nitrides and borides

5.4.1 Establishing reliable electrochemical methods for metal nitride and metal boride supports

As can be seen from previous sections, the supports under investigation in this work show very different behaviour compared to carbon. Therefore, before going into full electrochemical investigation of the catalysts prepared, it was first established if standard electrochemical techniques for fuel cell catalysts (CV, RDE) are applicable as such with these materials.

5.4.1.1 Calculation of theoretical values as benchmark

Before commencing with electrochemical measurements, the theoretical surface area and the diffusion limiting currents for LSV at different rotation speeds were calculated.

To calculate the theoretical surface area the following assumptions were made:

(i) All Pt particles supported on metal nitrides and borides are spherical

(ii) All Pt particles are uniform and have the same size

Surface area of Pt particle = $4\pi r^2$ and volume of Pt particle= $4\pi/3 * r^3$

Volume of Pt particle * density of Pt = mass of Pt

Therefore, theoretical maximum ECSA ($m^2.g^{-1}$) = surface area of Pt particle/mass of Pt, and the following results were obtained, using the particle size measured in section 5.3.4 (Table 5.2):

Table 5.5 Theoretical ECSA calculated using Pt particle size

	Theoretical specific surface area ($m^2.g^{-1}$)		
catalyst	**1.68 v/v%**	**3.36 v/v%**	**5.04 v/v%**
Pt/C	83.8	71.9	71.3
Pt/TiN	58.1	58.0	57.6
Pt/TiB_2	72.7	71.8	64.4
Pt/LaB_6	61.9	58.2	56.0

However, it should be noted that measured ECSA will be smaller compared to the theoretical, since at the interface area between Pt and the support is not electrochemically active and cannot be measured.

Diffusion limiting currents for LSV at different rotation speeds were calculated using the Levich equation below and tabulated in Table 5.6:

$$i_{d,theoretical} = 0.620nFA_E D^{\frac{2}{3}} w^{\frac{1}{2}} v^{-1/6} C$$

Where, n=4 is the number of electrons, F denotes Faraday constant, A_E =0.196 cm^{-2} is the area of the disk, w is the angular rotation speed (400 - 2500 rpm), v is kinematic viscosity of the electrolyte and C is the concentration of reactants.

Table 5.6 i_d, theoretical for 5mm glassy carbon disk used for RDE and RRDE studies

Rotation speed (rpm)	**i_d, theoretical**	
	mA	**mA.cm^{-2}**
400	0.593	3.02
900	0.890	4.53
1600	1.19	6.04
2500	1.48	7.55

5.4.1.2 Influence of support material on ECSA measurement

All CV measurements were carried out in Ar saturated 0.1 M $HClO_4$ scanning from 0.0 V – 1.1 V vs SHE at 20 $mV.S^{-1}$ at room temperature(20 ± 2 °C). The temeperature flactuations are negligible on the electrochemical results based on Nerst equation:

$E = E_O + \frac{RT}{NF} - InQ$ (Barbir, 2005)

Where, E denotes potential, F is Faraday's constant, n= number of of moles of electrons exchangd in the electrochemical reaction, R = gas constat, T= temparature and Q is the reaction quotient of ions.

The change in temperature is so small (2°C), to affect the kinetics of reactions taking place on the system.

RDE studies were carried out in the same electrolyte saturated with O_2 scanning from 0.1 – 1.2 V vs SHE at 5 $mV.s^{-1}$.

CV measurements of 1.68 v/v% were characterised first and the following results were obtained.

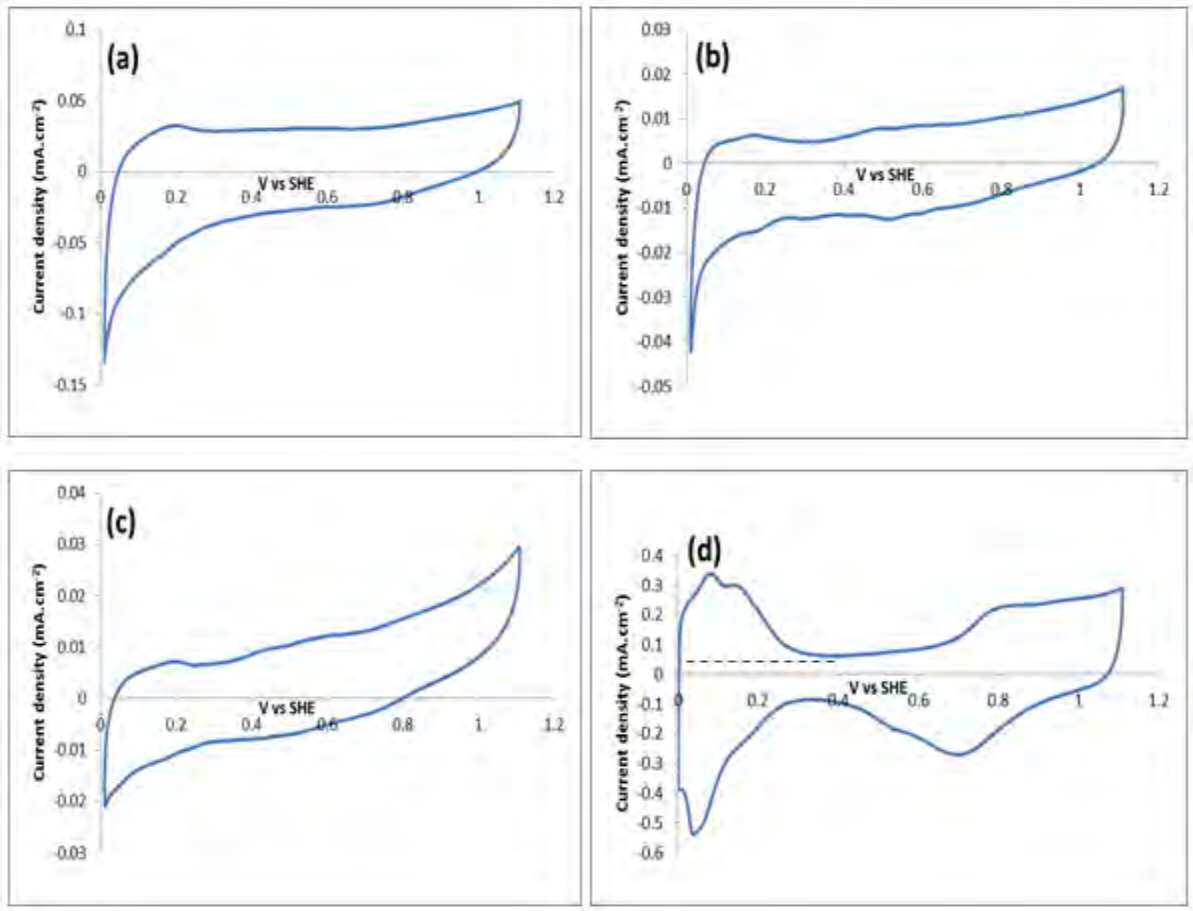

Figure 5.17 CV profile of 1.68 v/v% Pt on (a) TiN (b) TiB_2 , (c) LaB_6 and (d) Vulcan (C) (0.1 M $HClO_4$, 20 mV.s^{-1})

As shown in Fig 5.17, 1.68 v/v% Pt on metal nitrides and borides does not show a typical CV profile similar to that of Pt/C. The current in the double layer region is increased due to capacitance of oxides formed. H_{ads} and H_{des} peaks are observed, however, they are not as distinct as for Pt/C. Since the double layer is charging, it cannot be used to extrapolate the baseline for H_{ads}/H_{des} peak integration to determine the underpotential deposition charge. Therefore, ECSA cannot be calculated from this data. Hence, CO stripping was attempted as an alternative method. However, before commencing CO stripping measurements, metal nitrides and borides were electrochemically tested for activity towards CO oxidation. A bare nitride or boride electrode (i.e. without Pt deposited) was held at 0.1 V vs SHE for 30 min before cycling from 0 – 1.1 V vs SHE five times. The electrolyte was then saturated with CO for 20 min, while the electrode was held at the same potential as previously. After 20 min the electrolyte was purged with Ar for 30 min and the following results were obtained.

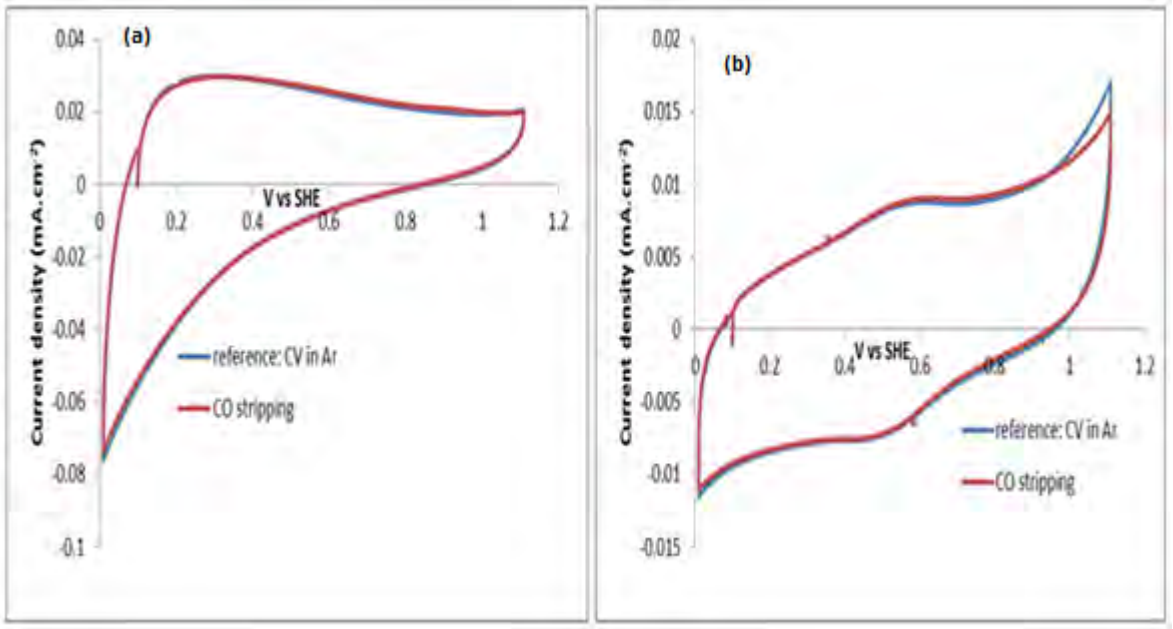

Figure 5.18 CO stripping teston (a) TiN (b) TiB_2 at 20 $mV.s^{-1}$

As it can be seen from Fig 5.18, for TiN and TiB_2 materials there is no difference between the CV recorded under inert conditions and CO , hence all three support materials did not show any activity toward CO oxidation. It was also observed that above 1 V vs SHE, TiN and TiB_2 form $Ti(OH)_3$ and potential cycling the amount of hydroxides formed decreases due to the growth of oxides at ca. 0.5 – 0.6 V vs SHE, as it was shown in section 5.4.

Due to problems with the use of CO stripping with TiN and TiB_2 as described below, the equivalent experiment with LaB_6 was not conducted.

The results above (Figure 5.18) already indicated that CO stripping may not work for this system, since consecutive cycles will measure lower oxidation current. To confirm this CO stripping experiments were conducted on TiN and TiB_2 with Pt deposited on it and the results are shown in Figure 5.19 below.

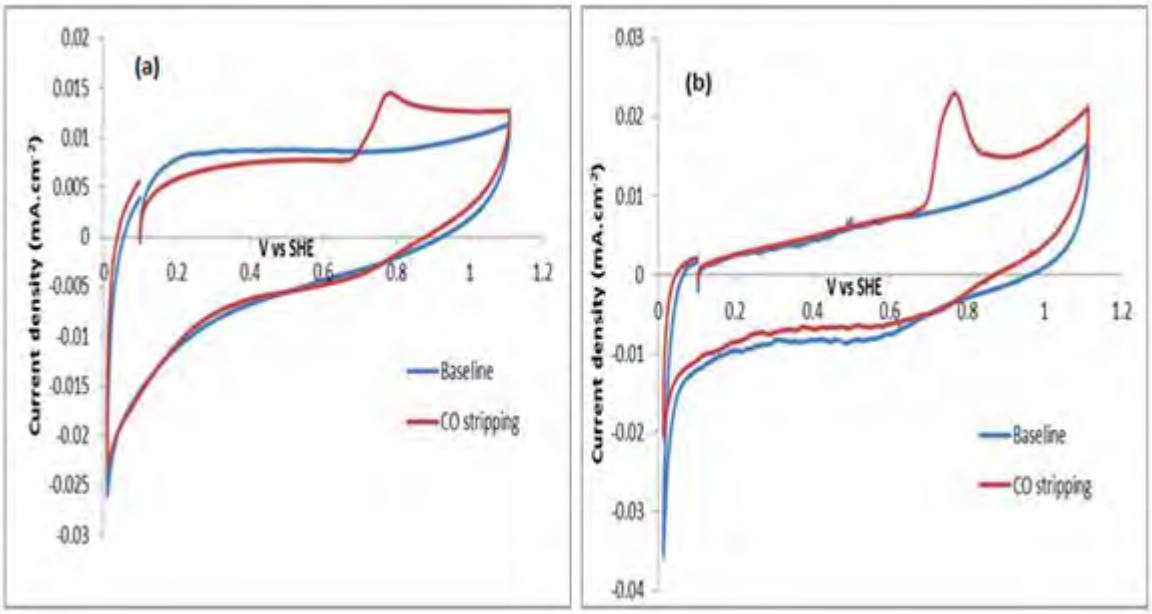

Figure 5.19 CO stripping CV for (a) 1.68 v/v % Pt/TiN and (b) 1.68 v/v% Pt/TiB_2

As anticipated, the oxidation current at 1 V vs SHE dropped significatly from the first cycle (CO stripping) to the baseline current. Therefore, the ECSA cannot be measured via CO stripping technique either; as oxidation currents above 1 V vs SHE will have contributions towards measured ECSA. The potential upper limit was then lowered to 0.98 V vs SHE, but the measured ECSA (98 m^2/g) is higher than the theoretical ECSA for 3.84 nm Pt/TiB_2 (72.65 $m^2.g^{-1}$). This shows that there were TiB_2 current contributions towards the measured value.

Similar results were obtained by Binninger et al. (2014) in a the study of Pt/$Ir_{0.8}Ti_{0.2}O_2$. Therefore, Binninger et al. (2014) developed a novel technique (CO baseline correction) to determine the ECSA on inorganic supports. This method subtracted support material current contributions. In this reasearch project, the applicability of this method was first evaluated using 1.68 v/v% (20 wt%)Pt/C. The results are shown in Fig 5.20, and for clarity the graphs were only plotted for the region of interest (i.e. up to 0.6 V vs SHE) and not for the whole range recorded.

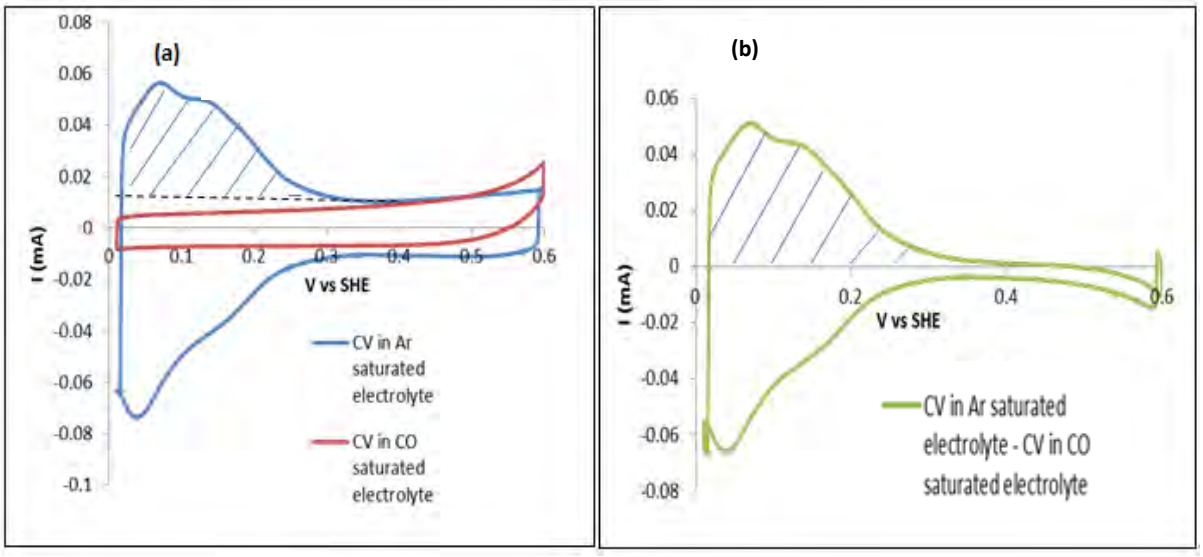

Figure 5.20 CV profile of 20 wt% Pt/C (1.68 v/v%)(a) before correction (b) after correction

As shown in Fig 5.20, the CV obtained in CO does not show any activity in H_{ads}/H_{des} region, since all active sites are blocked with CO. The current measured is purely from the support material. The CV data measured in CO was subtracted from CV data measured in Ar and the results are shown in Fig 5.20 (b). From both graphs it could be seen that the classical method of extrapolating double layer as the baseline is less accurate. The ECSA measured is underestimated. ECSA from the novel 'CO baseline correction' is 68.85 $m^2.g^{-1}$ and from the standard method is 65.48 $m^2.g^{-1}$. This technique was then employed to measure ECSA for the metal nitrides and borides used in this work, and the following results were obtained.

(i) 1.68v/v% Pt/TiN

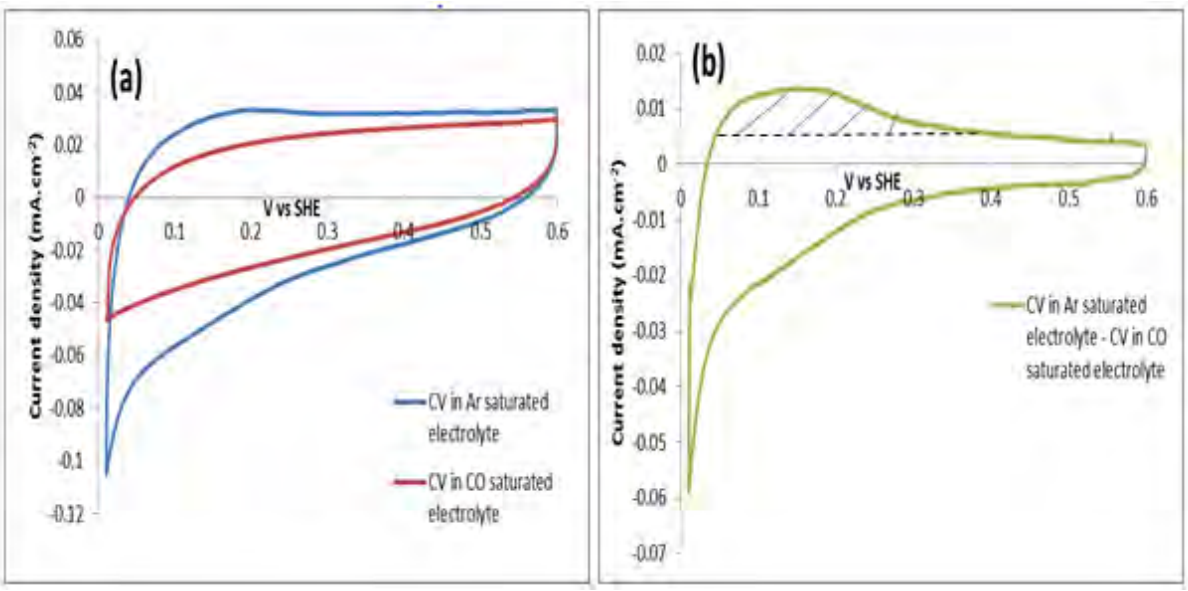

Figure 5.21 (a) CV of 1.68 v/v% Pt/TiN in Ar saturated electrolyte and CO saturated electrolyte (b) CV after correction.

The ECSA measured is 14.6 $m^2.g^{-1}$ and compared to the theoretical ECSA, only 25.2 % Pt is utilised. This low ECSA might be attributed to low e^- conductivity of TiN due to surface oxides. It could be seen from Fig 5.21 (a) that in CO saturated electrolyte, capacitive currents are lower in the H_{ads} region than in double layer region, which is attributed to Pt active sites being covered by CO. Therefore, after correction the double layer region is extrapolated as shown in Fig 5.21 (b), to integrate the charge associated with H_{ads}.

(ii) 1.68 v/v% Pt/TiB_2

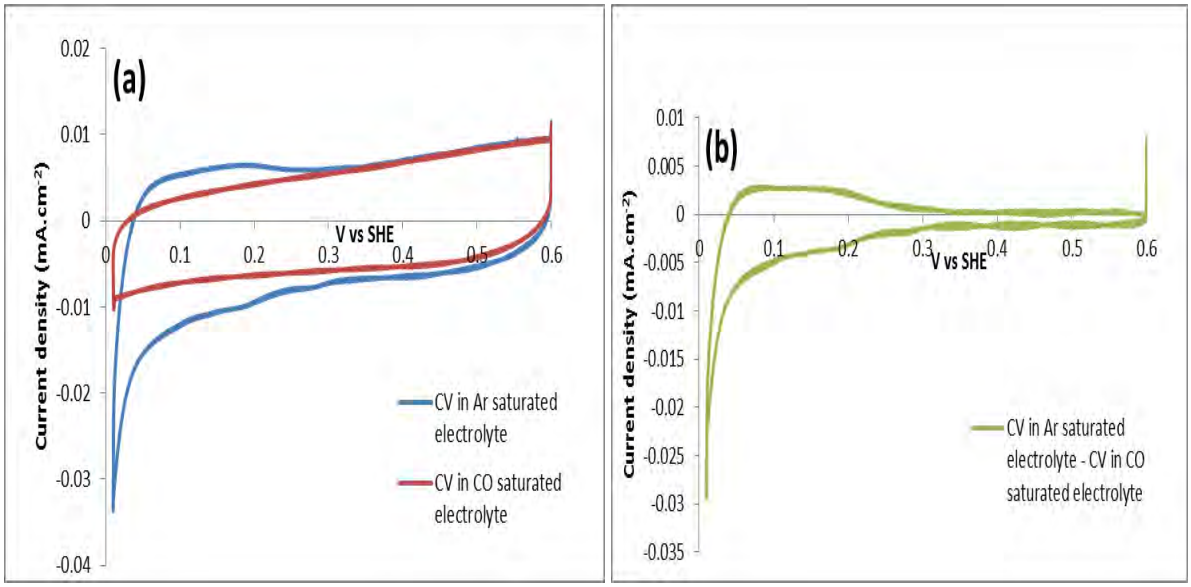

Figure 5.22 (a) CV of 1.68 v/v% Pt/TiB_2 in Ar saturated electrolyte and CO saturated electrolyte (b) CV after correction

For Pt/TiB_2 the calculated ECSA is only 2.61 $m^2.g^{-1}$, which is only 3.6 % of the theoretical ECSA of 72.65 $m^2.g^{-1}$. As for TiN, this result seems to suggest conductivity problems either in the material or in the thin film electrode.

(iii) 1.68 v/v% Pt/LaB_6

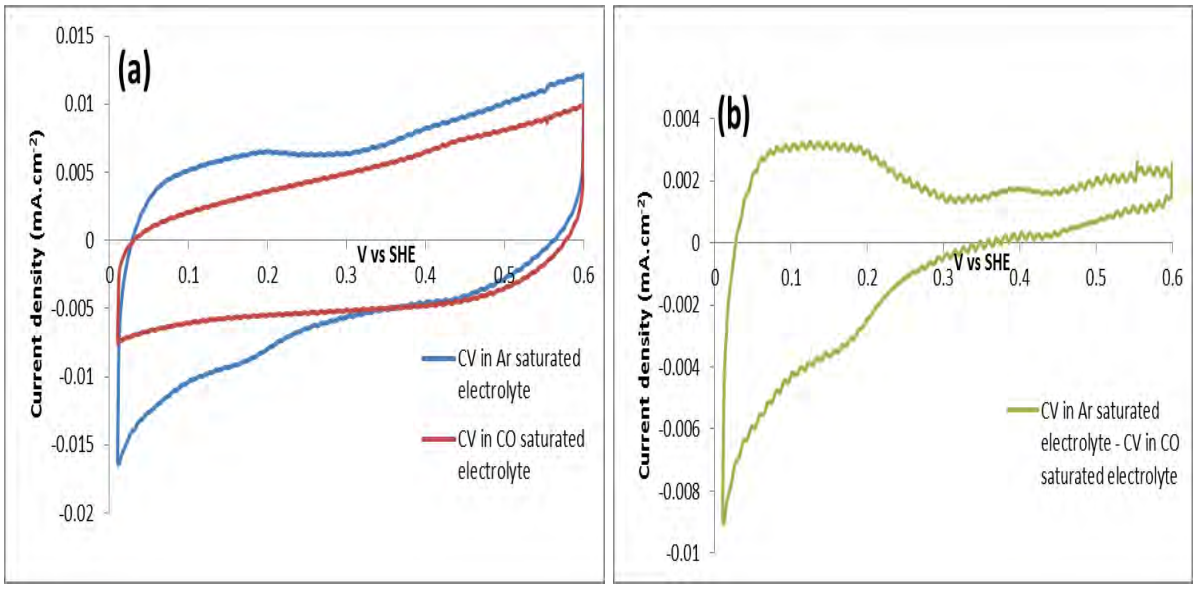

Figure 5.23 (a) CV of 1.68 v/v% Pt/LaB_6 in Ar saturated electrolyte and CO saturated electrolyte, and (b) CV after correction

Similarly to Pt/TiN and TiB_2, Pt/LaB_6 gave low ECSA, as shown in Table 5.7. The utilisation of Pt is 4.68%.

As seen from Fig 5.21 - 5.23, metal nitrides and borides have low ECSA compared to Pt/C. In the best case 25% of Pt seems to be utilised. Whereas, Pt/C with same Pt v/v% shows a high Pt utilisation (81.7%). These results strongly suggest that:

(1) Surface oxides on metal nitrides and borides (TiO_2/oxynitride and B_2O_3, respectively), shown in section 5.4, compromise the transfer of electrons generated during HOR from active sites to the external circuit.

(2) Low Pt loading yield low ECSA.

Schwanitz et al., (2012), reported that ECSA increases with Pt loading, however this only holds if the system contains well dispersed and isolated Pt particles. Therefore, a study to test for the influence of loading on ECSA measurements was conducted.

5.5.1.3 The influence of loading on ECSA measurement

In order to gain further insight in the low ECSA values obtained we first evaluated the claims by Schwanitz et al. (2012).From TEM images of Pt/TiN and Pt/TiB_2 it could be seen that Pt nanoparticles are well dispersed and not agglomerated as Pt loading increases. This was confirmed by XRD as Pt crystallite size measured for Pt/TiN did not change across all three loadings (Table 5.2). Therefore the ECSA of a higher Pt loading catalyst (5.04 v/v%) was measured for Pt/TiN, and the following results were obtained:

(i) 5.04 v/v% Pt/TiN

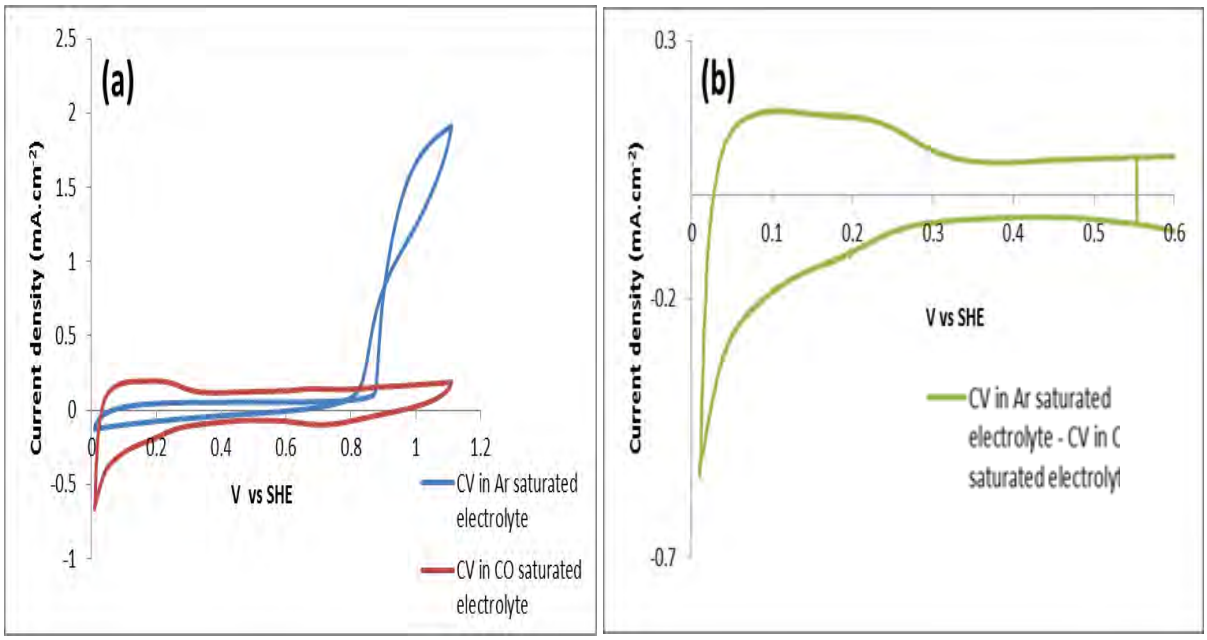

Figure 5.24 (a) CV of 5.04 v/v% Pt/TiN in Ar saturated electrolyte and CO saturated electrolyte, and (b) CV after correction.

Although the calculated ECSA increased to 21.3 $m^2.g^{-1}$ this is still less than half of what one would theoretically expect and therefore not satisfactory. The next step was then to evaluate to what extent the suspected electrical conductivity problem plays a role.

5.5.1.4 Influence of electron conductivity on ECSA measurement

Rather than conducting a CV or CO stripping experiment it was decided to investigate whether surface oxides hinder electron conductivity through RDE studies as ohmic resistances can be very well observed there. The initial experiment was done with Pt/TiN and the results are as follows:

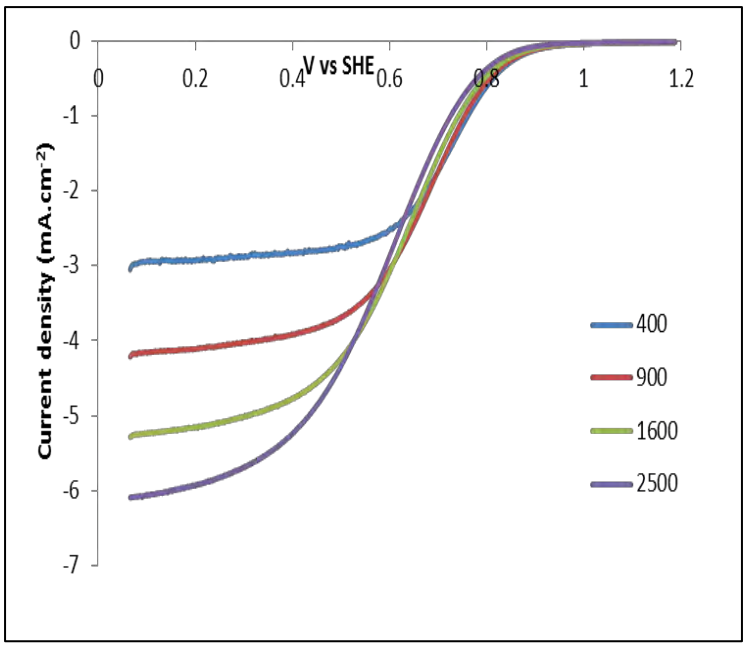

Figure 5.25 LSV curve of 5.04 v/v% Pt/TiN in O_2 saturated 0.1 M $HClO_4$ at 5 $mV.s^{-1}$ (positive sweep)

From Fig 5.25, it can be seen that the system does not follow an ideal behaviour. The onset potential of around 0.8 V vs. SHE is low and severe ohmic losses are observed in the mixed region due to poor electron conductivity of the support material. Moreover, the theoretical limiting current is not reached. To prove that poor e^- conductivity was the driving force for such unideal behaviour. To facilitate with electronic conductivity, 20 wt% acetylene black (AB) was then added into the catalyst ink suspension as it was done in the study by Kakinuma et al. 2012, and the following results were obtained.

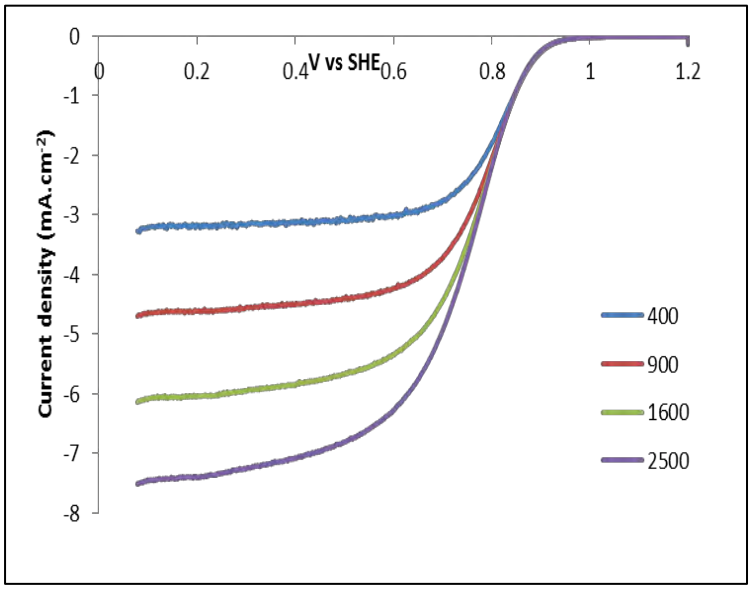

Figure 5.26 LSV curve for 20 wt% AB - 5.04 v/v% Pt/TiN in O_2 saturated 0.1 M $HClO_4$ at 5 $mV.s^{-1}$ (positive sweep)

As can be seen from Fig 5.26, addition of electron conducting AB improves ORR kinetics as can be seen from the shift of the onset potential to values around 0.9 V vs. SHE. Although a full plateau was not obtained, the theoretical limiting current is reached at all rotation speeds. These results clearly indicate that there is significant electrical resistance in the used support materials. This data will be fully analysed later to obtain the kinetic current, intrinsic activity and mass activity of the catalyst.

Since conductivity was now established as one of the challenges surface area could now be determined using a thin film electrode containing AB. Figure 5.27 shows the cyclic voltammetry profiles obtained. It needs to be noted that the ECSA is still measured by the novel CO baseline correction method.

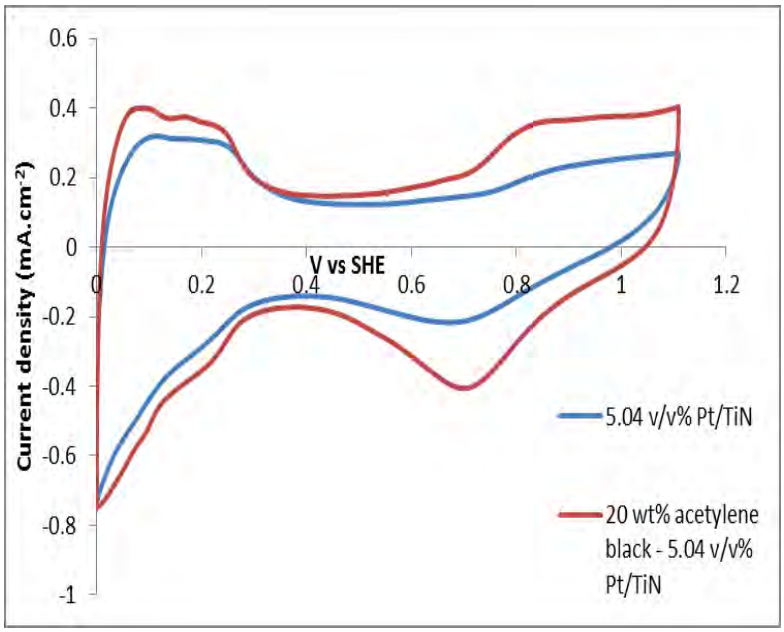

Figure 5.27 CV profile of 5.04 v/v% Pt/TiN before and after addition of AB

After addition of (AB) the ECSA increased from 21.3 $m^2.g^{-1}$ to 29.7$m^2.g^{-1}$, Pt utilisation increased to 57.5 %.

5.5.1.4 Summary on establishment of electrochemical characterisation methodology

It has been shown that low loading (1.68 v/v%) and poor electron conductivity are major contributors towards low measured ECSA. When Pt loading is tripled, Pt utilisation increased significantly. Moreover, addition of AB further increased measured ECSA. Due to time constraints addition of AB was not optimised and it is beyond the scope of this research project; however it is believed that further improvement is possible.

Because of the results obtained, all further CV and RDE measurements were performed on catalysts with and without AB and compared, results obtained are presented in the next section (5.4.2).

5.4.2 ECSA and activity for Pt supported on metal nitride and metal boride supports

As stated from the previous section, going forward AB was added to catalysts to improve electron conductivity. The CVs and LSVs obtained from both catalysts (with and without AB) are presented below for Pt/TiN, Pt/TiB_2 and Pt/LaB_6, with 5.04 v/v% Pt loading.

5.4.2.1 Catalysts with 5.04 v/v% platinum loading

(i) 5.04 v/v% Pt/TiN

See Figures 5.24. 5.25 and 5.26.

(ii) 5.04 v/v% Pt/TiB_2

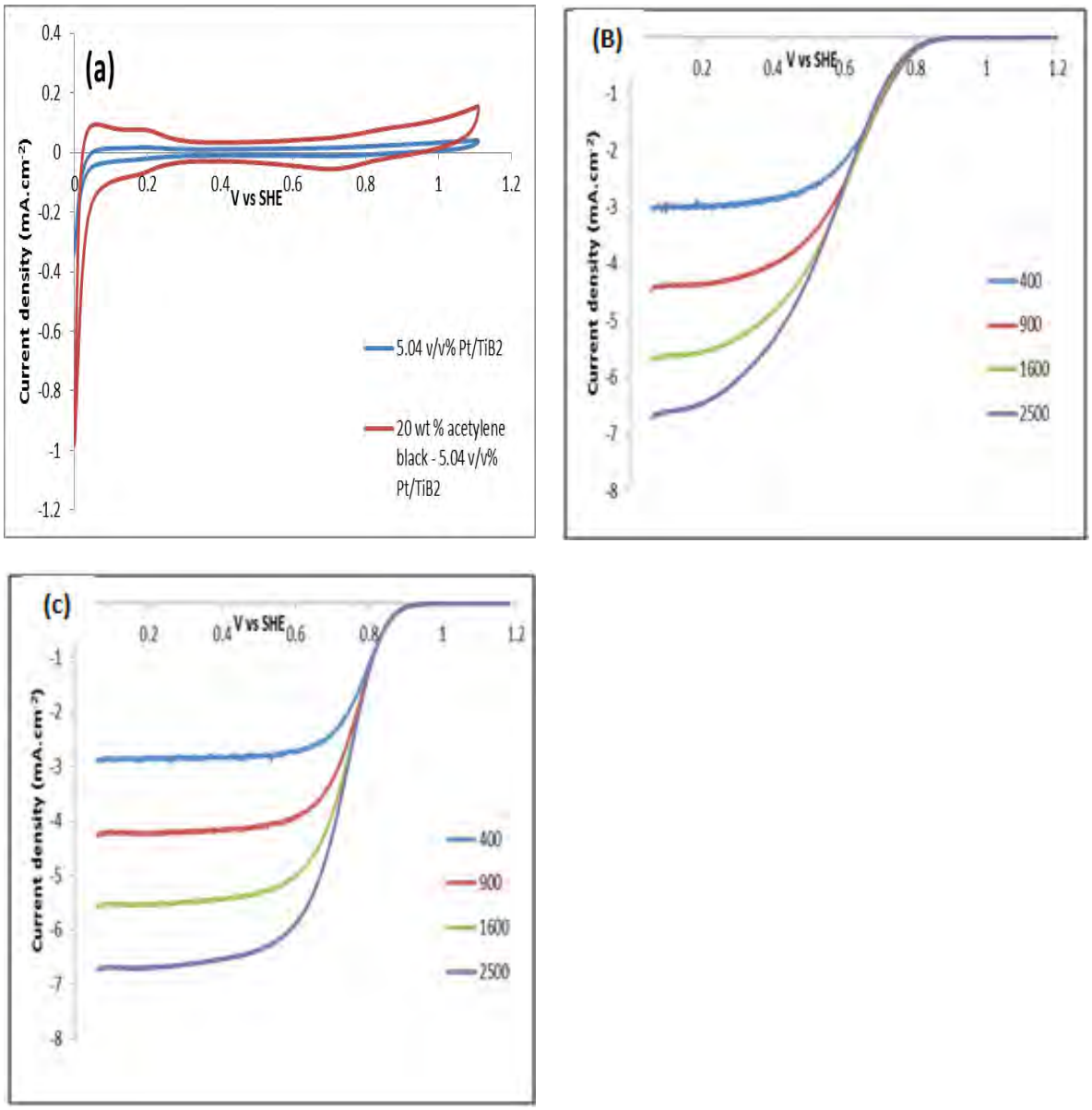

Figure 5.28 (a) CV of 5.04 v/v% Pt/TiB_2 before and after addition of AB (b and C) LSV curve before addition of AB and after, respectively.

Similarly to Pt/TiN, Pt/TiB_2 shows ohmic losses in the mixed region and theoretical limiting currents are not reached at all rotation speeds. However, after addition of AB the measured ECSA increased significantly from 2.4 to 11.9 $m^2.g^{-1}$. However, Pt utilisation is still as low as 18.4 %. In addition, a major improvement is observed on the kinetic region; however the onset potential is still lower than expected. Limiting currents do not entirely reach the theoretical levels however a clearly developed plateau region is visible. A possible explanation for this might be the formation of peroxides which will be discussed in a later section.

(iii) 5.04 v/v% Pt/LaB_6

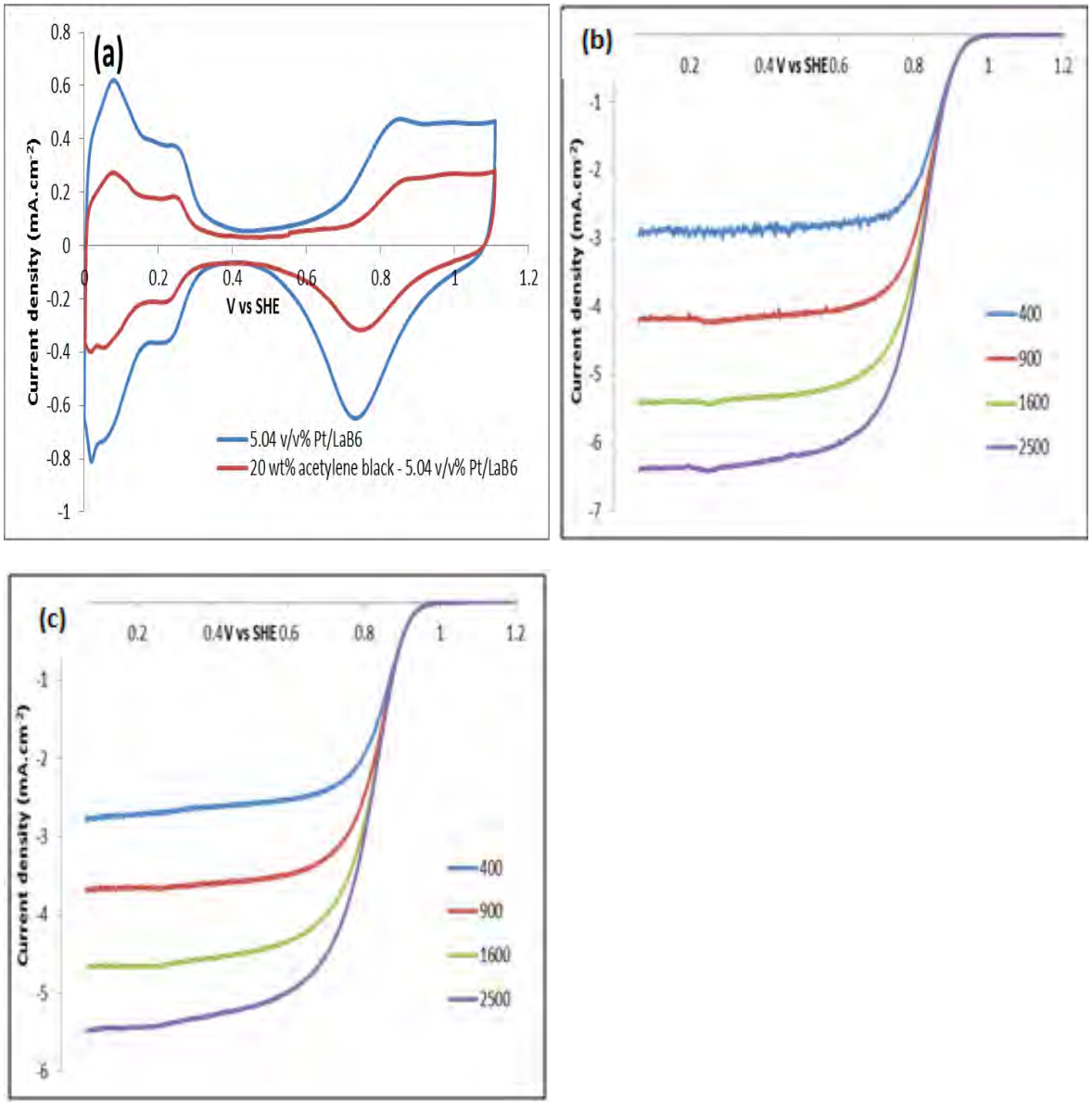

Figure 5.29 (a) CV of 5.04 v/v% Pt/LaB_6 before and after addition of AB (b and c) LSV curve before addition of AB and after, respectively.

On the contrary, Pt/LaB_6 gave high ECSA (30.8 $m^2.g^{-1}$) and does not show major ohmic losses in the kinetic region compared to Pt/TiB_2 and Pt/TiN. Moreover, the system does reach the theoretical limiting currents, without addition of AB. However, measured limiting currents are less than theoretical limiting currents at various rotation speeds. As mentioned previously, this might be an indication of the formation of peroxides (which will be investigated in the next section). Surprisingly, after addition of AB, ECSA decreased by a factor of 1.7. Literature has reported that promoted peroxide formation occurs on this material. However AB did not change the kinetic region. These results suggest that Pt/LaB_6 is very conductive on its own.

5.4.2.2 Catalysts with 3.36 v/v% platinum loading

3.36 v/v% Pt on metal nitrides and borides catalysts were electrochemically characterised as well. Based on results reported above, AB was only added to Pt/TiN and Pt/TiB_2 to provide an improved electron pathway within the catalysts layer, and the results are as following,

(i) 3.36 v/v% Pt/TiN

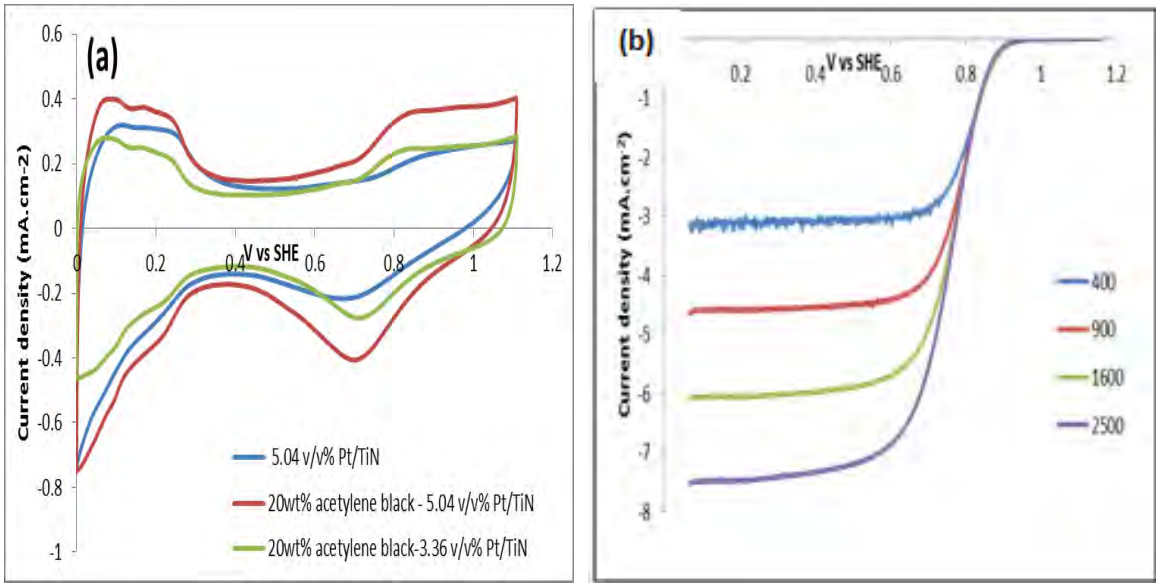

Figure 5.30 (a) CV of 3.36 v/v% Pt/TiN plotted with previous CV profiles of Pt/TiB_2, and (b) LSV of 3.36 v/v% Pt/TiN

As shown in Fig. 5.30, 3.36 v/v% Pt/TiN, showed similar ORR kinetics to 5.04 v/v% Pt/TiN and theroretical limiting currents were reached, this seems to suggest that very little peroxides are formed. The ECSA measured is similar to the one of 5.04 v/v% Pt/TiN, (see also Table 5.7).

(ii) 3.36 v/v% Pt/TiB_2

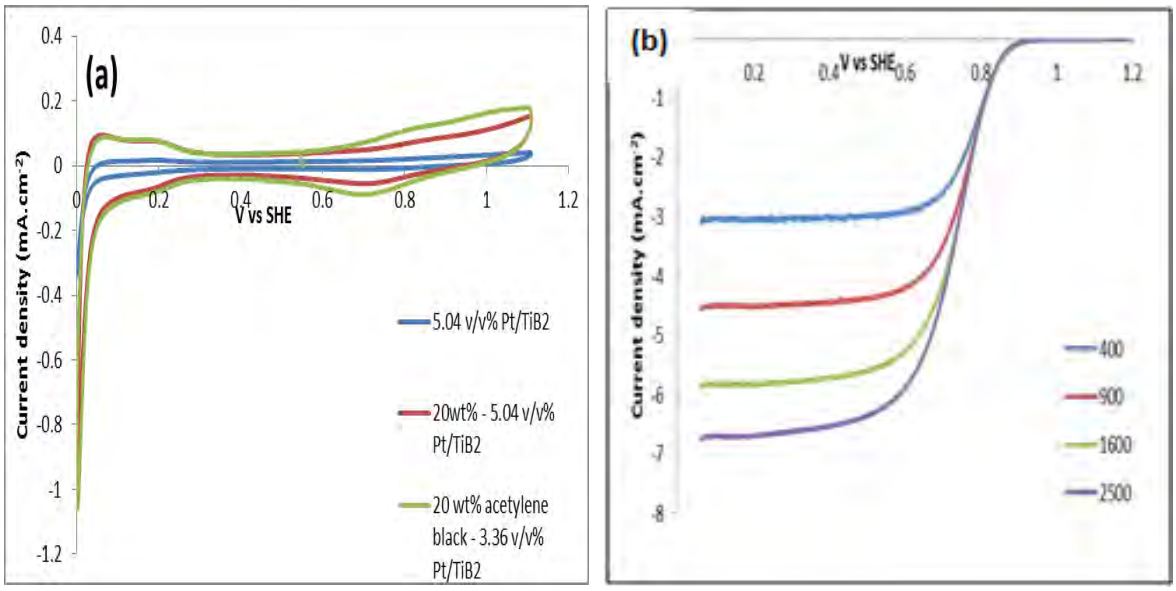

Figure 5.31 (a) CV of 3.36 v/v% Pt/TiB_2 plotted with previous CV profiles of Pt/TiB_2, and (b) LSV of 3.36 v/v% Pt/TiB_2.

The CV profile 3.36 v/v% Pt/TiB_2 gave almost the same ECSA as of 5.04 v/v%, due to same Pt particle size. Theoretical limiting currents are not reached, but have slightly improved compared to 5.04 v/v%.

(iii) 3.36 v/v% Pt/LaB_6

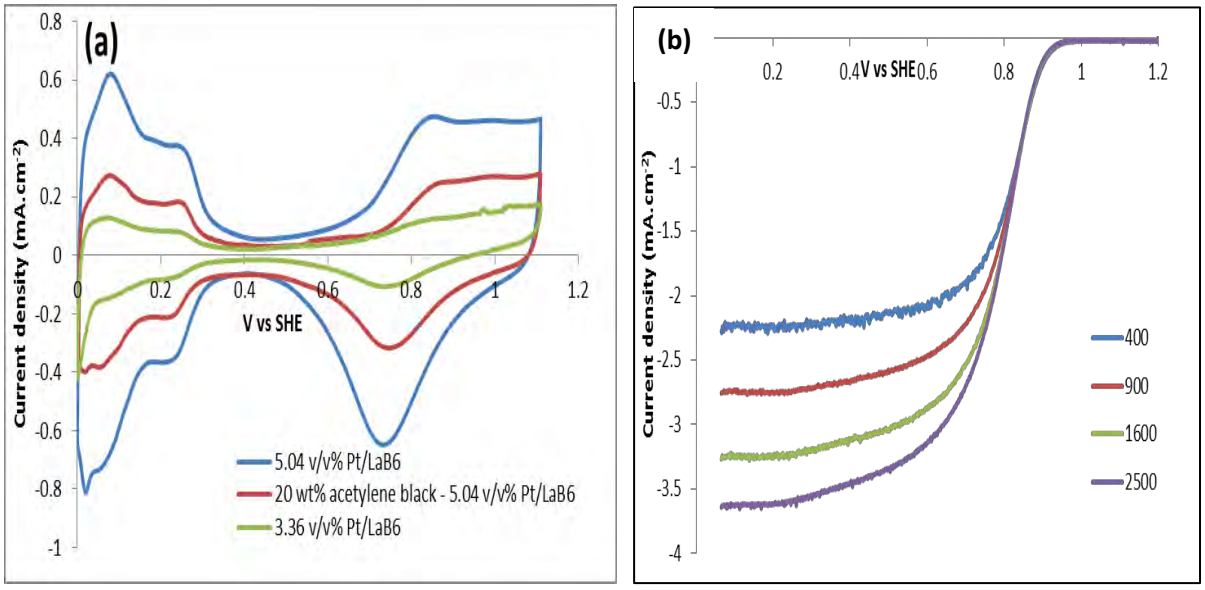

Figure 5.32 (a) CV of 3.36 v/v% Pt/LaB_6 plotted with previous CV profiles of Pt/LaB_6 (b) LSV of 3.36 v/v% Pt/LaB_6

3.36 v/v% Pt/LaB_6 measure a very small ECSA as shown in Table 5.7. The LSV curve shows a large deviation from the theoretical limiting current. The exact reason could not be

determined at this stage of this work, but it seems that at this particular loading a lot of peroxides are formed

5.4.3 Overall analysis of all ECSA and activity data

All the data generated above from 1.68, 3.36, and 5.04 v/v% Pt/TiN, Pt/TiB_2 and Pt/LaB_6, with and without addition of AB, is analysed to determine the ECSA and kinetics. The results are then compared to commercial catalysts (Pt/C) of equivalent v/v% Pt loading. The benchmarks were tested in similar test conditions as the catalyst of study and the following results were obtained.

5.4.3.1 Pt/C benchmark

In order to be able to do an in depth analysis, electrochemical characterisation of known Pt/C catalysts with the same platinum loading were performed to compile a set of benchmark data. The results obtained are shown in Fig 5.33, 5.34 and 5.35 and are discussed in section 5.5.3.2.

(i) 1.68 v/v% Pt/C

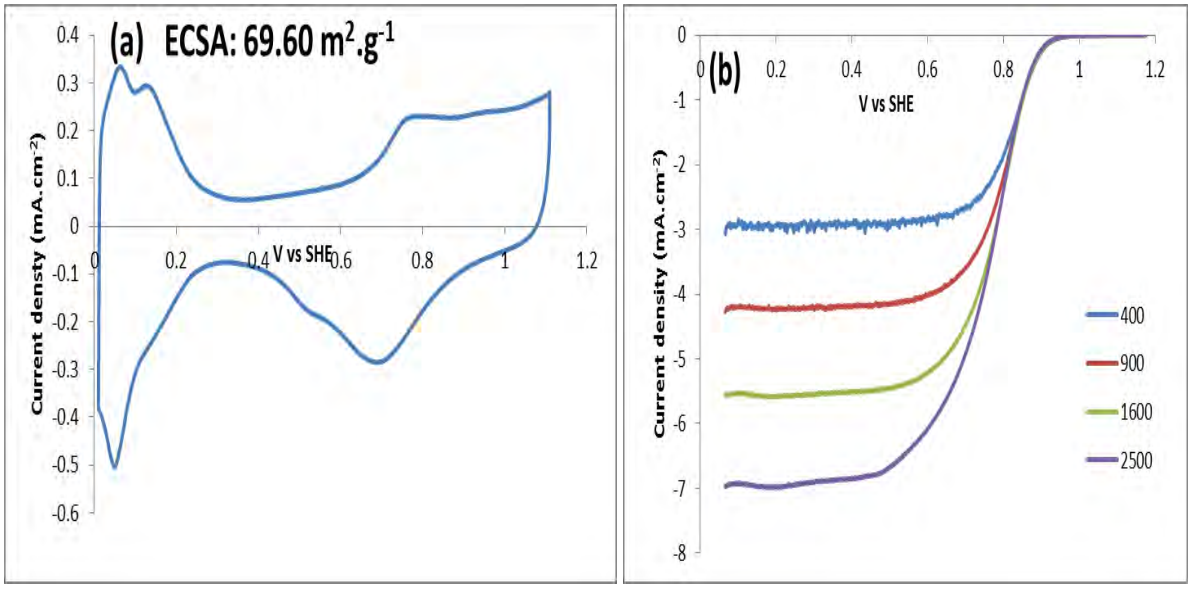

Figure 5.33 (a) CV for 1.68 v/v% Pt/C, and (b) LSV curve thereof**.**

(ii) 3.36 v/v% Pt/C

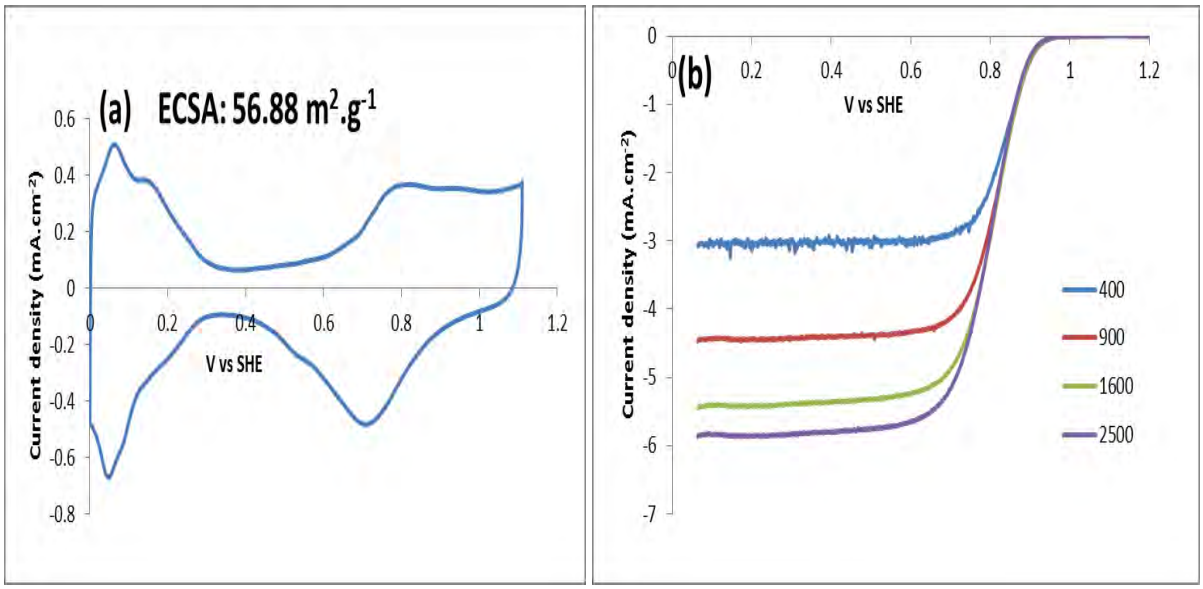

Figure 5.34 (a) CV for 3.36 v/v% Pt/C, and (b) LSV curve thereof.

(iii) 5.04 v/v% Pt/C

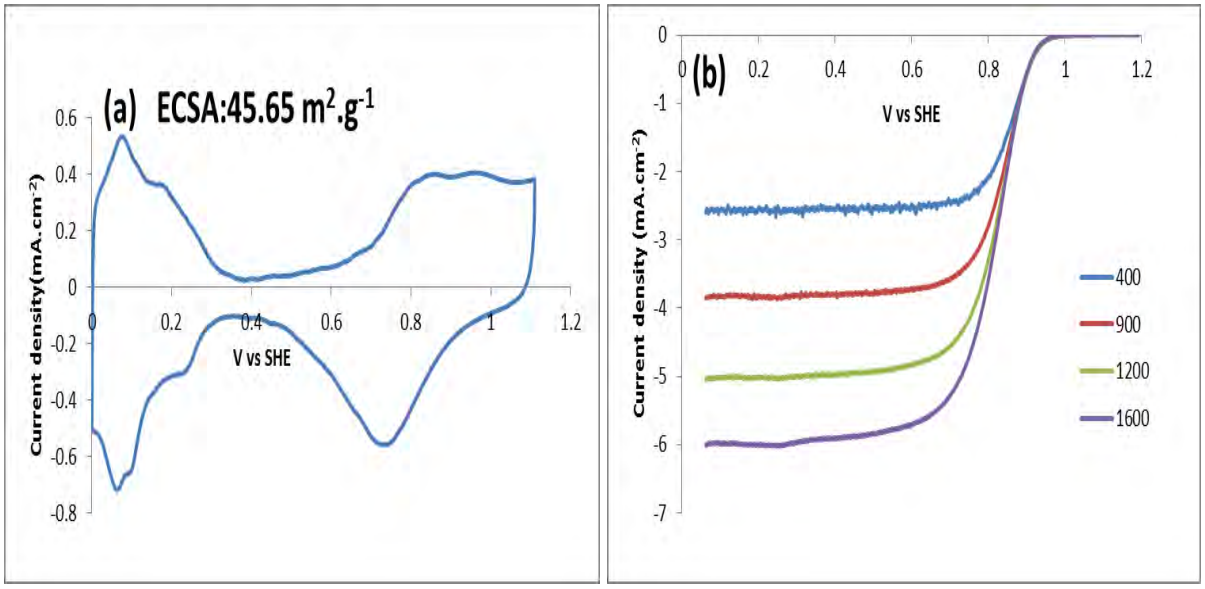

Figure 5.35 (a) CV for 5.04 v/v% Pt/C, and (b) LSV curve thereof.

5.4.3.2 ECSA analysis

All electrochemical results obtained for Pt/C, Pt/TiN, Pt/TiB_2, Pt/LaB_6 are shown in the table below.

Table 5.7 Pt utilisation of ECSA measured on Pt/C, Pt/TiN, Pt/TiB_2 and Pt/LaB_6, with and without AB.

catalyst	1.68 v/v%			3.36 v/v%			5.04 v/v%		
	Theoretical ($m^2.g^{-1}$)	Exp. ($m^2.g^{-1}$)	Pt utilisation (%)	Theoretical ($m^2.g^{-1}$)	Exp. ($m^2.g^{-1}$)	Pt utilisation (%)	Theoretical ($m^2.g^{-1}$)	Exp. ($m^2.g^{-1}$)	Pt utilisation (%)
Pt/C	85.2	69.6	81.7	73.8	56.9	77.0	71.2	45.7	64.1
Pt/TiN	58.0	14.6	25.2	57.0			58.0	21.3	36.7
Pt/TiN + AB					30.5	52.5		29.7	51.2
Pt/TiB_2	72.7	2.61	3.59	73.0			64.4	2.4	3.7
Pt/TiB_2 + AB					13.6	18.6		11.9	18.7
Pt/LaB_6	61.9	2.90	4.68	58.2	10.8	18.6	57.4	30.8	53.6
Pt/LaB_6 + AB								18.2	31.5

From the table above, Pt/C ECSA decreases as metal loading increases. At high loadings Pt nanoparticles tend to agglomerate and form bigger particles, resulting in a loss of surface area. These results do not agree with an ideal model by Schwanitz et al. (2012) described above. However, Pt/LaB_6 does follow the model and ECSA increases with increasing Pt loading. However this seems to be related to the increase in metal utilisation (from 4.68% to 18.6 % and 53.6 %) rather than an increase in actual physical surface area. For Pt/TiN and Pt/TiB_2 the measured ECSA remains the same, since nanoparticles are in the same size range, with utilisation in the same range as well. Catalysts that showed Pt utilisation higher that 50 % were further characterised to determine ORR kinetics. Hence, only 5.04 v/v% Pt/LaB_6, Pt/TiN + AB and 3.36 v/v% Pt/TiN + AB were taken further for analysis. Pt/TiB_2 showed least overall ECSA compared to other catalysts

5.4.3.3 ORR kinetics analysis

The data obtained from RDE above was used to calculate kinetic current, mass activity and intrinsic activity at 1600 rpm for catalysts that showed close to ideal behaviour under reduction of O_2 and Pt utilisation above 50 %. Table 5.8 shows intrinsic activity and mass activity of electrocatalysts at 0.9 V and 1600 rpm.

Table 5.8 Measured limiting current at 1600 rpm, calculated intrinsic and mass activity at 0.9 V.

catalyst	Limiting current		i ($mA.cm^{-2}$)			i_k ($mA.cm^{-2}$)			Intrinsic activity at 0.9 V	Mass activity at 0.9 V
	Exp.i_d ($mA.cm^{-2}$)	Dev i. (%)	0.7 V	0.8 V	0.9 V	0.7 V	0.8 V	0.9 V	($mA.cm^{-2}$)	($mA.mg^{-1}$)
3.36 v/v% Pt/C	-5.39	10.8	-4.55	-3.27	-0.560	29.1	8.31	0.625	0.035	20.0
5.04 v/v% Pt/C	-5.01	17.0	-4.55	-3.27	-0.560	49.6	9.41	0.630	0.029	13.4
3.36 v/v% Pt/TiN + AB	-6.05	0.331	-5.30	-1.88	-0.178	42.6	2.73	0.183	0.024	7.2
5.04 v/v% Pt/TiN + AB	-6.04	0.331	-4.43	-2.16	-0.138	16.5	3.36	0.141	0.013	3.8
5.04 v/v% Pt/LaB_6	-5.42	10.3	-4.82	-3.49	-0.611	43.5	9.80	0.688	0.026	7.9

From Table 5.8 it can be seen that the benchmark (Pt/C) showed better performance than Pt supported on metal nitrides and borides. This is attributed to low Pt utilisation % on metal nitrides and borides. The Pt/C catalyst has a small Pt particle size (high ECSA) and high Pt utilisation compared to Pt on metal nitrides and borides. In addition, only Pt/TiN with acetylene black added (TiN + AB) did reach theoretical limiting current. The low Pt utilisation obtained combined with the low limiting current suggest that the lower performance is due to ohmic losses, i.e. low conductivity. There is also a possibility that Pt nanoparticles are encapsulated by the oxides formed on the surface, as it was observed by Kakinuma et al. (2012) on Pt/TiN + AB catalyst, however, this has not been confirmed. When Pt particles are encapsulated, they are not electrochemically active as they are not accessible to reactants.

RRDE studies were performed to determine the amount of peroxides formed by 5.04 v/v% Pt/LaB_6 and 3.36 v/v% Pt/TiN + AB.

5.4.4 RRDE studies

The collection efficiency of the ring was measured before commencing RRDE measurements for Pt/LaB_6 and 3.36 v/v% Pt/TiN + AB.

5.4.4.1 Collection efficiency

Table 5.9 Collection efficiency measurements in Ar saturated 0.1 M $HClO_4$, scanning the disk from 0.01 -1.2 V vs SHE at 5 mv.s^{-1}, while the ring was held at 1.2 V.

Rotation speed (rpm)	i_{disk}	i_{ring}	$N = -\frac{i_{ring}}{i_{disk}}$ %
400	- 0.612	0.094	15.3
900	- 0.813	0.126	15.5
1600	- 1.15	0.180	15.6
2400	- 1.30	0.201	15.6

The collection efficiency of the ring is 15.5 %, and it is independent of rotation speeds. N measured is similar across all four rotation speeds. These results are in line with that of Paulus et al. (2001).

5.5.4.2 RRDE measurements of 5.04 v/v% Pt/LaB_6 and 3.36 Pt/TiN+AB

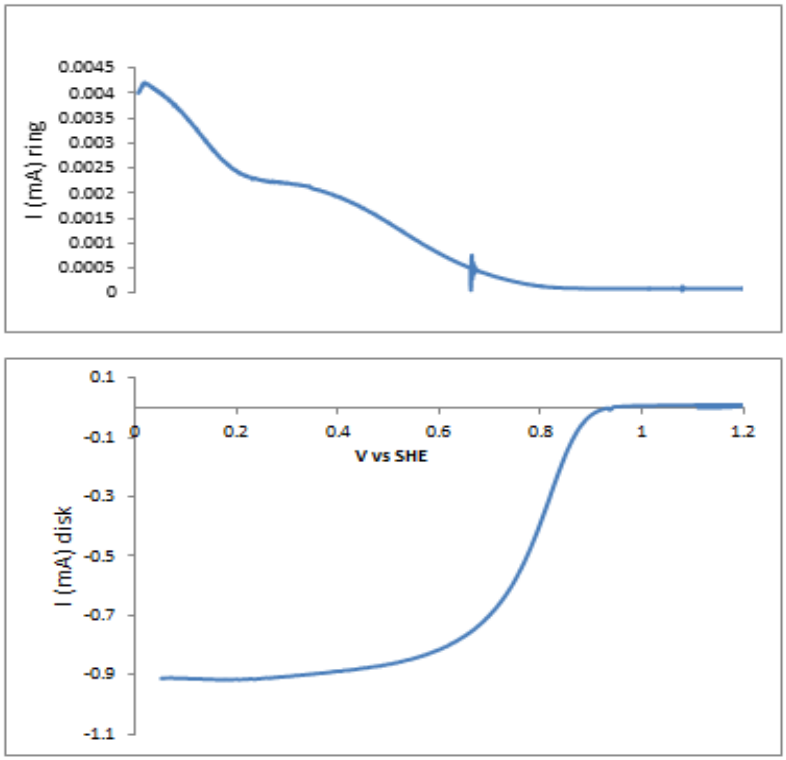

Figure 5.36 RRDE data for Pt/LaB_6 (ring held at 1.2 V, 5 mV.s^{-1}, 0.01 - 1.2 V vs SHE, O_2 saturated 0.1 M $HClO_4$, room temperature)

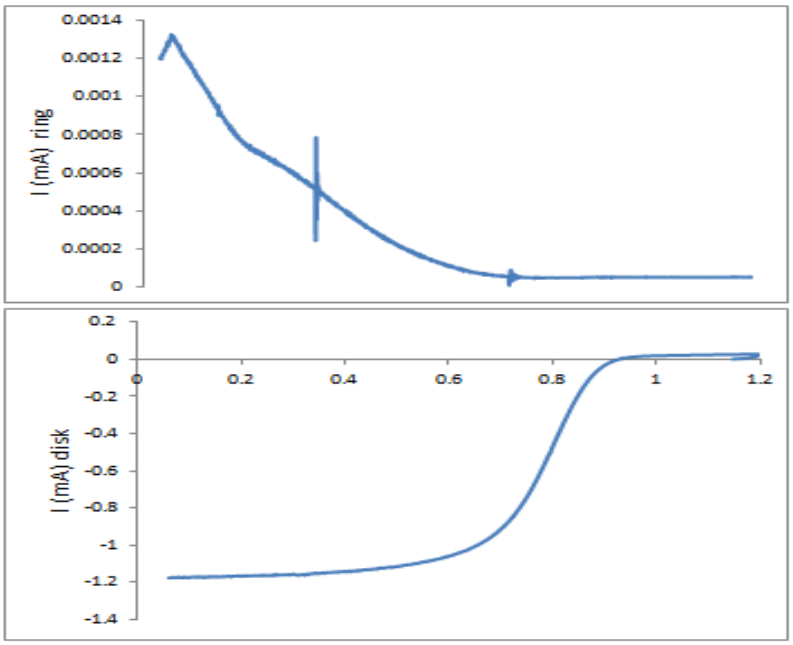

Figure 5.37 RRDE data for Pt/TiN + AB (ring held at 1.2 V, 5 $mV.s^{-1}$, 0.01- 1.2 V vs SHE, O_2 saturated 0.1 M $HClO_4$, room temperature)

As seen in Fig 5.36 and Fig 5.37, hydrogen peroxide formation starts below 0.8 V vs SHE. Pt/LaB_6 does not reach the theoretical limiting current. This is due to formation of hydrogen peroxide below 0.8 V vs SHE, as shown in the ring profile. Pt/TiN + AB does reach the theoretical limiting current, however, peroxides are still generated. The number of electrons for O_2 reduction was calculated to determine if the reaction proceeds via a $2e^-$ or $4e^-$ pathway and the results are presented below in Table 5.10.

Table 5.10 Calculated number of electrons and amount of peroxides formed per O_2 molecule

Catalyst	$n = \frac{4\, i_{Disk}}{i_{disk} + \frac{i_{ring}}{N}}$	$X_{H_2O_2} = \frac{\frac{2\, i_{Disk}}{N}}{i_{disk} + \frac{i_{ring}}{N}}$
5.04 v/v% Pt/LaB_6	3.88	12.5
3.36 v/v% Pt/TiN + 20 wt% AB	3.97	12.8

From table 5.9 it could be seen that for Pt/TiN + AB the calculated number of electrons transferred is very close to 4, indicating that this is an efficient catalyst for the ORR reaction due to the fact that little peroxide is produced and ORR predominantly proceeds via the following reaction:

$O_2 + 4\ H^+ + 4\ e^- \rightarrow H_2O$

For Pt/LaB_6 this value is further away from 4 indicating a higher loss in peroxide formation on this material. Therefore, ORR proceeds via two mechanisms:

Major reaction: $O_2 + 4\ H^+ + 4\ e^- \rightarrow H_2O$

Minor reaction: $O_2 + 2\ H^+ + 2\ e^- \rightarrow H_2O_2$

5.5 Accelerated durability test (ADT)

The durability test of 5.04 v/v% Pt/LaB_6 and of 3.36 v/v% Pt/C was conducted, since it showed better performance than 3.36 v/v% Pt/TiN + AB. The other reason why Pt/TiN+AB was not tested is due to addition of AB, as it is well known that carbon corrodes under load cycling, as shown in section 5.4. The AB added will eventually corrode and measured ECSA will be not accurate due to resistances. Hence, only 5.04 v/v% Pt/LaB_6 was evaluated. ADT techniques were employed namely, support corrosion and Pt dissolution test, using rectangle wave (1.0 -1.5 V vs SHE) and triangle wave (0.65 - 0.95 V vs SHE), respectively. The following results were obtained:

5.5.1 Support corrosion test (1.0 - 1.5 V vs SHE)

The CVs recorded after cycling number of times between 1.0 and 1.5 V vs SHE are as follows,

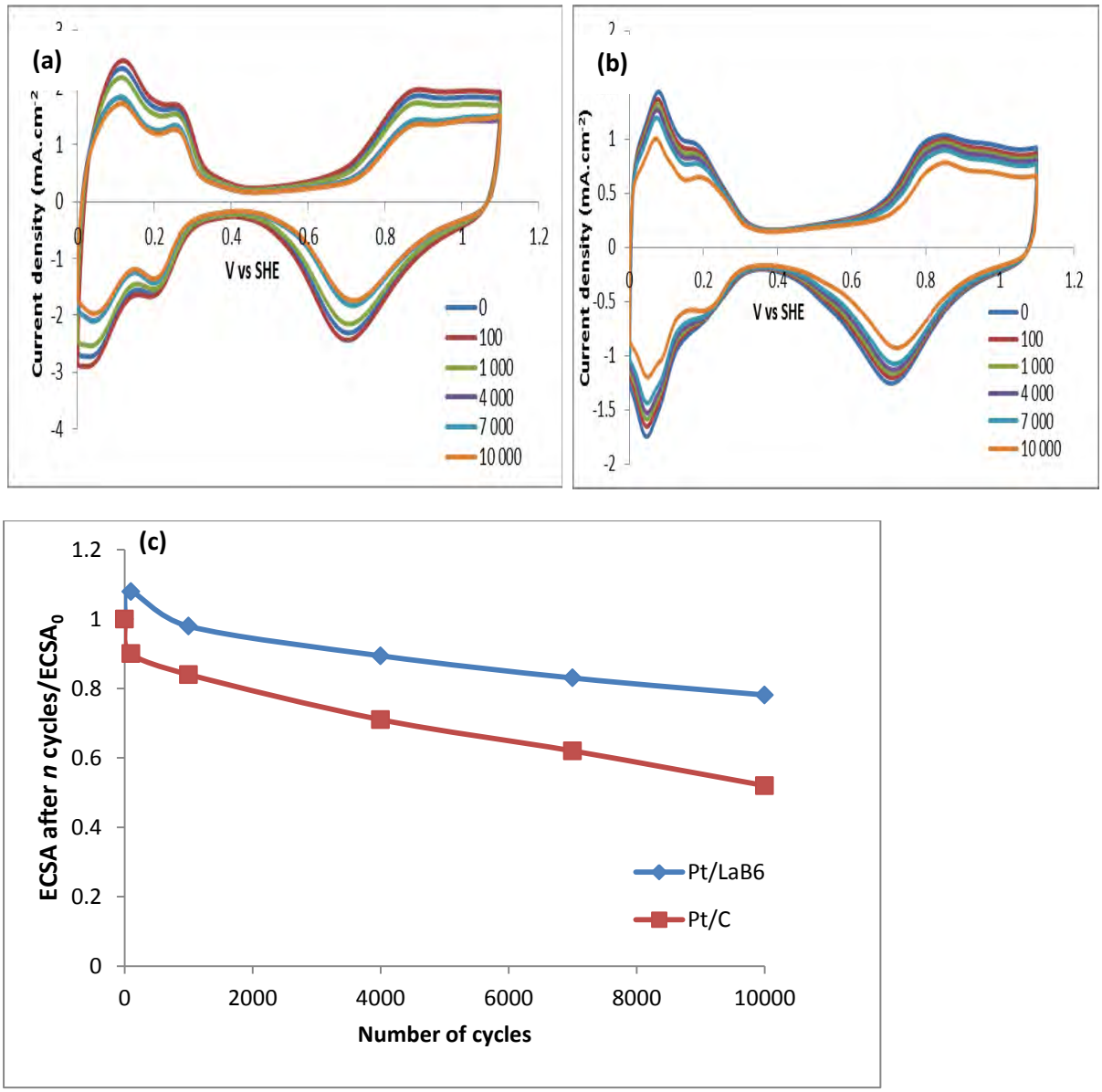

Figure 5.38 (a) and (b) CV profiles of Pt/LaB_6 and Pt/C, respectively, after various number of cycles (1 -1.5 V vs SHE) in 0.1 M $HClO_4$ at room temperature. (c) The rate of support corrosion over number of cycles.

As seen in Figure 5.38 Pt/LaB_6 appears to be more durable than Pt/C. After 10 000 cycles Pt/C has lost about 48 % of ECSA, whereas Pt/LaB_6 had just loss about 18%. These results are in line with finding in section 5.4. Although LaB_6 oxidises under cyclic loading, the rate of oxidation is 25% lower than of Pt/C. This shows that the increased durability observed is related to LaB_6 being more durable than carbon. Pt/LaB_6 furthermore produces higher current densities compared to Pt/C.

5.5.2 Pt dissolution on 5.04 v/v% Pt/LaB_6 and Pt/C

The CVs recorded after cycling number of times between 0.65 and 0.95 V vs SHE are presented below.

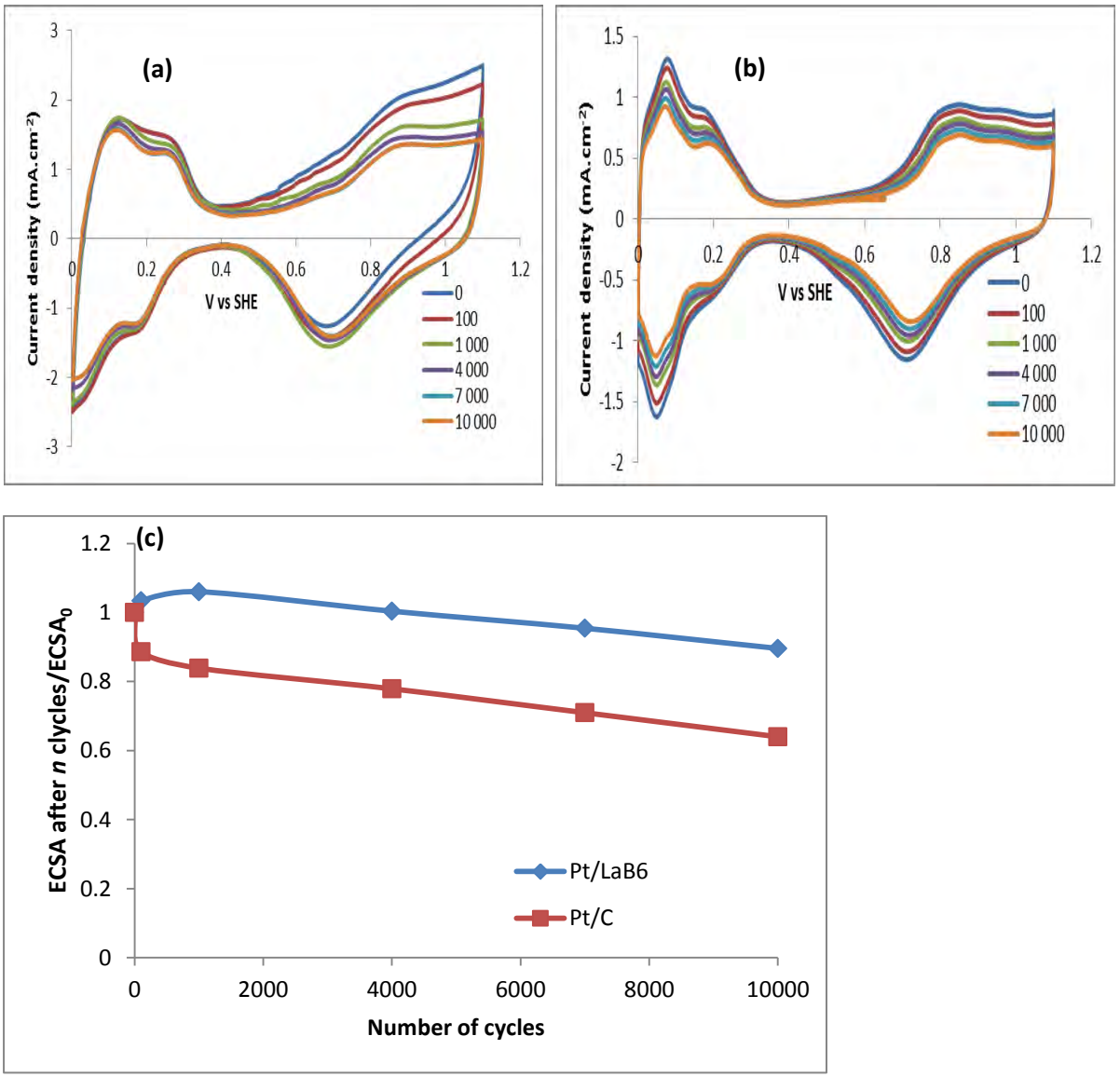

Figure 5.39 (a) and (b) CV profiles of Pt/LaB_6 and Pt/C, respectively, after various number of cycles (0.65 - 0.95 V vs SHE) in 0.1 M $HClO_4$ at room temperature. (c) The rate of Pt dissolution over number of cycles.

As shown above (Fig 5.39), after 10 000 cycles Pt supported on LaB_6 has been reduced by 10 %, while 36 % of the surface area of the Pt/C catalyst has been lost. This could be attributed to a more stable initial Pt particle size. The initial particle size measured by XRD is 3.92 nm for Pt/C and 4.86 nm for Pt/LaB_6 (Table 5.1). Therefore, Pt on LaB_6 is more resistant to Pt dissolution due to larger dimensions as to Pt on carbon. The literature has shown strong correlation between Pt particle size and dissolution rate. In addition to that it cannot be excluded that metal support interactions play a role as well, however this could not be investigated within the scope of this work.

Table 5.11 ICP results for support corrosion and Pt dissolution test

	5.04 v/v% Pt/LaB_6	**5.04 v/v% Pt/C**
1.0 – 1.5 V vs SHE	123 ppb	345 ppb
0.65 -0.95 V vs SHE	-	329 ppb

ICP results correlate with findings from Fig 5.38 (c) and 5.39 (c). Pt/LaB_6 showed better stability than Pt/C as only 123 ppb Pt was measured in the electrolyte. For Pt dissolution, Pt concentration could be below the detection limit or Pt^{2+} ions were reabsorbed by Pt particle (Ostwald ripening). For Pt/C the concentration of Pt is almost the same under both tests.

From the above findings it could be seen that from a durability point of view Pt/LaB_6 can be an alternative to Pt/C.

Chapter 6

6. Conclusions and recommendations

Based on the results obtained on evaluation of metal nitrides and borides as alternative electrocatalyst materials, in terms of physical and electrochemical properties, Pt deposition and activity studies, the following conclusions were drawn.

As it was stated in the literature review that for the material to be considered as an alternative support material it must meet certain requirements such as high BET surface area, have adequate porosity for mass transport and exceptional electrical conductivity and electrochemical stability. Metal nitrides and borides however showed low specific surface area compared to Vulcan XC-72 (carbon) due to differences in particle size and density. Therefore, new synthesis routes must be investigated to increase the surface area of inorganic support materials. This could be done by synthesising these materials in the form of fibres. Although all the support materials, including Vulcan XC-72 showed a similar N_2-adsorption hysteresis loop with wide BJH-pore distribution indicating the presence of both macro- and micro-pores. However, the pore volume of inorganic support materials was much lower than of carbon (Vulcan XC-72). During activity studies, mass transfer limitations were not observed, indicating that these support materials created a decent three phase boundary (TPB) condition, which is essential for PEFC performance, even though they had lower pore volume than carbon. Furthermore, by synthesising inorganic support materials as fibres may significantly increase the pore volume.

In terms of electrochemical stability, metal nitrides were found to be more stable than metal borides. This was attributed to formation of stable surface oxides and oxynitrides when the material is exposed to strong oxidizing conditions, as hypothesised. The presence of oxynitrides and oxides on the surface prevented further oxidation of the bulk material (passivation), and these results were consistent with literature studies. On the other hand, metal borides formed oxides (B_2O_3) which were found to be unstable. Metal borides did not show any mechanism of passivation under oxidising conditions. This can be attributed to boron being more electronegative than Zr and Ti, therefore boron was oxidised. In the case of metal nitrides, nitrogen was easily substituted for oxygen to form oxynitrides and oxides. Even though metal borides are not stable as metal nitrides, their oxidation rate is much lower than that of Vulcan XC-72. The oxidation rate of Vulcan XC-72 (Carbon) was found to be 24 times higher than LaB_6, 18 times higher than TiB_2 and 13 times higher than ZrB_2. Therefore, metal nitrides and borides are attractive alternatives to Vulcan XC-72, in terms of stability. Further studies are required on surface oxidation of metal borides (similar to the one conducted by Avasarala et al. 2010 & 2011 on metal nitrides, using techniques such as XPS). However the downside is that although these materials are more stable that carbon, due to the formation of surface oxides. It has been demonstrated that these oxides

significantly reduces electrical conductivity of support materials (except for LaB_6), as major ohmic losses were observed on the polarisation curve.

1.68 v/v%, 3.36 v/v%, 5.04 v/v% of Pt which is equivalent to 20, 40 and 60 wt% Pt/C, respectively, was successfully deposited on TiN, TiB_2 and LaB_6 , but not on ZrN and ZrB_2 (due to chemical inertness of the material) using both OMCVD and wet chemical deposition (impregnation) techniques, using chloride-free Pt precursors. The wet chemical deposition resulted in well dispersed Pt particles with narrow size distribution and was considered as the method of choice for Pt deposition on metal nitrides and borides opposed to organo-metallic chemical vapour deposition. Since Pt could not be deposited on Zr- based materials, it is clear that pre-oxidation treatment with acids is required to modify the surface, so that there could be a Pt-support interaction. However, pre-oxidation of materials reduces the electrochemical stability of the material. Furthermore, it must be noted that there is no literature documented on using these Pt deposition techniques (OMVCD and impregnation method) on metal nitrides and borides for fuel cell applications. Thus, this project has demonstrated that there are better alternative methods of depositing Pt on inorganic materials, opposed to conventional polyol technique. Moreover, it was indicated in the literature review that polyol method uses chloride containing Pt precursor which is believed to poison Pt during synthesise, which results in lower ECSA and performance. Since impregnation method uses Cl-free precursors, it is a better alternative to polyol method.

During electrochemical characterisation of Pt/TiN, Pt/TiB_2 and Pt/LaB_6, the voltammograms obtained showed significant differences compared to Pt/C. Therefore, there was a need to develop reliable electrochemical techniques for such catalysts. The novel CO baseline correction method developed for Pt/$Ir_{0.8}Ti_{0.2}O_2$ by Binninger et al. (2014) was applied on the study of Pt/TiN, Pt/TiB_2 and Pt/LaB_6. The CO baseline method gave more accurate ECSA than the 'standard' CO stripping and $H_{ads/des}$ integration, by extrapolation of the double layer as the baseline. This project has extended on the work done by Binninger et al. (2014), as it was demonstrated that CO-baseline technique could be applied on any catalysts. The method is reliable and gives accurate results.

1.68 v/v% Pt/TiN, Pt/TiB_2 and Pt/LaB_6 resulted in a low ECSA and poor performance due low Pt loading and poor electron conductivity. The electron conductivity of metal nitrides and borides was lost due to formation of surface oxides in an acidic medium. Therefore the loading was increased to 5.04 v/v% Pt and electron conducting acetylene black (AB) was added to overcome electron conductivity problems, which resulted in higher ECSA and improved ORR kinetics. The interesting results were that LaB_6 did not require addition of AB as it did not show much deviation from the typical LSV curve, and lower ohmic losses. Although the literature has reported that surface oxides formed do not affect the electrolytic activity, however this study shows that oxides compromises electron conductivity, hence the activity of the catalyst. Form these results the only support that has potential as a support is LaB_6, since it did not show severe ohmic losses and gave a

reasonable activity toward ORR without adding AB. Addition of AB on TiN and TiB_2 is not a long term solution for improving the electron conductivity, as it will eventually corrode and Ohmic losses will resurface.

After RDE analysis 5.04 v/v% Pt/LaB_6 and 3.36 v/v% Pt/TiN + AB, showed less mass and intrinsic activity compared to its Pt/C counterpart and this was attributed to low ECSA utilisation (possibly from Pt particles capsulation by surface oxides) RRDE studies showed very minimal amount of peroxide formed by 5.04 v/v% Pt/LaB_6 and 3.36 v/v% Pt/TiN + AB; therefore, a $4e^-$ pathway is favoured for ORR.

In closing, despite the lower performance, 5.04 v/v% Pt/LaB_6 showed exceptional durability compared to Pt/C of the same v/v%. This was attributed to better LaB_6 electrochemical stability and strong metal-support interaction which restricted Pt migration over the support to form Pt agglomerates (sintering). Moreover, Pt dissolution was very minimal compared to Pt/C. Therefore, LaB_6 has a great potential to be used as an alternative electrocatalyst support material. This material still oxidised as Pt/C but at a much lower rate. In addition, there are no literature reports on LaB_6 as an electrocatalyst support material. Therefore, this projected has generated new knowledge by showing the stability and activity of the materials for PEFCs applications.

Going forward, more insight on oxidation behaviour of Pt/TiN, Pt/TiB_2 and Pt/LaB_6 is needed, more specifically the surface species formed and the rate at which the oxidation occurs. Pt/LaB_6 is of particular interest, since this material did not show major ohmic losses compared to other catalysts. This catalyst did not require addition of AB. As a matter of fact addition of AB reduced the activity. The suggested further analyses are el electron conductivity, surface chemistry using XPS depth profiling to determine how thick is the oxidation layer and confirm if it is indeed B_2O_3, since Pt/LaB_6 showed a very different behaviour from other catalysts supported on inorganic materials.

References

Antoine, O. & Durand, R. (2000), "RRDE Study of Oxygen Reduction on Pt Nanoparticles inside Nafion: H_2O_2 Production in PEMFC Cathode Conditions", Journal of applied Electrochemistry, 30(7): 839-844.

Antolini, E. & Gonzalez E.R. (2009), “Ceramic Materials as Supports for Low-Temperature Fuel Cell Catalysts”, Solid State Ionics 180 (9-10): 746-763.

Artyushkova, K., Pylypenko, S.; Dowlapalli M. & Atanassov, P. (2014), “Structure-To-Property Relationships in Fuel Cell Catalyst Supports: Correlation of Surface Chemistry and Morphology with Oxidation Resistance of Carbon Blacks” Journal of Power Sources, 214(1): 303-313.

Asoro M. A.; Kovar, D.; Shao-Horn, Y. Allard, L.F. & Ferreira, P. J. (2010), “Coalescence and Sintering of Pt Nanoparticles: In Situ Observation by Aberration-Corrected HAADF STEM”, Nanotechnolog, 21(1):1-6

Avasarala, B. & Halder, P. (2010) “Electrochemical Oxidation Behaviour of Titanium Based Electrocatalysts under PEM Fuel Cell Conditions”, Electrochimica Acta 55(28): 9024-9034.

Avasarala, B. & Halder, P. (2011), “On the Stability of Tin-Based Electrocatalyst for Fuel Cell Applications”, International Journal of Hydrogen Energy, 369(6): 3965-3974.

Avasarala, B. & Murray, T. (2009) “Titanium Nitride Nanoparticles Based Electrocatalyst for Proton Exchange Membrane Fuel Cells”, Journal of materials Chemistry, 19(13): 1803-1805.

Barbir, F. (2005), "PEM Fuel Cells: Theory and Practice", Elsevier Academic Press

Baturina, O. A.; Aubuchon S.R & Wynne K. J. (2005), “Thermal Stability in Air of Pt/C Catalysts and PEM Fuel Cell Catalyst Layers”, Chemistry of Materials, 18(6): 1498-1504

Bazhanov, D. I.; Knizhnik, A. A; Safonov A. A.; Bagatur’yants, A. A.; STOKER, M.W. & Korkin, A. A. (2005) “Structure and Electronic Properties of Zirconium and Hafnium Nitrides and Oxynitrides”, Journal of Applied Physics 97(4): 044108-044108

Benninger, T.; Fabbr,i E.; Kotz, R. & Schmidt, T.J. (2014), “Determination of the Electrochemically Active Surface Area of Metal-Oxide Supported Platinum Catalyst”, Journal Of The Electrochemical Society, 161(3): H121-H128

Bladergroen, B.; Su, H.; Pasupathi, S. & Linkov V, (2012), “Overview of Membrane Electrode Assembly Preparation Methods for Solid Polymer Electrolyte Electrolyzer, Electrolysis”, Dr. Janis Kleperis (Ed.), ISBN: 978-953-51-0793-4, InTech, DOI:10.5772/52947.

Available from: http://www.intechopen.com/books/electrolysis/overview-of-membrane-electrode-assembly-preparation-methods-for-solid-polymer-electrolyte-electrolyz (accessed: 2014-11-20)

Borup, R.; Meyers, J.; Pivovar, B.; Kim, Y. S.; Mukundan, R.; Garland, N.; Myers, D.; Wilson, M.; Garzon, F.; Wood, D.; Zelenay, P.; More, K.; Stroh, K.; Zawodzinski, T.; Boncella, J.; Mcgrath, J. E.; Inaba, M.; Miyatake, K.; Hori, M.; Ota, K.; Ogumi, Z.; Miyata, S.; Nishikata, A.; Siroma, Z.; Uchimoto, Y.; Yasuda, K.; Kimijima, K.I. & Iwashita, N. (2007), "Scientific Aspects of Polymer Electrolyte Fuel Cell Durability and Degradation", Chemical Reviews, 107(10):3904-3951.

Brunauer, S.; Deming, L. S.; Deming, W. S.; Teller, E. J. (1940), “On a Theory of the Van der adsorption of gases”, Journal of American Society, 62(7): 1723.

Burdett, K. J.; Hughbanks, T.; Miller, G. J.; Richardson, J.W. & Smith, J. V. (1987) “ Structural-Electronic Relationships in Inorganic Solids: Powder Neutron Diffraction Studies of the Rutile and Anatase Polymorphs of Titanium Dioxide at 15 and 295 K” Journal of American chemical society, 109(12): 3639–3646.

Charreteur, F.; Ruggeri, S.; Jaouen, F. & Dodelet J. P. (2008),” Increasing the Activity of Fe/N/C Catalysts in PEM Fuel Cell Cathodes using Carbon Blacks with a High-Disordered Carbon Content” Electrochim Acta, 53(23): 6881-6889.

Chen, X.; Bai, X.; Deng, P.; Peng, D. & Liu, X. (2004) “Potential-pH Diagram of Zr-H_2O System at the Increased Temperatures” Rear Metal Materials and Engineering 33(1): 710-713

Chhina, H.; Campbell, S. & Kesler, O. (2007), “An Oxidation-Resistant Indium Tin Oxide Catalyst Support for Proton Exchange Membrane Fuel Cells”, Journal of Power Sources, 161(2): 893-900.

Chhina, H.; Campbell, S. & Kesler, O., (2007), “Thermal and Electrochemical Stability of Tungsten Carbide Catalyst Supports”, Journal of Power Sources 164(2): 431-440.

Ciapina, E.G.; Santos, S. F. & Gonzales E. R. (2010), “The Electro-Oxidation of Carbon Monoxide on Unsupported Pt Agglomerates”, Journal of Electro analytical Chemistry 644(2): 132-143.

Climent, V. & Feliu, J. M. (2011), "Thirty Years of Platinum Single Crystal Electrochemistry", Journal of Solid State Electrochem, 15(7-8): 1297-1315.

Cunha, L.; Vaz, F.; Moura, C.; Rebouta, L.; Carvalho, P.; Alves, E., Cavaleiro, A.; Goudeaue, P. H. & Rivière J. P. (2006), “Structural Evolution In ZrN_xO_y Thin Films as a Function of Temperature”, Surface And Coatings Technology, 200(9): 2917-2922

Curran, D.J. & Fletcher, K.S. (1968), “Lanthanum Hexaboride as an Electrochemical Generant of Lanthanum (III) for Titrations: Applications to Determination Of Nickel(II) Copper(II) and Zinc(II)” Analytical Chemistry, 40(12): 1809-1812

Doi, S.; Ishihara, A.; Mitsushima, S. & Kamiya, N. (2007), “Zirconium-Based Compounds for Cathode of Polymer Electrolyte Fuel Cells”, Journal of the Electrochemical Society, 154(3): B362-B369.

Esaka, F.; Furuya, K.; Shimanda, H.; Imanura, M.; Matsubayashi, N.; Sato, H.; Nishijima, A.; Kawana, A.; Ichimura, H. & Kikuchi, T. (1997), “Comparison of Surface Oxidation of Titanium Nitride and Chromium Nitride Films Studied by X-Ray-Absorption and Photoelectron-Spectroscopy”, Journal of vacuum science & technology. A. Vacuum, surface, and films, 15(1): 2521-2528.

Ferreira, P. J., La O’, G. J., Shao-Horn, Y., Morgan, G., Makharia, R., Kocha, S. & Gasteiger, H.A. (2005), “Instability of Pt/C Electrocatalysts in Proton exchange Membrane Fuel Cells”, Journal Of Electrochemical Society 152(11): A2256-A22.

Garnier, P. & Krachewski J.V. (2013) “Lanthanum Interaction with Surface Preparations”, The Electrochemical Society Abstract #2110.

Gelin, P. & Primet M (2002), “Complete Oxidation of Methane at Low Temperature over Noble Metal Based Catalysts: A Review”, Applied Catalysis 39(1):B1

Ham D. J. & Lee J. S. (2009) “Transitional Metal Carbides and Nitrides as Electrode Materials for Low Temperature Fuel Cells”, Energies,2(1): 873-899.

Hara, S. & Miyayama, M. (2004) “Proton conductivity of superacidic sulfated zirconia”, Solid State Ionics, 168(1-2): 111-116.

Hu, J.; Lu, Q.; Tang, K.; Yu, S.; Qian, Y.; Zhou, G. & Liu, X. (2000), “Low Temperature Synthesise of Nanocrystalline Titanium Nitride Via a Benzene-Thermal Route”, Journal of The American Ceramic Society 83(2): 430-432.

Hu, Z.; Chen, C.; Meng, H.; Wang, R.; Shen, P. K. & Fu, H. (2010), “Oxygen reduction electrocatalysis enhanced by nanosized cubic vanadium carbide”, Electrochem Communications, 13(8): 763-765.

Huang, F. & Liu, W.J. (2002), “Room Temperature Oxidation of Ultrathin TiB_2 Films”, Journal of Materials Research, 17(4): 805-813.

Huang, S.; Ganesan P. & Popov, B. N. (2009), “Development of conducting polypyrrole as corrosion-resistant catalyst support for polymer electrolyte membrane fuel cell (PEMFC) application” Applied Catalysis B: Environmental, 93(1-2):75-81.

Ignaszak , A.; Song, C.; Zhu, W.; Zhang, J.; Bauer A.; Baker R.; Nebeurchilov, V.; Ye, S. & Campell, S. (2012), “Titanium carbide and its core-shelled derivative TiC@TiO2 as catalyst supports for proton exchange membrane fuel cells”, Electrochimica Acta, 69(1): 397-405.

Inaba, M., Yamada, H., Tokunaga, J., & Tasaka, A. (2004), "Effect Of Agglomeration of Pt/C Catalyst on Hydrogen Peroxide Formation", Electrochemical and Solid-State Letters, 7(12): A474-A476

Inaba, M.; Kinumoto, T.; Kiriake, M.; Umebayashi, R.; Tasaka, A. & Ogumi, Z. (2006),"Gas Crossover and Membrane Degradation in Polymer Electrolyte Fuel Cells" Electrochimica Acta 51(26): 5746-5753.

Jerkiewicz, G.; Vatankhah, G.; Lessard, J.; Soriaga M. P. & Park Y. (2004), "Surface-oxide growth at platinum electrodes in aqueous H2SO4 Reexamination of its mechanism through combined cyclic-voltammetry, electrochemical quartz-crystal nanobalance, and Auger electron spectroscopy measurements", Electrochimica Acta, 49(9-10): 1451–1459.

Jiang, Z. (2011), "Carbon Nanotubes Supported Metal Nanoparticles for the Applications in Proton Exchange Membrane Fuel Cells (PEMFCs)" www.intechopen.com (accessed 27/08/2014).

Job, N.; Lambert, S.; Chatenet, M., Gommes, C. J.; Maillard, F.; Berthon-Fabry, S.; Regalbuto, J. R. & Pirard, J. (2010), "Preparation of highly loaded Pt/carbon xerogel catalysts for Proton Exchange Membrane fuel cells by the Strong Electrostatic Adsorption method ", Catalysis Today, 150(1): 119-127.

Jones, C. & Hitchman, M. L. (2009), "Chemical Vapour Deposition: Precursors, Processes and Aplications", RSC Publishing, Cambridge.

Kakinuma, K.; Wakasugia, Y.; Uchida, M.; Kaminoa, T.; Uchidab, H.; Dekia, S. & Watanabea, M. (2012) "Preparation of Titanium Nitride-Supported Platinum Catalysts with well Controlled Morphology and their Properties Relevant to Polymer Electrolyte Fuel Cells", Electrochimica Acta, 77(1): 279– 284.

Kinoshita K. (1988) "Carbon, Electrochemical and Physicochemical Properties", John Wiley &Sons, New York.

Komratov G. N. (1997), "The oxidation kinetics of titanium carbide, nitride, and carbonitride powders in air", Powder Metallurgy and Metal Ceramics, 36(9-10): 510-514.

Kosolapova, T. Y. (1986), "Preparation and Application of Refractory Compounds", Metallurgiya, Moscow, Russia.

Kucernak, R.A & Offer, G.J. (2008) "The Role of Adsorbed Hydroxyl Species in the Electrocatalytic Carbon Monoxide Oxidation Reaction on Platinum" Phys. Chem. Chem Phys, 10(25): 3699-3711.

Kulpa A. & Troczynski T. (1996) "Oxidation of TiB_2 Powders Below 900 °C" Journal American Ceramic Society 79(2): 518-520.

Larminie, J. & Dick, A. (2003) Fuel Cells Systems Explained Second Edition Wiley.

Lavrenko, V. A.; Yagupolskaya, L. N.; Kuznetsova, L. I.; Doroshenko, L. K. & Lugovskaya E. S (1974), "The Oxidation Of ZrB_2 TaB_2 Nb_2 and W_2B_5 in Atomic Oxygen and by Anodic Polarization", Oxidation of Metals, 8(3): 131-137.

Liu, Y. & Mustain W. E. (2011), "Structural and Electrochemical Studies of Pt Clusters Supported on High-Surface-Area Tungsten Carbide for Oxygen Reduction", ACS Catalysis, 1(3): 212-220.

Loroi, T.; Senoh H.; Yamazaki, S.; Siroma, Z.; Fujiwara N. & Yasuda K. (2008), "Stability of Corrosion-Resistant Magnéli-Phase Ti4O7-Supported PEMFC Catalysts at High Potentials", Journal of the Electrochemical Society, 155(4): B321-B326.

Lui, Y.; Kell ,G. T.; Chen, J. G. & Mustain, W.E. (2013), "Metal Carbides as Alternative Electrocatalyst Supports", ACS Catalysis, 3(6): 1184-1194.

Mackinnon I. D. R.; Alarco, J. A. & Talbot P. C. (2013). "Metal Hexaborides With Sc Ti Mn", Modelling and Numerical Simulation of Materials Science, 3(4): 158-169.

Maillard, F.; Schreier, S.; Hanzlik, M.; Savinova, E. R.; Weinkauf, S.; Stimming, U. & Federation, R. (2005), "Influence of Particle Agglomeration on the Catalytic Activity of Carbon-Supported Pt Nanoparticles in CO Monolayer Oxidation", Physical Chemistry Chemical Physics, 7(47): 385-393.

Mayrhofer, K. J. J.; Blizanac, B. B.; Arenz, M.; Stamenkovic, V. R.; Ross, P. N. & Markovic, N. M. (2005), "The Impact Of Geometric And Surface Electronic Properties Of Pt-Catalysts On The Particle Size Effect In Electrocatalysis", Journal Of Physical Chemistry, 109(30): 14433-14440.

Mayrhofer, K. J. J.; Strmcnik, D.; Blizanac, B. B.; Stamenkovic, V.; Arenz, M. & Markovic, N. M. (2008), "Measurement of Oxygen Reduction Activities via the Rotating Disc Electrode Method: from Pt Model Surfaces to Carbon-Supported High Surface Area Catalysts", 53(7): 3181-3188.

Meier, J.C.; Galeano, C.; Loannis, Katsounaros, Topalov, A.A.; Kostka, A.; Schuth, F. Mayrhofer, K. J. (2012) "Degradation Mechanisms of Pt/C Fuel Cell Catalysts Under Simulated Start-Stop Conditions", ACS Catalysis 2(5):832-843.

Milosv, I.; Strehblow, H. H.; Navinsek, B. & Metikos-Hukovic M. (1995), "Electrochemical and thermal oxidation of TiN coatings studied by XPS", Surface and Interface Analysis, 23(7-8): 529-539.

Mishlera, J.; Wanga, J.; Mukundanb, R.; Spendelowb, J.; Husseyc, D.S.; Jacobson, D.L. & Borupb, R.L. (2012), “Probing the Water Content in Polymer Electrolyte Fuel Cells Using Neutron Radiography”, Electrochimica Acta, 75: 1–10.

Mitsushima, S.; Kawahara, S.; Ota, K. & Kamiya, N. (2007) “Consumption rate of Pt under potential cycling”, Journal of the electrochemical society, 154(2), pp. B153-B158.

Mukerjee, S. (1989), "Particle Size and Structural Effects in Platinum Electrocatalysis", Journal Of Applied Electrochemistry, 20(4): 537-548.

Nicole, J.; Tsiplakides, D.; Pliangos, C.; Verykios, E.X.; Comninellisa, C.H. & Vayenas, C.G. (2001) “Electrochemical Promotion and Metal–Support Interactions”, Journal of Catalysis 204(1): 23–34.

Nikolic, J.; Exposito, E.; Iniesta, J. & Gonzalez-Garcia, J. (2009) “Theoretical Concepts and Applications of a Rotating Disk Electrode”, Journal of Chemical Education 77(9): 1191.

Park, Y.; Kakinuma, K.; Uchida, M.; Tryk, D.; Kamino, T.; Uchida, H. & Watanabe, M. (2013), “ Investigation Of The Corrosion Of Carbon Supports In Polymer Electrolyte Fuel Cells Using Simulated Start-Up/Shutdown Cycling” , Electrochimica Acta, 91:195-207.

Paulus, U.A.; Schmidth, T.J.; Gasteiger, H.A. & Behm, R.J. (2001) “Oxygen Reduction on a High-Surface Area Pt/C Carbon Catalysts: A Thin-Film Rotating Ring-Disk Electrode Study”, Journal of Electro analytical Chemistry 495:134-145.

Qi, Z. (2008), "Electrochemical Method for Catalyst Activity Evaluation", In: Zhang, J. (ed.) PEM Fuel Cell Electrocatalysts and Catalyst Layers. London: Springer.

Rabis, A.; Rodriguez, P. & Schmidt, T. J. (2012), "Electrocatalysis for Polymer Electrolyte Fuel Cells: Recent Achievements and Future Challenges", ACS Catalysis, 2(5): 864–890.

Radmilovic,V.; Gasteiger, H. A. & Ross, P.N. (1995), “Structure and Chemical Composition of a Supported Pt-Ru Electrocatalyst for Methanol Oxidation”, Journal of Catalysis,154(1): 98-106.

Ralph T. R.; Hudson S. & Wilkinson, D.P. (2006), “Electrocatalyst stability in PEMFCs and the role of fuel starvation and cell reversal tolerant anodes”, ECS Transansactions, 1(8);67-84.

Ramaswamy, N.; Hakim, N. & Mukerjee, S. (2008) “Degradation Mechanism Study of Perfluorinated Proton Exchange Membrane under Fuel Cell Operating Conditions” Electrochimica Acta, 53(8):3279-3295.

Reeve, R.W.;Christensen, P. A.; Dickinson, A.J.; Hamnett, A. & Scott K. (2000), “Methanol-tolerant oxygen reduction catalysts based on transition metal sulfides and their application to the study of methanol permeation” Electrochimica Acta 45(25-26): 4237–4250.

Reimer, L. & Koh,l H. (2008), “Transmission Electron Microscopy: physics of image formation” 5th Springer SCIENCE+Business Media, LLC, 5th edition, pp. 1.

Roth, C.; Bleith , P.; Schwobel, C. A.; Kaserer, S. & Eichler, J. (2014), “ Importance Of Fuel Cell Tests For Stability Assessment-Suitability Of Titanium Diboride as an Alternative Support Material” Energies 7(6): 3642-3652.

Rudi, S.; Cui C.; Gan, L. & Strasser, P. (2014), “Comparative Study of the Electrocatalytically Active Surface Areas (ECSAs) of Pt Alloy Nanoparticles Evaluated by H_{upd} and CO-stripping voltammetry”, Electrocatalysis, 5(4): 408-418.

Schell, G., winter, H., Rietschel, H. & Gomp F. (1982), “Electronic structure and supercondctiivity in metal hexaborides”, Physics Review B, 25(1):1589.

Schwanitz, B.; Rabis, A.; Horisberger, M. & Scherer, G. G. (2012), "Sputtered Cathodes for Polymer Electrolyte Fuel Cells: Insights into Potentials, Challenges and Limitations", Chimia, 66(3): 110-119.

Shao, Y., Lui, J., Wang, Y. M. & Lin, Y. (2009), “Novel Catalyst Support Materials for PEM Fuel Cells: Current Status and Future Prospects” Journal of materials chemistry, 19(1):46-59.

Shao, Y.; Yin, G. & Gao Y. (2007), “Understanding and approaches for the durability issues of Pt-based catalysts for PEM fuel cell”, Journal of Power Sources, 171(2): 558-566.

Sharma, S. & Pollet, G. B. (2012), “Support Materials for PEMFC and DMFC Electrocatalysts— A Review, Journal of Power Sources”, 208(15): 96-119.

Shioyama, H., Yamada, Y.; Ueda, A. & Kobayashi T. (2005) “Graphite intercalation compounds as PEMFC electrocatalyst supports”, Carbon, 43(11): 2374-2378.

Smirnova, A.; Dong, X.; Hara, H.; Vasiliev, A. & Sammes, N. (2005) “Novel Carbon Aerogel-Supported Catalysts for PEM Fuel Cell Application” International Journal of Hydrogen Energy, 30(2): 149-158.

Stevens D.A. & Dahn J.R. (2005), “Thermal degradation of the support in carbon-supported platinum electrocatalysts for PEM fuel cells”, Carbon, 43(1): 179-188.

Stonehart, P. & Ross, P. N. (1976), "The Use of Porous Electrodes to Obtain Kinetic Rate Constants For Rapid Reactions and Adsorption Isotherms Of Poisons", Electrochimica Acta, 21(6): 441-445.

Stonehart, P. (1984), “Carbon substrates for phosphoric acid fuel cell cathodes” carbon ,22(4-5): 423-431.

Sun, S; Zhang, G.; Sun, X.; Cai, M. & Ruthkoky, M. (2012), “Highly Stable and Active Pt/Nb-TiO_2 Carbon Free Electrocatalyst For Proton Exchange Membrane Fuel Cells”, Journal Of Nanotechnology 2012(1): 1-8.

Suzuki, Y.; Ishihara, A.; Mitsushima, S.; Kamiya, N. & Ota, K. (2007), “Sulfated-zirconia as a support of Pt catalyst for polymer electrolyte fuel cells”, Electrochemical and solid state letters, 10(7): B105-B107.

Takasaki, F.; Matsuie, S.;Takabatake, Y.; Nosa, Z.; Hayashi, A.; Shiratori, Y.; Ito, K. & Sasaki, K. (2011) “Carbon Free Pt Electrocatalysts Supported on SnO_2 for Polymer Electrolyte Fuel Cells: Electrocatalytic Activity and Durability”, Journal of the Electrochemical Society, 1858(10): B1270-B1275.

Thurier, C. & Doppelt, P. (2008), "Platinum OMCVD Processes and Precursor Chemistry", Coordination Chemistry Reviews, 252(1-2): 155-169.

Tikahashi, I. & Kocha , S.S. (2010), “Examination of the Activity and Durability of PEMFC Catalysts in Liquid Electrolytes”, Journal Of Power Sources, 195(19), pp.6312-6322.

Tominaka, S.; Monna, T.; Scrosati, B. & Osaka, T. (2010), “Sulphated Zirconia as A Proton Conductor for Fuel Cells: Stability to Hydrolysis and Influence on Catalysts”, Journal of Power Sources, 195(13): 4055-4071.

Uchimura, M. & Kocha, S. (2007), “The impact of cycle profile on PEMFC durability”, ECS Transactions, 11(1):1215-1226.

Urchaga, P. & Rice, C. (2013) “Ex-Situaccelerated Stress Test of Pt/C Cathode Catalysts.The Importance of Standard Test Procedures”, The Electrochemical Society Abstract #1441.

Verkhoturov, A.D.; Kuzenkova, M.A.; Lebukhova, N.V. & Podchernyaeva, I.A. (1988), “Electrochemical behavior of transition metals and refractory compounds of titanium in synthetic sea water” Soviet Powder Metallurgy and Metal Ceramics, 27(2):162-166.

Volonakis, G.; Tsetseris, L. & Logothetidis, S. (2011), “Electronic and Structural Properties of TiB_2: Bulk, Surface, and Nanoscale Effects”, Materials Science and Engineering B, 176(6):484-489.

Wang, H.; Li, H. & Yuan, X.; (2011), “PEM Fuel Cells Failure Mode Analysis”, CRC Press, pp. 36.

Wang, Y.; Chen, K. S.; Mishler, J.; Cho s. C. & Adroher C. (2011),“A review of polymer electrolyte membrane fuel cells: Technology, applications, and needs on fundamental research” Applied Energy, 88(4): 981-1007.

Wirth, S.; Harnisch, F.; Weinmann, M. & Schroder, U. (2012), “Comparative Study of IVB-VIB Transition Metal Compound Electrocatalysts for the Hydrogen Evolution Reaction”, Applied Catalysis -B: Environmental 126(25): 225-230.

Wu, J.; Yuan, X. Z.; Martini, J.J.; Wang, H.; Zhang, J.; Shen, J.; Wu, S. & Merida, W. (2008), “A review of PEM fuel cell durability: Degradation mechanisms and mitigation strategies”, Journal Of Power Sources, 184(1): 104-119.

Yin, S., Mu, S., Haifent, L.V., Cheng, N., Pan, M. & Fu, Z. A. (2010) “Highly Stable Catalyst for PEM Fuel Cell Based On Durable Titanium Diboride Support and Polymer Stabilization”, Applied Catalysis B: Environmental 93(3-4): 233-240.

Yin, S., Mu, S., Pan. M. & Fu, Z. A. (2011) “Highly Stable Tib2-Supported Pt Catalyst for Polymer Electrolyte Membrane Fuel Cells”, Journal of Power Sources 196(19): 7931-7936.

Yu, P. T.; Gu, W.; Makharia, R.; Wagner, F.T. & Gasteiger H. A. (2006), “The impact of carbon stability on PEM fuel cell startup and shutdown voltage degradation”, ECS Transactions, 3(1): 797-809.

Zellner, M.B & Chen, J.G. (2005), “Surface science and electrochemical studies of WC and W2C PVD films as potential electrocatalysts” Catalysis Today, 99(3-4): 299-307.

Zhang, J. (2008), “PEM Fuel Cell Electrocatalysts and Catalyst Layers”. London: Springer

Zhang, R.; Lee, T.; Yu, B.; Stampel, C. & Soon, A. (2012), “The Role of Titanium Nitride Supports for Single-Atom Platinum-Based Catalysts in Fuel Cell Technology” Physical Chemistry Chemical Physics, 14(48): 16552-16557.

Zhang, S.; Yuan, X.; Wang, H.; Merida, W.; Zhu H.; Shen, J.; Wu, S. & Zhang, J. (2009), “A Review of Accelerated Stress Tests of MEA Durability in PEM Fuel Cells”, International Journal of Hydrogen Energy, 34(1): 388-404.

Zhang, S.; Yuan, X.-Z.; Hin, J. N. C.; Wang, H.; Friedrich, K. A. & Schulze, M. (2009), "A Review Of Platinum-Based Catalyst Layer Degradation In Proton Exchange Membrane Fuel Cells", Journal of Power Sources, 194(2): 588-600.